UNIVERSITY OF OKLAHOMA

GRADUATE COLLEGE

SIMULATING PHOTOVOLTAIC ARRAY PERFORMANCE USING

RADIATION OBSERVATIONS FROM THE OKLAHOMA MESONET

A THESIS

SUBMITTED TO THE GRADUATE FACULTY

In partial fulfillment of the requirements for the

Degree of

MASTER OF SCIENCE IN METEOROLOGY

By

NICHOLAS A. ENGERER

Norman, Oklahoma

2011

SIMULATING PHOTOVOLTAIC ARRAY PERFORMANCE USING
RADIATION OBSERVATIONS FROM THE OKLAHOMA MESONET

A THESIS APPROVED FOR THE
SCHOOL OF METEOROLOGY

BY

_____
Dr. Mark L. Morrissey, Chair

_____
Dr. Susan E. Postawko

_____
Dr. J. Scott Greene

DEDICATION

This thesis document is dedicated to the tireless efforts of my mother,

Pamela, and my father, Daniel, who raised me with a relentless love and

a continual self-denial that should be greatly admired. Truly all of my

achievements are realizations of the merit of their efforts.

I will continue to act justly, to love mercy and to walk humbly in honor of

your sacrifices.

ACKNOWLEDGEMENTS

has enriched my life. In this regard, you have all contributed to my successes and the completion of this project.

To my fiancé Teddi, your support throughout the process of creating this thesis has been more active and involved than any other. Your patience, encouragement and love have been instrumental in fostering the energy required to complete this task.   Through the stress, turmoil and frustration involved in arriving at this juncture, our relationship has helped lead me to a personal awakening greater than any science project alone could provoke. You are a joyful and beautiful being. Let us continue to "conquer this world" together.

To all of you whom I would call my friends, you are an overwhelming force of blessing in my life. To my Ohio University crew – Aaron, Bex, Jared, Jordan, Noah, Terry and Wes and those I've met in Oklahoma – Owen, Stephen D., Stephen M., Zach, Rob. Together we have made many great memories, learned countless lessons and have become quite the companions along this journey. Without such friendships and the accompanying experiences, my time laboring on this thesis project would have benefited from far less inspired thought.

On the professional side of things, I must begin with my advisor Mark Morrissey, for taking me on as his student in June 2010 when I first

came to him with this project, without that leap of faith, this project may not have not been possible. To my committee members, Susan Postawko and Scott Greene, your contributions to this process are much appreciated. Additionally, I must thank my previous advisor Dr. Ming Xue for accepting me as his student here in 2008 and for his many hours of instruction and guidance throughout the first two years of my graduate education. Next, I must extend my gratitude to Celia Jones for her advice, her smiles and her genuine spirit. She truly makes this school a better place! To that end, I also am grateful to the School of Meteorology as well as the Ohio University Meteorology program for their instruction and provided opportunities. To Bob Willis of Sunrise Alternative Energy, thank you for your guidance in developing some of the specifics in this project. It is my sincere hope that this project contributes in a meaningful way to the growth of solar energy in the state of Oklahoma. Also, I must thank Howie Bluestein for involving me in his Vortex2 team driving the "Howie-mobile".

Finally, I must extend my most sincere respect to the Sangha of the Chung Tai organization, particularly the nuns at Buddha Mind Monastery in Oklahoma City. Your efforts have lead me to realize the value of selflessness and have left me with the desire to be a servant

unto the world. Changing my thesis topic from tornadogenesis to solar energy two years into my degree was no small event, and was a reflection of an internal shift in what I consider important. That shift was inspired by your diligence and instruction. In that regard you have contributed significantly to this document.

To any whom I have forgotten, trust that the gratitude lacking on these pages is alive in my heart.

TABLE OF CONTENTS

LIST OF TABLES

LIST OF FIGURES

Figure

ABSTRACT

Given the anticipated nationwide growth of solar energy applications, attributable to technological advances, falling production costs and increases in the number of state and federal incentives, a detailed understanding of Oklahoma's solar energy resource and the manner in which weather events, namely clouds, modulate surface solar radiation budgets (and therefore solar energy generation) is becoming increasingly more relevant. The Oklahoma Mesonet provides a unique opportunity to investigate such topics at a much finer scale than has previously been available. The Mesonet represents the world's largest long-term network of solar radiation sensors, consisting of over 115 Li-Cor pyranometer sensors, the majority of which have reported five-minute averages of downwelling solar radiation data since 1994. Through the use of two radiation models and photovoltaic and inverter simulation programs, the performance of two residentially sized (2kW) rooftop photovoltaic arrays were simulated using sixteen years of the Mesonet radiation observations. These long-term simulations were then broken down into yearly, seasonal and monthly level statistics in order to provide potential end users with reliable and explicit predictions of expected power production in order to encourage photovoltaic

installations in the state of Oklahoma. Analyses of a small collection of daily case studies were also completed, to investigate how power production might vary within a given day under various meteorological conditions. Additionally, a method for translating Mesonet radiation observations into power output for over 500 different photovoltaic module types has now been established. In this manner a new realm of research at the intersection of solar energy and meteorological science is now available for future study.

CHAPTER 1: INTRODUCTION

1.1 BACKGROUND

1.1.1 Photovoltaic Solar Energy

Solar energy production is the fastest growing source of power in the world. Lead by a 3.6% average annual reduction in costs and marked rises in efficiency of photovoltaic modules over the past 35 years (Figure 1.1.1-1) photovoltaic power generation is becoming increasingly more relevant with time (Topline Strategy Group 2006; RNCOS 2011). Worldwide photovoltaic generation capacity was estimated to be in excess of 20.4 gigawatts amongst International Energy Agency (IEA) participating countries in 2009 (International Energy Agency 2010a), with the exponential growth driven predominantly by grid-tied systems (Figure 1.1.1-2). In the United States, it is estimated that energy production from photovoltaic systems grew by 700 megawatts (MW) to 2.2 gigawatts (GW) in 2010 with the rate of installations accelerating rapidly. Some analysts predict a four-fold increase in the total installed capacity of the U.S. by 2014 to over 8.8 GW (RNCOS 2011).

This growth in photovoltaic installations increases the relevancy of the meteorological factors influencing solar energy generation. Expected generation from a photovoltaic cell is dependent upon the processes

1

modulating solar radiation, namely clouds. Past weather data will be needed to create predictions for how a given photovoltaic system will perform in the future over the long term. At shorter time scales, the widespread integration of distributed photovoltaic energy generation over the coming decades will shift the percentage of overall power production from traditional, stable sources to one that is more spatially and temporally variable. This creates a need for short-term power forecasts (on the order of a few hours to a few days) that are dependent on future meteorological conditions. In this manner, the past, present and future weather conditions all are highly relevant to solar energy production. This provides meteorologists with new research opportunities to meet the demands of the rapidly growing solar energy sector.

1.1.2 Radiation Observations from the Oklahoma Mesonet

The Oklahoma Mesonet (Brock et al. 1995; McPherson et al. 2007) is a network of over 115 observation stations located throughout Oklahoma that feature various environmental sensors that have been reporting current atmospheric and soil conditions at five-minute intervals to the Oklahoma Climate Survey (OCS) since January 1st, 1994. Included in these reported conditions is a global horizontal irradiance (GHI) measurement, taken from a Li-Cor 200S pyranometer at a height

of 1.5 m. These pyranometer observations represent the largest network of radiation observations of its given spatial density (mean separation distance between stations of less than 30km (Brotzge and Richardson 2003)) in the world.

This spatial density, coupled with a five-minute temporal resolution, provides an extremely valuable scientific dataset for studying geophysical processes related to radiation at a wide variety of scales. The radiation observations from the Mesonet have most commonly been used to study surface energy budgets and in the subsequent development of diagnostic and operational surface energy models. Examples of such work include the Surface Energy Budget Model (Crawford 1998; Crawford and Bluestein 2000), the development of heat flux parameterizations in the Noah Land Surface Model (Godfrey and Stensrud 2010), developing methods of computing surface fluxes from observation data (Zhou and Xu 1999) and in analysis of surface skin temperatures (Fiebrich et al. 2003). Mesonet radiation observations have also been incorporated into the study of various mesoscale meteorological phenomena. This includes research of rapidly developing nocturnal inversions (Hunt et al. 2007), and mesoscale air circulations induced by the impact of wheat fields on surface albedo (McPherson et

al. 2004). The spatial and temporal scales of the radiation field itself

have also been investigated using the Mesonet radiation measurements

(Barnett et al. 1998). Additionally, radiation observations from the

Mesonet have been coupled with observations from the Oklahoma

Atmospheric Surface-Layer Instrumentation System (OASIS), in which 10

Mesonet sites were outfitted with additional radiation measurement

equipment for studying the shortwave and longwave radiation budgets.

Correlations between these ten "super-sites" and the Mesonet

observations have been constructed (Brotzge and Richardson 2003).

Although further studies using radiation observations from the OASIS

sites have been conducted (Sridhar and Elliot 2002, Brotzge 2004),

these studies do not use the original Mesonet downwelling radiation

measurements. To date, Mesonet radiation observations have not been

used in any peer-reviewed study of the solar radiation climatology of

Oklahoma or in assessment of the potential solar energy resource.

1.1.3 Solar Radiation Resource Assessment

Previous analyses of the solar energy resource available to a

particular region have, in actuality, been studies of the solar radiation

budgets, rather than actual investigations of potential energy production.

A method of translating W/m^2 insolation measurements to kWh power

output is needed to directly support the solar energy industry. The first such study of the solar radiation resource available to a particular region in the United States was a nationwide study completed in 1965, which used hourly measurements from 59 pyrheliometers and hourly sunshine and cloud cover observations from 113 weather stations to produce monthly maps of daily mean insolation at a very coarse level of prediction (Bennett 1965). Since that time, the spatial and temporal density of data available for a nationwide analysis has greatly increased through the spread of observation equipment and the development of new technologies (namely satellites). Nationwide analyses at a 40km resolution are now completed by the National Renewable Energy Laboratory (NREL), wherein predictions are tailored to solar energy applications through the estimation of solar radiation available to a south facing surface at latitude tilt (NREL 2011). This prediction is provided by the Climatological Solar Radiation Model (Maxwell 1998), which ingests solar radiation observations (Figure 1.1.3-1), satellite derived irradiances, and information about cloud cover, water vapor, trace gasses and aerosols to create predictions of available radiation in terms of kWh/m^2/day (Figure 1.1.3-2).

Independently created state level analyses of the solar radiation

resource are available for several states, including, but not limited to

Alaska (Dissing and Wendler 1998), Arizona (Giacomelli 2002), Texas

(Vliet 2004), Nebraska (Rosenberg 1964) and California (Granger 1980).

However, many of these studies are outdated and include less detail

than the national level analysis produced by NREL. Additionally, they

are not presented in terms of south-facing surfaces tilted at latitude, an

important step in translating the radiation resource into power output

from photovoltaic solar energy installations. For these reasons, a large

majority of states, including Oklahoma, currently rely upon the

aforementioned NREL nationwide studies when assessing the solar

radiation resource available for solar energy applications.

1.2 MOTIVATION

The motivation and objectives for this study can best be

summarized in three major components. First, Oklahoma's potential for

solar energy greatly exceeds the current installed capacity (currently

below 100kW and limited to only a few homes and businesses for which

official statistics are unavailable). This study will provide explicit

predictions of power output from residentially sized systems for any

6

location in Oklahoma, to encourage photovoltaic installations within the state (Section 1.2.1).

Secondly, no sufficient radiation resource assessment has been performed for the state of Oklahoma, nor has a method of translating radiation analyses or measurements into power production been established (Section 1.2.2). This study will solve both of these issues by creating a basic solar climatology, and more importantly, by providing explicit predictions of power production from residentially size rooftop arrays. Rooftop arrays, such as the ones simulated in this study, are responsible for a majority of the grid-tied photovoltaic installations (Figure 1.2-1), which are the fastest growing sector of solar energy industry (Section 1.1.1).

Third, by creating a method of translating solar radiation observations from the Oklahoma Mesonet into power production figures for any of the 500-plus module types available in the Sandia Performance Model Database (King 2004), a new realm of research possibilities is opened. With nearly two decades of meteorological data from the Mesonet available for research, a wide variety of topics at the intersection of meteorological and solar energy science can now be investigated. The relevancy of such research topics is growing quickly,

driven by the rapid adoption of solar power production. If solar energy is to be successfully adopted at a significant scale, the variable nature of solar power production will require a system of forecasting solar energy generation. The creation of the translation system developed within this study is a significant step toward that goal.

1.2.1 Solar Power as an Electricity Generation Source in Oklahoma

Oklahoma is commonly referred to as an "energy state", owing mostly to the large amount of natural gas and crude oil it produces. It is the third largest natural gas producer and the sixth largest crude oil producer in the United States, with a total statewide economic impact of $23.8 billion dollars annually generated from these two industries (Snead and Barta 2008). In turn, Oklahoma generates most of it electricity from natural gas, which accounted for 64.1% of installed power generation capacity in 2008, totaling 12,985 MW. In addition to natural gas, coal accounts for 26.2% of installed capacity at 5,302 MW, followed by hydroelectric at 4.2% with 851 MW of capacity and wind accounting for 3.5% with 700 MW installed (Energy Information Agency 2010). According to this report, installed solar energy capacity was zero MW in 2008 for the state of Oklahoma. As of 2009, Oklahoma, Alaska, Kansas, Kentucky, Iowa, Nebraska, North Dakota, South Dakota and West

Virginia were all tied for last place in a ranked list in installed solar energy capacity, with a total of 100 kW or less (Sherwood 2010).

The relatively small solar power production is not a result of insufficient solar radiation in Oklahoma. According to one study (Topline Strategy Group 2006) Oklahoma was tied with Texas for 6th in average available sunshine for solar energy generation. However, an absence of state incentives (Oklahoma currently offers no solar energy incentives) and general lack of knowledge about solar energy's potential impact upon the state appear to be responsible. It is noted that Texas had over 4.2 MW installed by 2009 (Sherwood 2010). Therefore, it is a goal of this study to provide accurate estimates of residentially sized, rooftop solar energy systems to the general public, to increase awareness of the potential benefits to Oklahoma from photovoltaic installations throughout the state. The results from this study are presented in straightforward, easily interpretable maps and plots conveying information about expected power production and potential variation at the yearly and monthly levels (Chapter 4). Detailed analyses of power production statistics are focused on more population dense regions, so as to influence the greatest number of potential end users. Additionally, through the explicit estimation of solar power potential this study provides

the public and lawmakers with information to make informed decisions

concerning the implementation of state incentives for solar installations.

According to the Oklahoma Energy Security Act of 2008, 15% of

Oklahoma's electricity production will be sourced by renewables by 2025.

As of 2008, 8.1% of total electricity production was generated by

renewable sources, with 5.0% from hydroelectric and 3.1% from wind.

The remaining 6.9% could likely be sourced, in part, by solar energy

given proper state level incentives.

1.2.2 Past Solar Energy Analyses Conducted for Oklahoma

Direct assessment of the solar radiation resource available to

Oklahoma has only been performed at the regional level (i.e. the

Southern Great Plains) (Gao et al. 1998; McManus 1999), while only

indirect analyses have been completed at the state level (Barnett et al.

1998). In Gao et. al. (1998) a modeling method incorporating high-

resolution satellite data and ground based observations was created to

estimate surface radiation fluxes. However the model is only accurate

for clear skies and requires surface observations to correct estimates of

radiation fluxes under cloudy conditions, although a method for this

correction is not provided. Such a shortfall would significantly hinder

viable application of the model to solar energy research, wherein the

modulation of power production by clouds its extremely important. For

the latter study, (e.g. Barnett and Richie 1998), the primary purpose of

the study was to verify the representativeness of the surface solar

radiation measurements taken at the Atmospheric Radiation

Measurement (ARM) Program (Stokes and Schwartz 1994) sites within

or near Oklahoma. The study investigated the various spatial and

temporal scales at which processes in the solar radiation field evolved.

Analyses of the ARM measurements were compared against the finer

resolution analyses produced by the Mesonet radiation observations to

see whether the ARM derived fields were representative at relevant

spatial and temporal scales. This work, although very relevant to the

ARM program, did not produce any maps or datasets that would be

useful in solar energy applications. It is clear that both of these studies,

although scientifically relevant for some applications, are of little use in

the prediction of solar power output.

The same can be said of the detailed site-level analyses of cloud

and radiation behavior in the region provided by the Southern Great

Plains portion of the ARM project. Research studies produced by this

network include the cloud climatology work of Lazarus and Krueger

2000, the investigative work on individual cloud types with cloud radars

(Clothiaux et al. 1999; Kollias et al. 2007; Stokes and Schwartz 1994) and the study of how clouds modulate radiation through the Cloud and Radiation Testbed (Stokes and Schwartz 1994). Although these ARM studies are helpful for investigating the impact of clouds upon surface radiation budgets, they are not regional analyses, offer no long-term resource assessment and are not translatable into power production. At this time, it appears the primary benefit of the ARM program to solar energy applications will likely come from the work being done on cloud-radiation interactions and cloud resolving models (Guichard et al. 2003; Henderson and Pincus 2009; Wu et al. 2007).

In reviewing the literature, the most relevant work available for determining the solar radiation resource in the Oklahoma region is the dissertation work of Gary McManus. McManus developed a climatology of cloud type and frequency and global solar radiation the Great Plains region spanning the years 1952-1991 (McManus 1999). In his work, he produced maps of the annual, seasonal and monthly solar radiation resource as well as cloud cover and type for the Great Plains region. Although Oklahoma was included in this analysis, the resulting maps of global horizontal irradiance are inferior to both the national level maps produced by NREL and the analysis that could be produced through use

of the Mesonet radiation data. McManus 1999's radiation analyses are only available at a monthly resolution, leaving the variability within the month and individual days unknown, both of which are of great interest to modern solar applications. Additionally, the solar radiation estimates have not been translated to a tilted, south facing surface, a modeling process which takes a great deal of consideration to perform accurately (see Section 2.3 and 2.4). Despite these shortfalls, the cloud climatology developed by McManus 1999 was found to be quite useful in diagnosing the causes of variation in solar power production between seasons and months in Section 4.5.

Given the lack of an adequate state-level solar power analysis for Oklahoma, rough estimation of the expected power output from solar energy installations in the state can be obtained through the National Renewable Energy Laboratory's PVWatts program (Marion 2010). The PVWatts software utilizes the same core prediction equations as the Sandia Performance Model used in this study (Section 2.5) to translate NREL radiation data into predicted power output for a given module type at a location specified by the user. In Oklahoma, users may choose one of two locations (Oklahoma City or Tulsa) to access power production estimates for a variety of module types and orientations. These

estimates are created from Typical Meteorological Year 2, or TMY2, data in the National Solar Radiation Database (NREL 2007) which are based on hourly solar and meteorological data. For locations outside of these two cities, data is interpolated from the previously discussed 40km monthly level analysis (refer to Section 1.1.3). Although both a radiation analysis and a translation system are provided through the NREL software, it is clear that the input radiation data is inferior to the much finer spatial and temporal scales of radiation data sampled by the Oklahoma Mesonet. This study provides a high resolution (2km) resource assessment based on the simulation of rooftop sized photovoltaic arrays at five-minute temporal resolution for any given location in the state of Oklahoma. In this manner, potential end users in Oklahoma will have access to a solar energy analysis that greatly exceeds the NREL based analyses in resolution and accuracy.

1.2.3 The Potential Solar Energy Research with Mesonet Radiation Data

The Mesonet radiation observation network represents a coupling of high temporal and spatial resolutions that provide a unique resource for solar energy research in Oklahoma. The database of radiation observations used herein encompasses sixteen years (1994-2009) of

14

five-minute data from 108 unique station locations and has applications for hundreds of studies on how meteorological events modulate surface radiation budgets, numerical model parameterizations and coincidentally, solar energy production on a wide variety of time scales. The current study will focus on developing long-term assessments of past radiation data to predict how rooftop sized photovoltaic arrays will perform in the future. However, the potential research projects that will be made available by the developed translation method used to create this assessment will be broader in scope. Addressing the difficulties of large scale integration of distributed photovoltaic's due to the variability of the solar radiation resource, assessing the solar energy generation potential of a commercial sized solar farm, or investigating the total rooftop energy resource of any given region in the state are a few examples of highly relevant studies that will be possible through the methodology presented in this study.

1.3 OBJECTIVE

The main objective of this study is to use archived Mesonet radiation observations to create projections of energy production from 2kW rooftop photovoltaic arrays based on estimates of past performance. Power production estimates will be created through the

coupling of existing radiation and photovoltaic simulation models to create one comprehensive photovoltaic modeling system (Chapter 2). This modeling system will then be integrated forward through the sixteen years of radiation observations available from 108 stations located across Oklahoma. Output will be produced on yearly, monthly and daily time levels with means and variability presented through easily interpreted mediums, such as maps and time series plots in terms of predicted power production. In this manner, end users will be able to analyze their personal energy consumption and the predicted offset provided by a 2kW photovoltaic installation (Chapter 4) to complete a cost-benefit analysis (Section 4.6). In summary, the end goal of this project is to encourage photovoltaic installations in the state of Oklahoma through the provision of reliable and explicit predictions of power output of an optimally sized residential solar energy system.

CHAPTER 2: MODELING PROCESS

2.1 OVERVIEW

In order to predict photovoltaic array energy output from the

Oklahoma Mesonet, global horizontal radiation (E_g) measurements, two

radiation models, a photovoltaic (PV) array model and an inverter model

were required. First, it was necessary to separate (Section 2.2.5) the

global horizontal measurements into direct (also known as beam

radiation, E_b) and diffuse radiation (E_d) components via the Direct

Insolation Simulation Code or DISC model (Maxwell 1987); (Section 2.3).

Second, estimates of diffuse radiation incident upon a tilted PV module

were produced through the Hays-Davies-Klucher-Reindel, or HDKR,

transposition model (Reindl et al. 1990) (Section 2.4). Third, the Sandia

Performance Model coupled with the Sandia Module Database (King

2004) was used to predict DC power output from a given PV module or

array (a string of modules). Lastly, an inverter model is required (King

2007) in order to simulate AC power output from the PV array system.

To fully understand the complexity of the modeling process, a

review of the properties of solar radiation is necessary. In order to

predict the amount of solar radiation available to a tilted PV module, solar

geometric variables must be defined and the various sources and types

17

of radiation available for PV power generation explained. It is also necessary to review the ways in which atmospheric constituents modify incoming solar radiation through scattering and reflection.

2.2 REVIEW OF SOLAR RADIATION

2.2.1 Extraterrestrial Solar Radiation

The primary source of energy in photovoltaic power production is of course the sun. The sun has an effective blackbody temperature of 5777 K driven by a continual high intensity fusion reaction which emits a broad spectrum of electro-magnetic radiation (Duffie 2006). This radiation is transmitted through the vacuum of space and after several minutes of travel, strikes the outer layer of the Earth's atmosphere. The energy of this direct normal irradiance (as received on a perpendicular surface at the top of the atmosphere at the mean earth-sun distance) is reported as the solar constant E_{sc} and is equivalent to approximately 1367 W/m^2 (Krivova et al. 2011).

There are also variations in this solar constant value, in the case of solar engineering, most of which can be neglected (Duffie 2006). However the variation caused by the obliquity of the Earth's orbit leads to a $\pm$ 3.3% change in the received radiation, which must be accounted for. A relationship accounting for this adjustment yields the extraterrestrial

radiation incident upon a surface normal to the incoming radiation, E_{ext}, and is given in the following equation (Spencer 1971):

$$E_{ext} = E_{sc} \cdot \left(1 + 0.033 \cdot \cos\left(\frac{360 \cdot n}{365}\right)\right)$$
(1)

where n is the nth Julian day of a given year.

2.2.2 Modification of Solar Radiation by the Atmosphere

As solar radiation enters the Earth's atmosphere, it is modified by a wide variety of sources. Under clear skies, incoming radiation is absorbed, reflected or scattered by aerosols and precipitable water vapor (Gueymard 2003) and also by atmospheric gaseous constituents such as ozone and nitrogen dioxide. Under cloudy conditions, the primary source of radiation modulation becomes cloud liquid water droplets, which in extreme conditions can reduce the direct radiation received at the surface by 100% and the overall performance of a PV module by 95% (reference Section 4.4.3). Given the extensive modification of solar radiation when traveling through the atmosphere, special attention must be paid to the type and amount of radiation available at the surface to correctly analyze the radiation available for energy generation. For solar energy applications, this includes partitioning solar radiation available at the surface into two distinct components: direct and diffuse radiation.

Direct radiation, henceforth known as 'beam' radiation in order to retain clarity in variable subscripts, accounts for the portion of solar radiation that has not been absorbed, reflected or scattered. Beam radiation is a concentrated energy source and arrives in a straight line from the solar disk. In this manner, direct radiation can be measured through a two-axis (horizontal and vertical) tracking unit that follows the sun across the sky. Measuring the beam radiation in this manner yields Direct Normal Irradiance (E_n or DNI), which along with solar geometry can be translated to the radiation received by a given fixed surface, such as a solar cell (Section 2.2.3). Due to the intense nature of this radiation source, most of the electricity generated by PV systems is converted from beam radiation (reference Section 4.4).

The secondary form of radiation utilized by PV devices is diffuse radiation. Diffuse radiation encompasses the solar radiation that has been scattered by atmospheric processes, changing the direction from which the light arrives. The primary form of scattering is Rayleigh scattering, which is applicable for objects up to 1/10 the wavelength of light, such as air molecules, and is the cause of our blue sky (Rojo and Berman 2010). The secondary form of scatter is termed Mie scattering, which applies to objects greater than 1/10 the wavelength of light and is

the primary source of white glare around the sun (termed the circumsolar radiation) and for the scattering of light by clouds or aerosols (Bohren 2010). On a given day, diffuse radiation arrives anisotropically from nearly all angles, and thus the measured diffuse radiation will change with the orientation of a given sensor.

2.2.3 Determining the Beam Radiation Incident on a Tilted Surface

For performance predictions of photovoltaic applications, the beam and diffuse components incident upon a given module's surface must be known. PV arrays most often are fixed (in residential applications), though some arrays may feature 1 or 2 axis tracking (variable tilt and azimuth angles) in order to follow the solar disk and receive more beam radiation, thus increasing power output. For the purpose of this study, only fixed tilt systems will be considered. Given a fixed tilt photovoltaic array at latitude λ, tilt angle α_m, and azimuth angle γ_m and a measurement of direct normal irradiance, E_n, the quantity of beam radiation incident upon the module surface at module tilt, E_b, can be calculated. For this calculation several solar geometry terms must be introduced and defined.

2.2.3.1 Solar Geometry Basics

First, values of the solar zenith and azimuth angles (θ_z and γ) are needed. Solar zenith angle is a measure of the height of the sun in the sky with respect to the horizon. It is measured as the angular departure of a line drawn from the sun to the earth and a line perpendicular to the earth's surface. The azimuth angle (γ) is measured as the deviation from the plane formed by the meridian drawn directly through module and normal to the surface, so that an object directly south of a reference location has $\gamma = 0°$, whereas one directly east (west) would have an angle of -90° (+90°). Determining the value of these two terms requires calculation of the hour angle (ω), which is the angular displacement between the local meridian and the sun's position caused by the rotation of the earth, and also the declination angle (δ), which gives the angle of the sun at solar noon with respect to the equator.

The declination angle is given by Spencer 1971 as:

$$\delta = 0.006918 - 0.399912 \cdot \cos(\rho) + 0.070257 \cdot \sin(\rho) - 0.006758 \cdot \cos(2\rho)$$

$$+ 0.000907 \cdot \sin(2\rho) - 0.002697 \cdot \cos(3\rho) + 0.001480 \cdot \sin(3\rho) \qquad (2)$$

Where $\rho = (n - 1) \cdot 360/365$ and n is the nth day of the year.

The hour angle calculation is slightly more complicated, it is given by:

$$\omega = \tau - \psi \qquad (3)$$

22

Where τ is the current GMT time in decimal form and ψ is the local solar noon (the time of the minimum zenith angle for a given location), which is given by:

$$\psi = 12 - \left(\varepsilon/60\right) - \left(\zeta/15\right) \tag{4}$$

The current longitude is given by ζ and ε is the equation of time correction, which accounts for the difference in mean solar time and actual solar time for a given location (accounting for obliquity and eccentricity in the Earth's orbital procession). The relationship for ε is given by (Woolf 1968) as:

$$\varepsilon = 0.258 \cdot \cos(\Omega) - 7.416 \cdot \sin(\Omega) - 3.648 \cdot \cos(2\Omega) - 9.228 \cdot \sin(2\Omega) \tag{5}$$

$$\text{where } \Omega = 360 \cdot \frac{(n-1)}{(365.242)}$$

and n is the nth day of the year

Given the above calculations for the hour angle (ω) and solar declination angle (δ), the zenith angle (θ$_z$) calculation is given by (Duffie 2006) as:

$$\cos(\theta_z) = \cos(\lambda) \cdot \cos(\delta) \cdot \cos(\omega) + \sin(\lambda) \cdot \sin(\delta) \tag{6}$$

And the azimuth angle (γ) by:

$$\cos(\gamma) = sign(\omega) * |\cos^{-1}\{\frac{(\cos(\theta_z) \cdot \sin(\lambda) - \sin(\delta))}{\sin(\theta_z) \cdot \cos(\lambda)}\}| \tag{7}$$

23

Finally, the concept of air mass (AM) must be introduced. Air mass values represent the optical depth of the atmosphere through which solar radiation must pass before reaching the surface. An air mass value of 1 is present when the sun is directly overhead (at a zenith angle of zero). Any displacement from a zero zenith angle increases the AM value according to Equation 8 (Kasten and Young 1989; King 1997):

$$AM = \left[\cos(\theta_z) + 0.5057 \cdot \left(96.08 - \theta_z\right)^{-1.634} \right]^{-1}$$

(8)

Air mass values are used in multiple different ways in solar radiation modeling. They are used in the prediction of the horizontal component of beam radiation in the DISC model (Section 2.3), it is used to account for important variation in the solar spectrum at large zenith angles in the Sandia Performance Model (Section 2.5) and it will help analyze the impacts of terrain on photovoltaic energy generation in Section 4.5.

2.2.3.2 Beam Radiation on Horizontal and Tilted Surfaces

With the above solar geometry defined, and a provided value of E_n, the components of beam radiation on both horizontal and tilted surfaces are given by simple geometric relationships. First, the angle of

24

incidence (θ_a), which is the angle between beam radiation striking a surface and the normal to that surface, is given by:

$$\cos(\theta_a) = \cos(\lambda) \cdot \cos(\theta_z) + \sin(\lambda) \cdot \sin(\theta_z) \cdot \cos(\gamma - \gamma_m) \qquad (9)$$

Then, given the angle of incidence (θ_a) and the zenith angle (θ_z), both the horizontal component (E_{bh}) and the tilted component (E_b) of beam radiation can be calculated by (Duffie 2006):

$$E_{bh} = E_n \cdot \cos(\theta_z) \qquad (10)$$

and

$$E_b = E_n \cdot \cos(\theta_a) \qquad (11)$$

2.2.4 Determining the Diffuse Radiation Incident on a Tilted Surface

For a tilted surface, diffuse radiation will arrive from three primary sources (Figure 2.2.4-1) and will vary with the tilt angle at any given time. The first source is circumsolar diffuse radiation, which is the most intense source of diffuse radiation and is caused by forward scattering of beam radiation by air molecules, water vapor and aerosols. This source of diffuse radiation is the cause of the glare surrounding the sun under clear sky conditions and is often referred to as the circumsolar disk (Perez et al. 1987). The second source originates from the broad spectrum scattering that occurs near the horizon as light passes through increased

25

depths of atmosphere (measured by air mass (AM), see Section 2.3).

This results in a ring of increased light levels at the base of the sky

hemisphere and is termed horizon brightening. This brightening is most

apparent under clear-sky conditions. The third source is termed

isotropic, and is emitted from the full sky hemisphere in a directionally

uniform fashion. Under cloudy skies, it is assumed that most (if not all) of

the diffuse radiation will be isotropic in nature.

Due to the complex nature of diffuse radiation, the amount of

diffuse radiation on a tilted surface must either be directly measured at

the source, or, more commonly, estimated via a transposition model. A

transposition model most often uses the horizontal value of diffuse

radiation, a given surface orientation and knowledge of the "clearness"

as given by the clearness condition K_t to estimate the diffuse radiation

arriving from the three sources. The clearness condition (also referred to

as a transmission coefficient) K_t was first given by Liu and Jordan 1960

and is the ratio of measured global horizontal radiation to the

extraterrestrial radiation on a horizontal surface:

$$K_t = \frac{E_g}{E_{h\_ext}}$$

(12)

Where E_{h_ext} is the extraterrestrial radiation on a horizontal surface,

and is equivalent to the vertical component of the E_{ext} value defined in

2.3.1:

$$E_{h\_ext} = E_{ext} \cdot \cos(\theta_z)$$
(13)

This clearness condition K_t approaches unity for clear conditions

and approaches zero for cloudy conditions. The clearness conditions

can then be used to partition a measured or estimated horizontal diffuse

radiation component amongst the various radiation sources. For

example, a low value of the clearness condition would indicate cloudy

conditions and a larger value of isotropic radiation with a reduced amount

of circumsolar radiation. For a larger value of K_t, the opposite is true,

with increased amounts of circumsolar radiation and reduced values of

isotropic radiation. This approach can be applied in several different

ways with various levels of complexity. Some models are completely

isotropic (Hottel 1942) while others attempt to include secondary sources

such as ground reflected radiation (Perez et al. 1990). Given the number

of different approaches in the literature, a comparison of various diffuse

radiation models is given in Section 2.2.6. For this study, the HDKR

transposition model will be used to estimate diffuse radiation incident

upon a tilted PV module surface (reference Section 2.4).

2.2.5 Estimates of the Horizontal Components of Beam and Diffuse Radiation Given Global Horizontal Measurements

The general outlines of Sections 2.2.3 and 2.2.4 explain the calculation and estimation of the beam and diffuse radiation components incident on tilted surface, respectively. The difficulty of these approaches is that it is assumed that direct measurements of DNI and horizontal diffuse radiation are available. However, owing to the cost of maintaining such measurement networks, this is not generally the case. For example, DNI measurements require 2-axis tracking sensors that maintain a 90° between the sensor surface and the sun, easily tripling the initial cost over a stationary sensor (King et al. 1997). Given these limitations, it is more common to have global horizontal measurements of irradiance. Such sensors detect all downwelling radiation from the full-sky hemisphere, thereby including beam and diffuse sources of radiation in the reported measurement.

These global horizontal irradiance (E_g or "GHI") measurements are relatively inexpensive and have become very prevalent. However they pose certain difficulties in determining the required quantities of beam and diffuse radiation on tilted surfaces (E_b and E_d), since values of horizontal diffuse and direct normal radiation are needed for their

calculation. In order for these quantities to be estimated, the global

horizontal measurement needs to be separated into horizontal beam and

horizontal diffuse components so that the transposition procedures can

be completed. As discussed in Section 1.2.1, the Oklahoma Mesonet Li-

Cor 200S sensors used in this study measure global horizontal radiation,

and thus a separation model must be used.

2.2.6 Selection of Optimal Separation and Transposition Models

The selection of the separation and transposition models for this

study was based upon an extensive verification study (Gueymard 2009).

Using direct measurements of beam and diffuse radiation from south-

facing surfaces at 40° and 90°, global horizontal radiation data and

measurements of DNI from 2-axis tracking units collected at NREL's

Solar Radiation Research Laboratory in Golden, CO, Gueymard 2009

was able to verify the performance of ten transposition models under

various sources of input data. The study was partitioned into sub-optimal

and optimal input scenarios, where optimal data for the transposition

models include actual horizontal diffuse radiation measurements, while

the sub-optimal cases included scenarios where only GHI was available.

For the sub-optimal cases, the four most accepted and widely used

separation models were paired with the ten transposition models and the

corresponding calculations were performed at the 40˚ and 90˚ and tracking array surfaces. The model estimates were then compared against the direct measurements of DNI and horizontal and tilted beam and diffuse radiation, from which Mean Bias Error (MBE) and Root Mean Square Error (RMSE) were computed.

For the purpose of this study, the 40˚ results are of the greatest interest, due to the simulated PV rooftop arrays being oriented at latitude-tilt during simulation, which vary amongst the Mesonet stations used in this study from approximately 34˚ to 37˚. The sub-optimal input modeling results were used to choose the best transposition and separation model, based upon their collective performance, rather than on individual results. The ten transposition models tested were the AHRAE (ASHRAE 2005), Gueymard (Gueymard 1987), Hay (Hay 1979), Klucher (Klucher 1979), Muneer (Muneer 2004), Perez (Perez et al. 1990), Reindl or HDKR (Reindl et al. 1990), Skartveit (Skartveit and Olseth 1987) and Temps (Temps and Coulson 1977) models. A simple isotropic model is also included (Hottel 1942). The four separation models simulated are the Erbs (Erbs et al. 1982), Orgill and Hollands (Orgill and Hollands 1977), Reindl (Reindl et al. 1990) and Maxwell or DISC (Maxwell 1987) models. The Erbs and Orgill models are

univariate, requiring only E_g as input. The Reindl model requires ambient

temperature, relative humidity and the zenith angle in addition to E_g

measurements. The Maxwell/DISC model is bivariate, requiring only E_g

and θ_z. All four models are empirically based, however the Maxwell

approach incorporates a simple physical model (see Section 2.4). All

four models are regarded to be "universal" and are widely used in the

literature (Gueymard 2009).

A review of Gueymard 2009 results establishes the Maxwell/DISC

model as the most accurate, with RMSE errors between 8.2 - 10.2% for

surfaces at 40˚ tilt. Among the ten transposition models paired with the

Maxwell/DISC model, three models had RMSE value of 8.2%, the Hay,

Reindl and Skatveit models (with MBE values of -1.3, -1.0 and -1.5

respectively). The RMSE values at 40˚ tilt indicates that the Reindl

model provides slightly more accurate estimates of diffuse radiation, with

RMSE values of 5.3% and 3.1% for all-sky (any amount of cloud cover)

and clear-sky (<10% cloud cover) conditions respectively, versus

5.5%/5.7% and 3.2%/3.2% for the Hay/Skartveit models.

Although other studies have investigated transposition model

performance (Hay 1986; Kambezidis et al. 1994; Loutzenhiser et al.

2007) and separation model performance (de Miguel et al. 2001; Myers

2008; Torres et al. 2010), Gueymard 2009 is currently the only study that investigates several separation-transposition model pairings and thus its results are viewed as authoritative. Given the revealed superiority of the Maxwell-Reindl coupling, these two models have been chosen for incorporation into this study. A review of these models is present in Sections 2.3 (Maxwell) and 2.4 (Reindl).

2.3 DIRECTION INSOLATION SIMULATION CODE –

THE DISC MODEL

The DISC model was developed by researchers at the Solar Energy Research Institute in the mid 1980s and was described as a "Quasi-Physical Model for Converting Hourly Global Horizontal to Direct Normal Insolation" (Maxwell 1987). Whereas previous methods of calculating direct normal irradiance (DNI) had relied on simple empirical correlations between K_t and K_d or K_n (Bugler 1977; Collares-Pereira; Rabl 1979; Iqbal 1980; Liu and Jordan 1963) which Maxwell 1987 exposes to have strong seasonal, climatological and interannual variations, the DISC model incorporates a physical algorithm representing the properties of surface irradiance processes. Physical models had been successfully created prior to Maxwell 1987 (Randall 1977), however these models required input data for cloud cover,

turbidity, precipitable water vapor, ozone and surface albedo, of which

data for some (i.e. turbidity, ozone, albedo) are rarely available. After

extensive analysis of the relationship between these input variables and

their effects on DNI, Maxwell 1987 established that DNI could be

accurately calculated with only a global horizontal radiation

measurement, E_g and the zenith angle as inputs, through use of a

physical model establishing clear-sky atmospheric radiation limits.

2.3.1 DISC Model Formulation and Calculation of DNI

The DISC model was developed in a sequential fashion with

increasing levels of simplicity. To begin, Maxwell investigated the

seasonal, interannual and climatological variations in the relationship

between K_t, which is the clearness condition (or "global horizontal

transmittance" in Maxwell 1987) introduced Section 2.2.4 and K_n, which

is the direct beam transmittance. The direct beam transmittance is given

as:

$$K_n = \frac{E_n}{E_{ext}}$$
(14)

As mentioned in the introduction of this Section, studies that use

empirical correlations between K_t and K_n or K_d to separate the diffuse

and direct components of global radiation measurements are subject to a

significant degree of variation within these three categories. Using a dataset from Atlanta, GA spanning the years 1980-1982, which included DNI and E_d and E_g measurements, Maxwell first revealed the seasonal variation of the K_t and K_n relationship. For the Atlanta location, this variation was likely caused by strong changes in water vapor and cloud cover, which peak in summer and reach a minima in winter for the region. Although other locations would experience different causes and levels of variation, the Atlanta example was enough to highlight the seasonal variation in this and other correlations. Similar logic follows for the interannual variation, wherein variations for a similar dataset from Las Vegas between 1977 and 1980 were analyzed. Maxwell concluded from this and data from subsequent stations, that the random variations between yearly correlations would introduce small, but important variations that would cause errors in any simple empirical correlations. Lastly, data from six locations were compared and once again revealed varying relationships between K_n and K_t that were caused by varying climatological regions. Given these findings, Maxwell concluded that "using a single regression relationship between K_n and K_t apparently will not work well at all stations or at the given station for all seasons".

Maxwell then analyzed the relationships between K_n and K_t and the individual parameters known to modify them. Air mass, cloud cover, turbidity and precipitable water vapor were all investigated. After initial inspection, both albedo and turbidity were eliminated at this juncture due to their measurement being relatively uncommon, and, in the case of turbidity, for fear of the results being biased toward conditions that "favored turbidity measurements". Correlations matrices were produced and parametric studies conducted using the previously introduced Atlanta dataset, which was complimented by cloud cover (CC) and precipitable water vapor (PWV) observations from the nearby Atlanta airport. In order to isolate the effects of individual parameters, data subsets were created and grouped according to arbitrary ranges of AM, CC and PWV, plotting the results against K_n and K_t as well as ΔK_n and ΔK_t. ΔK_n and ΔK_t represent the departure of the transmittance value from its maximum clear sky value (K_{nc} and K_{tc}), which are empirically determined from the Atlanta dataset. These are termed herein as "limiting values" with the relationships given by:

$$\Delta K_n = K_{nc} - K_n \tag{15}$$

and

$$\Delta K_t = K_{tc} - K_t \tag{16}$$

Through this approach, Maxwell found strong similarities in the plots of cloud cover and precipitable water vapor versus the K_n, K_t, ΔK_n and ΔK_t calculations. These strong correlations were interpreted to indicate that "the use of cloud cover data to modify equations relation K_n and K_t will account for much of the variance attributable to both cloud cover and precipitable water vapor" (p. 17). This conclusion therefore omits the PWV variable from inclusion in the DISC model, and reduces the model to dependence on two remaining variables: cloud cover and airmass. Furthermore, given this simplification and the fact that CC and PWV observations do not always accompany global horizontal radiation measurements, it was decided at this juncture that the DISC model formulation would not directly include them. The clearness condition K_t was chosen to account for cloud-cover effects, which is appropriate since cloud cover strongly modulates K_t. The implementation of this is found in the coefficient calculations for a, b and c below, in which two separate empirical relationships dependent on the value of K_t were used in order to improve the accuracy of this assumption.

Given the aforementioned investigations and inclusions, three hypotheses about how DNI, or E_n, might best be calculated from E_g were formed. The first assumes that air mass is the dominant parameter in

the relationship between K_n and K_t. Secondly, changes in K_n can best be

calculated through a physical model that predicts K_n from air mass

values. Third, it is assumed that the seasonal, interannual and

climatological variations between K_n and K_t can be accounted for via an

equation in K_t that relates ΔK_n to AM and thus only one ubiquitous set of

equations would be necessary.

Using these experimentally determined hypotheses, only a few

additional relationships were required to complete DISC model

development. First, the Bird clear-sky model (Bird 1981) is used to

establish clear-sky direct beam transmittance limiting value, K_{nc}, and is

given by:

$$K_{nc} = 0.866 - 0.122 \cdot AM + 0.0121 \cdot AM^2 -$$

$$0.000653 \cdot AM^3 + 0.000014 \cdot AM^4 \qquad (17)$$

Next, a relationship for ΔK_n is developed from the exponential

relationship between AM and ΔK_n which was discovered through a least

squares regression analysis of subsets of K_t values in which ΔK_n was

plotted against AM for each subset. The relationship is given as:

$$\Delta K_n = a + b \cdot \exp(c \cdot AM) \qquad (18)$$

The coefficients a, b and c were found be computable via polynomial functions, resulting a continuous algorithm for calculating ΔK_n, K_n and E_n. The coefficient polynomials are expressed in terms of K_t:

If $K_t \leq 0.60$ (cloudy conditions),

$$a = 0.512 - 1.56 \cdot K_t + 2.286 \cdot K_t^2 - 2.222 \cdot K_t^3 \tag{19}$$

$$b = 0.370 + 0.962 \cdot K_t \tag{20}$$

$$c = -0.280 + 0.932 \cdot K_t - 2.048 \cdot K_t^2 \tag{21}$$

If $K_t > 0.60$ (mostly clear conditions),

$$a = -5.743 + 21.77 \cdot K_t - 27.49 \cdot K_t^2 + 11.56 \cdot K_t^3 \tag{22}$$

$$b = 41.40 - 118.5 \cdot K_t + 66.05 \cdot K_t^2 + 31.90 \cdot K_t^3 \tag{23}$$

$$c = -47.01 + 184.2 \cdot K_t - 222.0 \cdot K_t^2 + 73.81 \cdot K_t^3 \tag{24}$$

Thus given the clear-sky limiting value for beam transmittance, K_{nc} and the departure from this value, ΔK_n which is given by an exponential relationship between relative air mass, AM and the coefficients a, b and c to K_t, the direct beam transmittance is then calculated by:

$$K_n = K_{nc} - \Delta K_n \tag{25}$$

Which, by definition of K_n, yields the direct normal irradiance as:

$$E_n = E_{ext} \cdot K_n \tag{26}$$

38

Once E_n is known, the geometrical calculations of E_b and E_{bh} are performed as outlined in Section 2.2.3.2. Then, given the values of E_g and E_{bh}, the separation of gobal horizontal irradiance E_g into horizontal and diffuse components, E_{bh} and E_{dh}, is simply:

$$E_g = E_{bh} + E_{dh} \qquad (29)$$

2.4 THE HAY-DAVIES-KLUCHER-REINDL (HDKR) TRANSPOSITION MODEL

As outlined in Section 2.2.4, the transposition of the horizontal component of diffuse radiation to a tilted surface is not straightforward. The estimated component of diffuse horizontal radiation (E_{dh}) provided indirectly by the estimate of E_n from the DISC model cannot be transposed by geometry alone (as in the transposition the horizontal beam component). A titled module will receive circumsolar, isotropic (full-sky), horizon brightened and ground reflected diffuse radiation that vary with solar position, sky conditions and module orientation. As a consequence, the diffuse radiation on a tilted surface must be estimated through a model. The HDKR transposition model provides the most accurate estimates of diffuse radiation incident upon a tilted module, particularly when paired with the DISC model (Gueymard 2009), and thus is the model of choice for this study.

The HDKR model represents the combined efforts of three separate works, beginning with Hay 1979, adding a correction factor for cloudy conditions from Klucher 1979 and finally resulting in the form used herein, outlined in Reindl, Beckman et. al. 1990.

2.4.1 The Hay-Davies Model

The Hay- Davies (Hay 1979) model estimates the diffuse radiation incident upon a tilted surface from both circumsolar and isotropic diffuse sources. These two sources are partitioned by the anisotropy index which was expressed as:

$$A_i = \frac{E_n}{E_{ext}}$$ (30)

It is clear that A_i is equivalent to the direct beam transmittance K_n as used in the DISC model (defined in Section 2.3). This anisotropy index will approach unity under clear sky conditions and will be reduced to a minimum under cloudy conditions. In this manner, the portion of E_d that is determined to be isotropic will be increased/decreased and the remaining fraction of E_d will be considered circumsolar and will decrease/increase as K_n (clearness) decreases/increases.

The Hay-Davies model assumes circumsolar radiation (E_{d_cir}) to be projected onto a module surface with the same geometric relationship as beam radiation, yielding the relation:

$$E_{d\_cir} = E_{dh} \cdot K_n \cdot R_b \qquad (31)$$

Where R_b is the geometric factor. The geometric factor is the ratio of beam radiation on a tilted surface to beam radiation on a horizontal surface and is expressed as:

$$R_b = \frac{E_b}{E_{bh}} = \frac{\cos(\theta_a)}{\cos(\theta_z)} \qquad (32)$$

And the remaining diffuse radiation is isotropic (E_{d_iso}) given by:

$$E_{d\_iso} = E_{dh} \cdot (1 - K_n) \cdot \left(\frac{1 + \cos(1 + \alpha_m)}{2} \right) \qquad (33)$$

Therefore, when combined, the total diffuse radiation for a module at tilt α_m is:

$$E_d = E_{dh} \cdot \left[(1 - K_n) \cdot \left(\frac{1 + \cos(1 + \alpha_m)}{2} \right) + K_n \cdot R_b \right] \qquad (34)$$

2.4.2 Modifications by Reindl 1990

Reindl 1990 concluded that the Hay and Davies model could be improved through the inclusion of a horizon brightening source term. This horizon brightening term was first considered by Temps and

Coulson 1977 who applied the following correction factor to the isotropic

diffuse radiation term:

$$\left[1 + \sin^3\left(\frac{\alpha_m}{2}\right)\right]$$

(35)

however, the modification was only found to be valid under clear sky

conditions.

Through additional manipulations by T.M. Klucher (Klucher 1979),

the horizon brightening factor was made applicable to all cloud cover

conditions through an additional modulating factor:

$$F = \left[1 - \left(\frac{E_{dh}}{E_g}\right)^2\right]$$

(36)

This modulating factor, when applied to the sine term of the horizon

brightening modification, forces the correction factor to 1 and the model

to fully isotropic under cloudy conditions. For clear conditions, the

modulating factor has a value less than one and the horizon brightening

correction factor is retained.

The Klucher and Temps and Coulson modeling concepts formed

the basis for the final version of the HDKR model in Reindl 1990. While

the horizon brightening factor of Temps and Coulson remained

unchanged, Reindl 1990 introduced alterations to the Klucher modulating

factor after testing various alternate forms. In the final model version, the

following modulating factor was adopted:

$$f = \sqrt{\frac{E_{bh}}{E_g}}$$
(37)

The result was a new anisotropic model that estimates the magnitude of

diffuse radiation incident upon a tilted module from isotropic, circumsolar

and horizon brightening sources:

$$E_d = E_{dh} \cdot \left[(1 - K_n) \cdot \left(\frac{1 + \cos(1 + \alpha_m)}{2} \right) \cdot \left(1 + f \cdot \sin^3\left(\frac{\alpha_m}{2} \right) \right) + K_n \cdot R_b \right]$$
(38)

The first term in the HDKR model accounts for the isotropic diffuse

radiation. This term also includes horizon brightening considerations

through the modulating factor f, which, under cloudy conditions

approaches zero, along with the anisotropy index (K_n), leaving fully

isotropic conditions. When conditions are cloud-free, all terms are non-

zero owing to K_n never completely reaching unity, but circumsolar

radiation will be the dominant source.

2.5 SANDIA PHOTOVOLTAIC ARRAY PERFORMANCE

MODEL

With global horizontal radiation measurements successfully

separated to beam and diffuse components, and their corresponding

quantities transposed to a tilted surface, these estimates are then

ingested into the Sandia Photovoltaic Array Performance Model (King

2004), herein tilted the "Sandia Performance Model" or SPM. The SPM

uses the tilted beam and diffuse radiation components to predict direct-

current (DC) output from a photovoltaic module selected from a module

database. This database contains module specific empirically derived

coefficients, developed through extensive field testing, that are

accompanied by a series of performance equations which predict module

power output given environmental conditions (radiation, temperature and

wind speed) and the electrical, thermal and optical properties of the

selected module.

The SPM's performance has been validated through seven years

of outdoor testing for flat-plate photovoltaic modules (the type simulated

in this study) of nearly all available technologies through work by several

laboratories and independent testing organizations (Eckert 1996; Fanney

et al. 2009; Fanney 2002; Kroposki et al. 2000; Whitaker 1997). The

model's success has even lead to the incorporation of major SPM core

elements into NREL's PVWatts photovoltaic prediction system, which is

widely used (Anderberg 2006; Marion 2010). Additionally, commercial

manufacturers and system integrators actively contribute information

about their modules to the SPM database and also use the SPM in

system design software (Maui Solar Energy Software Corporation 2004).

2.5.1 Sandia Performance Model Performance Equations

The SPM predicts photovoltaic module power output through a

series of performance equations created from over twelve years of

development at Sandia National Laboratories. The equations describe

the electrical performance of a single photovoltaic module and can

reproduce five points on the I-V (aka "Power") Curve, including the power

output at the short-circuit current, power output at open-circuit voltage

and the maximum power point (P_{mp}). For the purpose of this study, only

the maximum power point will be calculated. Deviation from this point on

the power curve is uncommon for grid-tied photovoltaic modules, as the

voltage and current levels are held steady, even under varying solar

radiation conditions, due to the consistent flow of incoming power from

the electric grid (Engerer 2010). This study will only consider grid-tied

photovoltaic systems.

In order to calculate P_{mp}, the voltage at maximum power, V_{mp}, and

the current at maximum power, I_{mp}, are required, and are given by:

$$I_{mp} = I_{mpo} \cdot \left(C_0 \cdot E_e + C_1 \cdot E_e^2 \right) \cdot \left[1 + \alpha_{Imp} \cdot \left(T_c - T_o \right) \right]$$ (39)

$$V_{mp} = V_{mpo} + C_2 \cdot N_s \cdot \delta(T_c) \cdot \ln(E_e) + C_3 \cdot N_s \cdot \left[(T_c) \cdot \ln(E_e) \right]^2 + \beta_{Vmp}(E_e) \cdot (T_c - T_o) \quad (40)$$

Maximum power is then simply given by:

$$P_{mp} = I_{mp} \cdot V_{mp} \quad (41)$$

Parameters are defined in (Appendix D). Further equations and some additional explanation are needed for a few of the above parameters.

2.5.1.1 Thermal Voltage and Cell Temperature Calculations

The thermal voltage of a cell, $\delta(T_c)$ accounts for voltage drops resulting from circuitry level inefficiencies that arise as solar cell temperature increases. The thermal voltage is given by:

$$\delta(T_c) = \frac{n \cdot k \cdot (T_c + 273.15)}{q} \quad (42)$$

In order to calculate thermal voltage, an estimation of individual cell temperature (T_c) must be made from module temperature ™ by:

$$T_c = T_m + \frac{E}{E_o} \cdot \Delta T \quad (43)$$

Where E is the solar irradiance on the module surface and ΔT is the temperature difference between the cell and the module back temperature, which is module specific and given by the module database. Module temperature is either directly measured or it can be estimated using

46

ambient temperature and wind speed through the thermal model

provided by King 2004:

$$T_m = E \cdot \left[\exp(a + b \cdot WS) \right] + T_a \qquad (44)$$

Where parameters are defined in (Appendix D).

2.5.1.2 Calculation of Effective Irradiance (E$_e$)

The SPM accepts radiation input in terms of effective radiation E$_e$

which is calculated according to:

$$E_e = f_1(AM_a) \cdot \left[\frac{E_b \cdot f_2(\theta_a) + f_d \cdot E_d}{E_o} \right] \cdot SF \qquad (45)$$

This equation provides the portion of the total radiation incident

on the module surface that will be used by the module for energy

production. It accounts for variation in the solar spectrum as a function

of absolute air mass AM$_a$ through the empirical function f$_1$(AM$_a$) as well

as for optical losses incurred by θ_a, the angle of incidence, in f$_2$(θ_a):

$$f_1(AM_a) = a_0 + a_1 \cdot AM_a + a_2 \cdot AM_a^2 + a_3 \cdot AM_a^3 + a_4 \cdot AM_a^4 \qquad (46)$$

$$f_2(\theta_a) = b_0 + b_1 \cdot \theta_a + b_2 \cdot \theta_a^2 + b_3 \cdot \theta_a^3 + b_4 \cdot \theta_a^4 + b_5 \cdot \theta_a^5 \qquad (47)$$

Where the coefficients a and b are module specific and empirically

determined through extensive testing at Sandia National Laboratories.

Absolute air mass (AM_a) can be calculated from the relative air mass (AM) and given by:

$$AM_a = AM \cdot \exp(-0.0001184 \cdot \eta)$$
(48)

Where η is the station elevation (above sea level) in meters.

2.5.2 Performance Equations for Module Arrays

The SPM performance equations in 2.5.1 can be applied to arrays of PV modules. Module arrays are constructed of parallel and series strings, where M_s is the number in series and M_p is the number in parallel. Extending these equations to the array level is done simply through multiplying the maximum power voltage (V_{mp}) by M_s and the maximum power current I_{mp} by Mp. In this manner, the power production of the entire array is based on the performance of individual modules. King 2004 admits that this is "slightly optimistic" since array-level losses, such as those caused by module mismatch and additional wiring resistance, are not included in the calculation. King estimates these effects result in losses up to 5%.

2.6 PERFORMANCE MODEL FOR GRID-CONNECTED PHOTOVOLTAIC INVERTERS

The power output generated by photovoltaic arrays systems is direct-current electricity (DC) meaning that the flow of electrons is consistently in one direction. However, the electricity delivered to consumers by electric utilities is in the form of alternating-current (AC), meaning that the flow of electrons is continually reversing its direction (at about 60 times a second in the United States). This requires than an inverter to be a part of the photovoltaic system. An inverter converts the DC electricity output by the array into AC electricity, which is compatible with the electricity arriving from the electricity grid and is usable by household devices. As a result, in order to produce usable kilowatt-hour power production estimates from a rooftop photovoltaic system, the modeling of an inverter system is required.

Sandia National Laboratories has produced an inverter modeling system, designed to be easily integrated into the Sandia Performance Model and provide power output statistics in terms of AC electricity (King 2007). This model was developed empirically through extensive field-testing of inverters tethered to grid-tied photovoltaic systems for both residential and commercial sized systems. In conjunction with such testing, an inverter model database of the parameters needed for system simulation has been developed and is continually being augmented

through testing at Sandia National Laboratories. The resultant model and database were tested in well-controlled laboratory measurements and validated, with a standard error of approximately 0.1% between modeled and measured inverter performance.

2.6.1 Model Development

The primary purpose of the development of the IPM was to create one ubiquitous model applicable to all commercially available inverter systems through an algorithm that accurately predicts AC power output from DC power input. The model is not based off of engineering level circuitry models, as is used in their development, but rather is an "empirical, or phenomenological model that simply but accurately replicates the power delivery characteristics of the dc to ac inversion process" (King 2007).

Manufacturer specifications of inverter specifications provide invaluable information about inverter characteristics and behaviors, however, this information must be supplemented by third-party testing laboratories in order provide the information needed by any inverter modeling system. Such third party testing is handled according to the specification of Sandia National Laboratories and BEW (Behnke, Erdman & Whitaker Engineering) and is conducted a variety of power levels and

over several separate testing sessions (Bower 2007). Furthermore, the

database is augmented by hundreds of field measurements in which

inverter data points are recorded from modules under representative

operating conditions. This rigorous testing provides the needed empirical

data for accurately modeling the given inverter system, including the

losses due to inverter inefficiencies, wherein energy can be lost to heat

or power levels exceeding inverter modeling specifications.

2.6.2 Inverter Performance Model Basic Equations

Alternating-current output is predicted through the below

equation for P_{ac} which includes the DC power (P_{dc}) and the DC voltage

(V_{dc}) as independent variables.

$$P_{ac} = \left[\frac{P_{aco}}{(A-B)} - C \cdot (A-B) \right] \cdot \left(P_{dc} - B \right) + C \cdot (P_{dc} - B)^2 \tag{49}$$

Where:

$$A = P_{dco} \cdot \left[1 + C_1 \cdot \left(V_{dc} - V_{dco} \right) \right] \tag{50}$$

$$B = P_{so} \cdot \left[1 + C_2 \cdot \left(V_{dc} - V_{dco} \right) \right] \tag{51}$$

$$C = C_0 \cdot \left[1 + C_3 \cdot \left(V_{dc} - V_{dco} \right) \right] \tag{52}$$

CHAPTER 3: MODEL EXECUTION

In order to make predictions of rooftop photovoltaic array performance in Oklahoma, the four models outlined in Chapter 2 (DISC model, HDKR model, SPM and IPM) were implemented sequentially in a comprehensive fortran90 simulation code. The developed comprehensive photovoltaic modeling system accepts input global horizontal irradiance values and then separates them into diffuse and beam components via the DISC model. Estimates of these components on a tilted surface (whose orientation is given by the module tilt and azimuth angles α_m and γ_m respectively) are then obtained via the HDKR model. Next, using array design information (see Section 3.1), the appropriate module information is retrieved from the Sandia Module Database and used to model photovoltaic array DC power output through the SPM performance equations outlined in Section 2.5. Finally, an appropriate inverter system is selected and simulated through the IPM to produce estimates of AC power output.

3.1 MODULE SELECTION AND ARRAY DESIGN

The comprehensive photovoltaic model system was used to simulate 2kW rooftop photovoltaic array performance. The arrays were assumed to be south-facing and at a fixed tilt equivalent to the latitude of

the module. Such orientation is termed "latitude-tilt" and provides the

best annual power production compromise for fixed systems (King et al.

2002). In order to create the most relevant end product, rooftop

photovoltaic array design recommendations were obtained through

personal correspondence with Mr. Bob Willis of Sunrise Alternative

Energy, an Oklahoma energy company which installs rooftop PV arrays.

Through this correspondence, a 2kW array system was determined

provide the most economical balance between total cost and energy

production (see Section 4.6) for Oklahoma customers. Based on this

advice, two 2kW arrays designs similar to those Sunrise Alternative

Energy installs in the Oklahoma region were chosen for this study.

3.1.1 2.16 kW Sharp ND-216U1F Array

A 2.16 kW (henceforth referred to as 2 kW) array of 10 Sharp ND-

216U1F modules consisting of a single 10 module string was constructed

for simulation. The array system was coupled with a Xantrex GT2.8

inverter with a 2.8 kW rating. Sharp ND-216U1F modules are

constructed with 60 polycrystalline silicon cells tied in series that are

textured so as to absorb radiation more efficiently (approximately 13.3%

efficient). They are also specifically designed for the fairly rigorous

operating conditions present upon rooftops as well as being lighter than

many comparable cells (~20kg) so as to reduce rooftop stress (Sharp-Electronics-Corporation 2007).

3.1.2 2 kW Sanyo HIP-200BA3 Array

A 2 kW array of 10 Sanyo HIP-200BA3 modules consisting of 2 parallel 5 module strings was constructed for simulation. The array system was coupled with a Fronius IG2000 inverter featuring a 2 kW rating. Sanyo HIP-200BA3 modules are constructed of an amorphous and polycrystalline silicon blend that produces a 16.1% efficient module. They are also constructed in a manner that occupies 20% less space than a traditional module, are considerably lighter than the Sharp modules at 14kg and are constructed for grid-tied applications, making them another ideal module type for rooftop installations (Sanyo-Energy-Corp 2005).

3.2 MODEL INTEGRATION THROUGH OKLAHOMA MESONET DATA

The comprehensive photovoltaic module system was forward integrated through sixteen years (1994-2009) of global horizontal radiation measurements, which were available at five-minute intervals from 108 different station locations. At each five-minute step, GHI values were split into their beam and diffuse components, transposed to the

54

module surface and power predictions were generated through the SPM

and IPM systems. Power output figures were converted to kilowatt-hours

(kWh) and output on the daily and monthly level. Additionally, 10m air

temperature and wind speed observations were also used at five-minute

intervals for the thermal voltage and cell temperature calculations

described in Section 2.5.1.1.

3.2.1 Missing Data

Missing data points were handled on a daily and monthly basis.

Days missing 12 or more GHI observations (one hours worth, or <5%)

were omitted from model integration, and were replaced with the value of

the previous day. This previous day replacement scheme was limited to

no more than five days in a given month. Since daily and monthly power

output values were based on integration into kWh, application of this

elementary previous day replacement approach prevents the

underestimation of monthly total power generation that would result from

missing data points. This is accomplished through the inclusion of days

and months with small amounts of missing data, that would have

otherwise have been omitted from subsequent monthly level analyses.

Furthermore, because the yearly values are also based on integration,

any given year in which there are not twelve subsequent values of

monthly power generation was omitted from the final analysis. Through

the adoption of this simple scheme, a greater number of years were

made available for creating the yearly mean production estimates by

avoiding the omission of an entire year based on the absence of a small

amount of data. Admittedly, a more complex and involved data

interpolation scheme could be implemented with hopes of achieving

greater accuracy in handling the missing data points. However, given

the very limited occurrence of short time frames of missing data (most

missing data events occur during long-term instrument malfunctions), the

potential inaccuracies of previous day replacement scheme are clearly

offset by the inclusion of a much greater number of real observations that

would have otherwise not been included.

Additionally, GHI measurements exceeding 90% of the

corresponding E_{ext_h} value were omitted. Due to extensive data quality

control by the Oklahoma Climatological Survey, such exceptions are not

common and minimally impact the given study.

3.3 MODELING CONSTRAINTS

Several factors relating primarily to solar geometry required the

implementation a few basic constraints on the comprehensive model

system. Model integration was performed for all time steps where GHI

observations were reported to exceed 2 Wm^{-2} and for which the value of the $f_1(AM_a)$ function from Section 2.5.1.2 was greater than zero. For time steps where the angle of incidence (θ_a) exceeded 90°, values of beam irradiance were set to zero and only transposed diffuse radiation was considered. All horizontal beam irradiance values for zenith angles (θ_z) greater than 90° were set to zero and subsequently the corresponding GHI measurement was assumed to be all horizontal diffuse radiation (E_d). For the inverter modeling process, voltage, current and power output were not permitted to exceed the maximum ratings.

3.4 SOURCES OF MODEL ERROR

Due to the nature of this modeling study, there are several sources of significant error which may alter modeling results. These error sources include pyranometer measurement error, radiation modeling error from the DISC and HDKR models and errors incurred during the array or inverter simulation process.

3.4.1 Li-Cor 200S Pyranometer Error

The Li-Cor 200S pyranometer units installed at the Oklahoma Mesonet station locations feature a high stability silicon photovoltaic cell in a weatherproof anodized aluminum case and stainless steel hardware. Optimal operation can be expected for sensors while ambient

temperatures remain between -40 to 65°C, which is well within the range of temperatures expected in the Oklahoma region. The typical accuracy of these pyranometers is ±3% under natural daylight, with a maximum error of ±5% (Campbell-Scientific 1996).

3.4.2 Radiation Modeling Error

As reviewed in Gueymard (2009), the coupling of the DISC and HDKR radiation model comprises the most accurate method for translating GHI values to a southward facing surface tilted at 40°. However this model combination still introduces significant errors when compared against measured values of direct and diffuse radiation at 40° with a Root Mean Square (RMS) error or 8.2%. A Mean Bias Error of -1.0% indicates that an underestimation of the radiation resource is slightly more likely than overestimation.

3.4.3 Performance Model Error

The Sandia Photovoltaic Performance Model and the Inverter Performance Model are both empirically based models (King 2007; 2004). The extensive module and inverter testing under real-time, real-world conditions used to compile their corresponding databases has contributed to very accurate modeling systems. The primary source of error in the SPM arises from module mismatch and wiring resistance

losses in arrays, which are not included in the module database

construction since they are highly dependent upon the size and

construction of a given array. King (2004) suggests the resultant

overestimate of performance will be at most 5%, and in most cases

substantially less (2%) (King 2007). For the IPM, total model error is

estimated by King 2007 as ±1%.

3.4.4 Verification Study of SPM coupled with HDKR Model

Fanney et. al. 2009 performed a verification study of the SPM for

multiple different vertically integrated photovoltaic modules. In this study,

measurements of actual performance of monocrystalline, polycrystalline,

tandem-junction amorphous and copper-indium diselenide modules were

gathered. Additionally, GHI, beam radiation and horizontal diffuse

radiation observations were taken at module location. When these GHI

measurements were used as input into the SPM, the difference between

annual measured energy production and SPM predictions was between

1%-8%. When study results are narrowed to polycrystalline cells, such

as the ones used in this study, annual error range is reduced to 4.99%-

5.63%. Furthermore, the 4.99% annual error value resulted from a

system in which diffuse radiation on a tilted surface was estimated

through the HDKR model (the transposition model used in the present

study) using GHI minus the cosine of incidence angle multiplied by measured direct normal radiation to estimate the horizontal diffuse component. Therefore, this study is quite similar to the current study, except that it uses measured direct normal radiation rather than a model (here the DISC model was used for this purpose). Given Fanney et. al. (2009) results, the error of the comprehensive photovoltaic modeling system incorporated herein is assumed to be no less than 5%.

CHAPTER 4: MODEL RESULTS AND DISCUSSION

Output from the comprehensive photovoltaic modeling system was produced at daily and monthly resolutions. Total array power output was expressed in kilowatt-hours integrated over daily and monthly intervals for each of the 108 station locations. In an effort to produce results in the most accessible manner to end users, mean seasonal and yearly power output and GHI values were spatially interpolated via an Ordinary Kriging method (Isaaks and Srivastava 1990) to produce state-level maps of expected kilowatt-hour power output. Additionally, monthly and daily level results were reviewed for selected stations. At the daily level, three separate cases are presented for days of varying cloud cover type including clear skies, fair weather cumulus and overcast conditions. For these various time scales, patterns in the distribution of power production and GHI were explored, correlating results to observed cloud cover and type and mean precipitation patterns.

4.1 REVIEW OF APPLIED ORDINARY KRIGING METHOD

Ordinary Kriging (OK) is a linear interpolative method based in the field of geostatistics. First developed for applications in mining industry in the 1960s, kriging has now expanded to a wide variety of spatially continuous natural phenomena. Kriging is often referred to with the

acronym B.L.U.E. or "Best Linear Unbiased Estimator". The process is linear since the estimates produced are created through linear weights formed by summations of the estimated variance. It is termed "unbiased" because the mean error m_R is set to zero when error variance σ_R^2 is determined. Lastly, the system is referred to as the "best" since the error variance is minimized in the system solution. Although m_R and σ_R^2 are not known, the formulation of the kriging processes allows the above constraints to be realized via statistical theory (Isaaks and Srivastava 1990).

4.1.1 Ordinary Kriging with Moving Neighborhood

The OK interpolative processes is defined by estimating unknown points at a regular grid, using linear combinations of weights of the known samples (this population is denoted "'l" through "n"). The total number of samples influencing the sum of linear weights may include all available values, or it may be limited by a predefined distance or by a moving neighborhood of nearest neighbors. For the purposes of this study, a moving neighborhood of the 65 nearest stations was used for all maps presented. The use of 65 neighbors produced a smooth and reasonable analysis with respect to the average separation distance between Mesonet stations.

In the OK method applied herein, estimates at unknown points (û) are given by:

$$\hat{u} = \sum_{i=1}^{n} w_i u_i \qquad (53)$$

Where u_i is a sample point and w_i is the linear combination of weights, which are given at each estimation point by:

$$w = C^{-1} \cdot D \qquad (54)$$

Here C is an n x n covariance matrix containing covariance values between each sample point in the defined neighborhood. D is an n x 1 matrix of the covariance values between the current sample point and all other sample points. Qualitatively, C represents the influence of the distance between samples, with larger C values with increased proximity, therefore being a measure of data density. The D matrix provides an inverse distance weighting scheme, in terms of statistical distance. When C^{-1} is multiplied by D, a n x 1 matrix of weights is produced which is then multiplied against the n x 1 matrix of neighborhood sample points (u_i) and the sum is taken. This summation then provides the estimated value û (Isaaks and Srivastava 1990).

4.1.2 The Variogram

The *C* and *D* covariance matrices are formulated through a spatial model of variance known as the variogram. The variogram provides an estimate of the variance as a function of the separation distance h. The variogram model may have many different forms and is constructed through a positive definite fit to a sample variogram, which is determined by the variance between sample points. Construction of the sample variogram requires grouping the distances between sample points into predefined lag-bins whose size is given by an somewhat arbitrary lag-spacing. Variance values between all data points are calculated and grouped according to the lag-bin corresponding to the distance between them. The lag-spacing should be chosen so as to provide a relatively smooth field to which a positive definite function can be fit while maintaining enough detail to represent the behavior of the sample data's spatial variance. The form of the fit function is specific to the sample field and may come in several different forms. For the purposes of this study, a standard exponential variogram function appeared to provide a reasonable fit to the sample variogram points in all relevant analyses.

The exact form of the exponential variogram model is defined by three parameters: the nugget, range and sill.

$$\gamma(h) = nugget + sill \cdot \exp(range \cdot h) \qquad (55)$$

The nugget value should ideally be set to zero, as it represents

measurement error (the value of error at separation distance of zero

$\gamma(h=0)$). The sill value is the maximum value of variance (if the nugget is

non-zero then the maximum value is the sill plus the nugget) and is

termed "sill" because in the absence of a trend, a spatially continuous

variable should reach a plateau in variance. The sill is reached at the

value of the range parameter. These three values are then determined

through a least-squares fit to the sample variogram using the exponential

model.   The end result is a continuous, positive-definite variogram

model, used to predict the variance at any given separation distance.

4.1.3 Sample Variogram and Exponential Fit for Yearly Data

Though a thorough review of the variograms and kriging methods

experimented with to produce the maps in Sections 4.2-4.4 is beyond the

scope of this thesis document, an example variogram is provided in

Figure 4.1.3-1. The provided variogram was constructed from annual

power production estimates from the Sharp 2kW array, and used in the

nearest neighbors ordinary kriging method to create the map in Figure

4.2.2-1.

Sample variogram construction was hindered by suboptimal

allocation of separation distances at short ranges with the nearest pair in

65

the dataset separated by 12.32km. Subsequent station separation

distances are relatively sparse until about 40km as is shown in the

histogram of 10km lagbin station separation distances in Figure 4.1.3-2.

In order to compensate for the relative lack of stations between 0-40km a

variable lagbin scheme was created, with the first four lagbins for the

sample variogram set to 10km, thereafter lagbins were set equal to

15km. Additionally, data points were spatially de-trended by a second-

order least squares polynomial fit in order to remove the very strong

westward oriented trend. This trend is readily apparent with the strong

upward growth in semivariance with increasing separation distance in

Figure 4.1.3-3. This trend correlates with the general increase in GHI

and power production with westward progression across the state, the

causes of which will be thoroughly presented in subsequent Sections.

The resulting sample variogram is represented by the points in Figure

4.1.3-1 with an exponential model fit denoted by the solid line. This

particular variogram model has a nugget = 0.0, sill ≈ 135.0 and range ≈

60.0 km. Variograms models for all map types were analyzed and found

to fit to an exponential function in a similar manner, with the values of the

sill, nugget and range adjusted appropriately for the closest fit to sample

variogram data.

4.2 YEARLY POWER PRODUCTION TOTALS

In this section, estimates of annual power production and GHI values are presented. These estimates were constructed by integrating the output monthly totals over a given year. Any years with missing months were omitted from yearly analyses resulting in an average of 14 years of data being available for each station.

4.2.1 Yearly GHI

To assess the general solar radiation resource in Oklahoma, yearly means of total global horizontal irradiance, as reported directly by the Mesonet were integrated in the same fashion as energy production figures. The resulting values were expressed kWh/m^2 and are presented in Figure 4.2.1-1. Yearly insolation values are at their peak in the Oklahoma panhandle with approximately 1850 kWh/m^2 of accumulated radiation. A steady decrease is apparent with eastward progression until a minimum of approximately 1550 kWh/m^2 in southeastern Oklahoma. The overall western maximum to eastern minimum pattern is a dominant feature in all of the presented figures, the causes of which are investigated in Section 4.5.

It is important to understand that GHI measurements do not translate directly into power production estimates without the

comprehensive modeling procedure outlined in Chapter 2. However GHI

measurements are related to power production in a quasi-linear

relationship as a first order input (King 2004) and thus analysis of the

GHI resource is quite relevant.

4.2.2 Sharp 2kW Array

Predicted annual power output from the Sharp 2kW array is

presented in Figure 4.2.2-1. Unsurprisingly, maximum mean yearly

power production is located in the Oklahoma panhandle at the Kenton

mesonet station (KENT), collocated with the peak insolation value

presented in Figure 4.2.1-1. This maximum point is ubiquitous for all

maps at all time levels, and it is due to the locally arid climate and

subsequent reduction in thick cloud cover, which is further explored in

Section 4.5.1. Yearly predicted power output reaches values over 4000

kWh in this region. It should be noted that the nearest neighbors

interpolation method will include stations far from the prediction points in

the panhandle region in the interpolation weights, leading contours to

encompasses smaller areas and slightly under-predict power production

in the panhandle. From this maximum point, power production

decreases in a fairly linear downward gradient, with N-S oriented

isolines. Upon reaching eastern Oklahoma, the N-S oriented isoline

pattern is disrupted by a local minimum in power production collocated

with the Mt. Herman (MTHE) station in extreme southeastern Oklahoma.

Reasons for this are again explored in Section 4.5.1. Power production

in the southeastern Oklahoma region is reduced by 800-900 kWh from

the maxima in the panhandle with annual power production amounts

estimated to be approximately 3100-3200 kWh.

Given average annual power production estimates, some

measure of variability must also be established. For this purpose, the

interquartile range (IQR) values for the 16 years of power production

estimates is included in Figure 4.2.2-2. IQR values peak in central

Oklahoma, likely due to the variation in the compromise between

competing moist southeastern gulf and dry southwestern air masses

between years. IQR values peak at 275 kWh have a minimum value of

48 kWh. The median value for all prediction locations is 156 kWh, which

yields a 3.5-5% annual variation in power production. Overall, there is a

weak correlation between northerly progression and reduced IQR values.

4.2.3 Sanyo 2kW Array

Yearly power estimates from the Sanyo 2kW array are slightly

reduced compared to the Sharp array. As defined in Section 3.1, this

results from a slightly lower overall rating for the array (2.0 kW versus

69

2.16 kW for the Sharp array). However the overall patterns in the Sanyo

2 kW array map, given in Figure 4.2.3-1, are nearly identical to those

described in the Sharp array, owing to GHI being the sole first-order

input. An absolute maximum in power production occurs in the

Oklahoma panhandle, with annual average production estimated to be

approximately 3710 kWh. Power production values reach a minimum in

southeastern Oklahoma, where they are estimated to be approximately

3000 kWh.

IQR values are shown in Figure 4.2.3-2 and show an overall

similar pattern to the annual Sharp IQR values. The median IQR for all

prediction locations is 148 kWh with a maximum value of 266 kWh and a

minimum of 48 kWh. This mean IQR value gives an annual variation of

3.9-5.0% in power production, when compared to the maximum and

minimum values of mean annual production.

4.3 SEASONAL AND MONTHLY POWER PRODUCTION

TOTALS

Analysis of GHI values and power production estimates were also

grouped into seasonal and monthly categories for analysis to show how

power production is distributed within a given year. Seasonal

categorizations follow a typical tri-monthly scheme (DJF, MAM, JJA,

SON), and the results are presented in map format. Monthly analyses

are provided through box and whisker plots of GHI and estimated power

production for several stations chosen to represent climatically different

regions of Oklahoma with preference towards more population dense

areas, where more potential end users will reside. The stations chosen

for the monthly level analyses are presented in Table 4.3-1 and are

identified in map denoting the 9 separate Oklahoma Climate Divisions of

stations in Figure 4.3-1.

4.3.1 GHI Measurements

Analysis of the seasonal maps (Figures 4.3.1-1 through 4.3.1-4)

reveal a few key patterns in the solar radiation data. First a relative

maximum appears in southwestern Oklahoma that was not as readily

apparent from annual maps. This relative maximum is strongest during

the fall and winter periods.   Secondly, during the spring and summer

periods, the insolation minimum resides in southeastern Oklahoma.

However, in the fall, the minimum shifts suddenly to the northeastern

portion of the state, with iso-insolation lines becoming oriented in NNW-

SSE fashion. In the winter months, this minimum drops slightly

southward to east-central Oklahoma with iso-insolation lines becoming

oriented in a N-S manner. Causes for this shift are explored in Section

4.5.2. It is also apparent that, though similar solar geometry is present,

the spring months experience higher amounts of insolation than the fall

months with a difference on the order of 100 kWh/m^2.

On the monthly level, the box and whisker plots (Figures 4.3.1-5

through 4.3.1-11) reveal similar patterns with slightly more detail. Boxes

encompass the 25th and 75th percentiles with the median denoted by the

solid black line in the box center. Whiskers then extend to the extrema.

Overall, all stations show a clear preference for higher GHI values in the

spring months versus fall months, though solar geometry considerations

are identical. This points to generally reduced solar insolation in the fall

months, the causes of which are discussed in Section 4.5.2. The peak

month for accumulated GHI is July for all stations, with the exception of

the extrema points for June exceeding those for July at the BOIS and

MEDI stations in western Oklahoma. Unsurprisingly, available GHI

increases with westward progression, with the GHI resource at BOIS

exceeding that at MCAL by approximately 20% for each month.

Between seasons, variability tends to be reduced during the winter

months and greatest in the late spring and early summer. A general

pattern of reduced year to year variability between months is present

moving northwest along a northwest-southeast line. This is particularly

evident in the BOIS station plot and to a lesser extent the WOOD station in northwestern Oklahoma.

4.3.2 Sharp 2kW Array

Expected power production from the Sharp 2kW array is presented for the four seasonal periods in Figures 4.3.2-1 through 4.3.2-4. A seasonal shift of the relative minimum to the northeast in the fall and winter months and back to the southeastern part of the state in spring and summer is apparent, although it is admittedly much weaker than that shown in the GHI maps. The intra-monthly power production Figures are characterized by much different patterns than the seasonal GHI values.   Maximum power production in the panhandle region occurs during the spring months, as is apparent in Figure 4.3.2-2, with over 1040 kWh of expected power generation whereas power production is reduced in the summer months to approximately 980 kWh for the panhandle region. This is true for all of western Oklahoma, with the spring months providing greater power production than the summer months as is apparent in comparison of Figures 4.3.2-2 and 4.3.2-3. The same does not hold for eastern Oklahoma, the reasons for which are explored in Section 4.5.2. Power production in the winter months varies between approximately 690 to 935 kWh from southeastern minimum to

the panhandle maximum, with the more populous central Oklahoma region expected to produce approximately 800 kWh as is shown in Figure 4.3.2-1.

The results from Section 4.3.1 and 4.3.2 may seem to be in conflict upon initial investigation. GHI values are at a maximum in the summer months, so naturally one would expect power generation to behave simlarly. However, such is not the case, owing to the fundamental differences in solar geometry between horizontal and titled surfaces. Modules are oriented at a south-facing latitude tilt, which causes optimal angle of incidence (θ_a) values to arrive at the equinoxes, when the maximum insolation is falling upon the equator. The angle of incidence modulates how much direct normal irradiance (E_n) is received at the module according to Equation 11:

$$E_b = E_n \cdot \cos(\theta_a) \tag{11}$$

Additionally, as the sun's average zenith angle decreases into the summer months, the daily sum of beam radiation incident upon a horizontal surface increases. However, for a tilted module, this actually results in larger portions of a day in which θ_a is greater than 90° and no beam radiation is incident upon a module. Furthermore, the extraterrestrial radiation on a normal surface is at a minimum during the

summer months, as the earth is further from the sun during this period. In this manner, the latitude tilt angle compromise results in the greatest annual energy production figures, by considering the manner in which beam radiation arrives at the module over the course of a year (King et al. 2002).

Monthly level power production estimates for the selected stations are given in Figures 4.3.2-5 through 4.3.2-11. These plots will be particularly relevant for solar installation companies and their potential customers due to the level of detail in the box and whisker plots. Power production maximum, minimums and median values are presented, so that expected production and potential variability are captured in one graphical item.   For example, solar installations in the Oklahoma City area could reference the power production estimates in Figure 4.3.2-10 for the Spencer Mesonet station. Information in this figure is relevant to more than 500,000 Oklahoma city residents, as well as the surrounding suburbs. In this figure, median power production reaches its maximum during July with a monthly production of approximately 320 kWh and is at a minimum in November at 260 kWh. The greatest variability in production amounts is present between October and January, with

production varying by as much as 160 kWh during October and November.

The rest of the monthly station plots further elaborate upon the patterns apparent in the monthly maps. Stations in western Oklahoma (BOIS, MEDI, WOOD) exhibit higher median production values during the spring months than do the other stations. Of particular interest is the BOIS station, which exhibits a particularly productive spring season with the relative peak median in March and the median production during of March, April and May all exceeding production during the summer months. This feature is still apparent at the WOOD and MEDI stations in northwestern and southwestern Oklahoma, respectively, where overall, median spring values exceed those of the summer. This is not true for the fall months, owing to increased cloud presence, as explained in Section 4.5.2.

MCAL and BIXB experience peak values in median monthly production during late summer, occurring in July for MCAL with a value of approximately 310 kWh and in August for BIXB with a value of approximately 320 kWh. These differences between eastern and western Oklahoma are attributed to clouds as discussed in Section 4.5. The patterns in cloudiness also help to explain the period of overall

increased variability is during the months between October and February, with variability being noticeably reduced during the spring and summer period for all stations.

4.3.3 Sanyo 2kW Array

Seasonal maps of power production for the Sanyo 2kW array are presented in Figures 4.3.3-1 through 4.3.3-4. Patterns for the Sanyo 2kW array are identical to those for the Sharp 2kW array, but production figures are reduced slightly. During the winter months, the Sanyo 2kW array is estimated to produce 635 to 880 kWh from southeastern minimum to panhandle maximum, a reduction of approximately 60 kWh when compared to the Sharp 2kW array. For the spring period the western portion of the state produces more energy during MAM than during JJA, with production of approximately 980 kWh and 960 kWh, respectively. Conversely, in the southeastern portion of the state, production increased by 40-60 kWh between spring and summer periods. During fall, estimated power production increases from 720 kWh to 920 kWh with progression from the southeastern to panhandle regions of the state.

In Figures 4.3.3-5 through 4.3.3-11, box and whisker plots are again presented for the seven stations in table 4.3.1-1. The overall

patterns are identical to those described in Section 4.3.2 for the Sharp 2kW array, but the magnitude of the results are slightly reduced. In the southeastern and northeastern portions of the state, represented by the MCAL and BIXB stations, respectively, median peak production occurs in July and August with production estimates of approximately 295 and 310 kWh. Median production values fall during the spring and fall months and reach a minimum in December at approximately 205 and 215 kWh for MCAL and BIXB, respectively. Variability is notably increased between October and February, and is greatest in November, with production varying by nearly 180 kWh for the BIXB station. For central Oklahoma, the NRMN and SPEN stations have median energy production peaking in the summer during July at approximately 300 kWh and reach a minimum in November with approximately 240 kWh of energy production. Energy production during the spring and summer months is fairly similar with both September and April producing approximately 275 kWh. Once again, the period of greatest variability falls during the months between October and February.

4.4 INVESTIGATIONS OF DAILY POWER PRODUCTION

In order to investigate how power production might vary within a given day, three separate case studies were chosen for data from the

NRMN mesonet station in conjunction with the Sharp 2kW array. In each

case study, the meteorological conditions present are reviewed in order

to highlight the manner in which they modulate the solar energy

production and subsequent need for accurate forecasts of these

parameters for solar power forecasting. The first, a cloud free day in

July, the second a June day characterized by fair weather cumulus

clouds and the third a completely overcast, snowy December day. For

each case, weather conditions are presented through surface

observations, atmospheric soundings and satellite imagery. Then, the

instantaneous predicted power output is plotted along with the

components of beam, diffuse and effective radiation. The integral of total

power production is also included.

4.4.1 Cloud-Free Day - July 31st, 2005

Synoptic scale conditions on July 31st, 2005 were characterized

(reference Figure 4.4.1-1) by a light southerly surface flow beneath a

surface ridge. Conditions were relatively dry with dewpoint depressions

in the 25-30°F range. The 00Z sounding from OUN (Norman WFO) in

Figure 4.4.1-2 shows very dry conditions at all levels with relatively weak

northeasterly flow aloft. The 15Z and 21Z satellite images in Figures

4.4.1-3 through 4.4.1-4 further confirms that dry, clear, cloud-free

79

conditions dominated by a moderate surface ridge are present in the central Oklahoma region.

Figure 4.4.1-5 presents the distribution of power generation and radiation throughout the day. The effective radiation (green line) is approximately the sum of the beam radiation (blue line) and diffuse radiation (pink line) and shows a steady sinusoidal shape throughout the day. Although no clouds were apparent from the satellite imagery, there was apparently one small cloud event (or other miscellaneous blockage of the instrument) at approximately 16Z. Effective radiation and instantaneous energy production (red line) reaches a peak at local solar noon shortly after 18Z at 925W/m^2 and 1867W respectively. The gold line is the total generated power which reaches a value of 13.5 kWh after dusk. The horn shaped peaks at the edges of the plot result from zenith angles reaching 90° whereupon all of the reported GHI measurement is treated as diffuse within the comprehensive modeling system. Handling of the GHI separation in this manner actually leads to a slight under prediction of the daily power production, and cannot be remedied without adjustments in the formulation of the DISC and HDKR models at extreme zenith angles (see Chapter 2).

4.4.2 Fair Weather Cumulus Day – June 16th, 2003

The surface map in Figure 4.4.2-1 shows weak northeasterly surface winds and dewpoint depressions of approximately 20 degrees in the Oklahoma region. A weak surface boundary is present across central Arkansas and northeastern Texas which is apparent from the associated wind shift. The satellite images in Figures 4.4.2-3 and 4.4.2-4 show convection occurring along this surface boundary, indicating the presence of conditionally stability and environmental lapse rates that are favorable for convection. From 16Z through 22Z, Figures 4.4.2-3 through 4.4.2-5 showing a growing region of fair weather cumulus clouds over the area surrounding Norman, OK. A 00Z sounding from OUN on July 17th (Figure 4.4.2-2) was the closest available sounding for analysis with regards to time, and reveals an elevated moist layer at approximately 850mb, which is likely where the cumulus development was taking place earlier in the day.

A time series of five-minute power production and radiation intervals is presented in Figure 4.4.2-6. Initiation of cumulus convection is apparent around 16Z when effective radiation (green line) begins fluctuating on short time scales. A brief break from the cumulus shadows over the NRMN station is apparent from 19-20Z, but then starts up again thereafter. Closer examination of the beam (blue) and diffuse (pink)

components reveal that as beam radiation is reduced according to the DISC model formulation there is a corresponding increase in diffuse radiation. The compensating increases in diffuse radiation are roughly one-third the magnitude of those in the beam component. This results in a net loss in the effective irradiance and therefore the instantaneous power production. However, the accumulated power production (gold line) for the day was still rather high, with approximately 1242 kWh of power generated. Had clear conditions been present, the estimated power production would likely have been on the order of 1350 kWh as was the case in Section 4.4.1 for the clear day case. It therefore appears that the rapid oscillations present in power production on a day characterized by fair weather cumulus convection do not cause a very large reduction (less than 10%) in power production.

4.4.3 Overcast Day - December 12th, 2003

Surface conditions at 19Z in Figure 4.4.3-1 reveal a developing surface low in north central Texas, with surface temperatures at or slightly above freezing in central Oklahoma. Northeasterly surface flow was present with an east-west oriented warm front draped over the Red River. Freezing rain was occurring in southwestern Oklahoma with steady rain falling in the central part of the state. The 12Z OUN sounding

in Figure 4.4.3-2 shows saturated, cold conditions at the surface with weak northeasterly winds that transitions rapidly to warm, moist southwesterly flow a few hundred meters above the surface. Coupled with satellite images in Figures 4.4.3-3 through 4.4.3-5, it is apparent that thick low-level nimbostratus and stratus clouds are present in the 950-800 mb level before conditions become less saturated above 750 mb. An intrusion of upper level clouds is also likely present at approximately 450mb, given the moisture evident in the sounding and westerly motion in clouds observed in satellite imagery, which is consistent with flow at the 450mb level. This type of storm is fairly common in the winter months for the Oklahoma region, and provides an excellent case study for the overcast conditions and large reductions in the solar radiation resource that occur.

A time series of power production and radiation is presented in Figure 4.4.3-6. Instantaneous power production is greatest during the period between 15Z and 17Z, reaching a peak of 304W at 1510Z. In the 16Z satellite image in Figure 4.4.3-3, the eastern portion of Oklahoma is cloud free, with thin clouds and light surface fog over the central portion of the state, thus during the early hours some brief periods of weak sunshine and a small amount of beam radiation occurred (as seen in the

abrupt peaks in effective radiation). However, by 18Z thick low-level

clouds had completely covered the central Oklahoma region, and

negligible amounts of beam radiation were present. Thus power

production for most of the day is tied directly to the available diffuse

radiation, which accounts for nearly all of the effective radiation input into

the SPM.   Total daily power production was only .59 kWh, a very large

reduction (95%) in potential generation when compared to the fairly

sunny day before, December 11th, 2003, in which 12.75 kWh of energy

production was estimated. Figure 4.4.3-7 provides the 20Z visible

satellite image, in which very sunny clear conditions are apparent. This

is further verified by broad, smooth sinusoidal shape in the power

production and radiation time series from December 11th, 2003 provided

in Figure 4.4.3-8.

4.5 DISCUSSION OF SPATIAL AND TEMPORAL

PATTERNS

In the presentation of the yearly, seasonal and monthly power

production estimates for the 2kW array systems a number of patterns

were identified, the origins of which require further explanation.

Modulation of solar radiation is primarily accomplished by the influence of

clouds, whose shadows reduce available radiation and through a direct relationship with elevation (Section 4.5.1).

In order to identify the causes of patterns in variability and distribution of photovoltaic energy generation attributable to cloud shadows, patterns of cloud behavior must be identified. In the absence of an advanced study of satellite data to determine the cloud cover climatology of Oklahoma, two other sources are considered. The first is a study by McManus 1999 in which a global solar radiation model ingesting hourly observations of pressure, dewpoint, snow cover presence, fractional sky cover and cloud height observations from the years 1952-1991 were used to create a climatology of solar radiation in the Great Plains area (McManus 1999). The second is through the climatological (30 year) averages of precipitation provided by OCS, although most clouds do not create precipitation, increased precipitation does correlate with increased cloudiness and reduced photovoltaic energy generation.

4.5.1 Investigation of the Impacts of Elevation

To investigate the impact of elevation upon power production, a basic empirical approach to estimating the direct normal irradiance at varying elevations under clear skies is employed (Laue 1970). According

85

to work done by Laue 1970, estimates for E_d as a function of air mass and elevation are given by:

$$E_d = 1353 * [(1 - 0.14 * \eta_{km}) * 0.7^{(AM^{0.678})} + 0.14 * \eta_{km})]$$ (56)

According to this relationship, areas of increased elevation will experience greater amounts of direct normal radiation than those of a lower elevation due to the decreased depth of atmosphere through which radiation must travel. This depth is measured by air mass, which was first discussed in Section 2.2.3.1 in Equation 8:

$$AM = \left[\cos(\theta_z) + 0.5057 \cdot (96.08 - \theta_z)^{-1.634} \right]^{-1}$$ (8)

To aid in this analysis, a topographic map of Oklahoma is provided in Figure 4.5.1-1.   An elevation change of over 1220 meters (4000 feet) is present from extreme southeastern Oklahoma to the most western portion of the panhandle. However approximately 600 meters of this elevation increase occurs in the panhandle alone, and when the panhandle is excluded the elevation gradient is significantly reduced. In order to assess the impact of terrain on photovoltaic energy generation through air mass values, three stations along a E-W line from eastern to the western Oklahoma panhandle were selected: VINI, BLAC, BUFF and BOIS (denoted by stars in Figure 4.5.1-1). Elevations for these

stations are 236m, 304m, 559m and 1267m respectively. The predicted E_d values as a function of elevation and air mass values are then plotted in Figure 4.5.1-2 for zenith angles between 13.3° and 72°. The zenith value 13.3° is the minimum zenith angle reached by BUFF, the northernmost station at 36.8° N, which occurs at the summer solstice. The 72° value is the angle at which AM approaches a value of 3 for BUFF. An AM value of 3 was chosen because it is known that approximately 90% of annual energy generation is produced for AM values less than 3 (King 2004) and thus this range of AM values is characteristic of most power generation. In this figure, the mean reduction in E_d between the highest BOIS station (1267m) and the lowest station, VINI (236m) was 7.3% for an elevation difference of 1031m. Between VINI and BUFF (559m) a mean difference of 2.0% was present for a 223m elevation difference whereas in comparison of BOIS to BUFF the difference was 5.3% over an elevation change of 708m.

The estimated increase in DNI values over the elevation gradient from eastern to western Oklahoma is on the order of 7.3% when including the panhandle and a much more modest 2.0% excluding the panhandle. In order to translate the increase of beam radiation intensity with height into approximate differences in power production, power

87

output was simulated using the E_d calculation from Laue 1970 rather than the DISC model for these four stations on the July 31st, 2005 cloud free case (see Section 4.4.1). The results are presented in Figure 4.5.1-3. Difference in power production between the VINI and BUFF and BLAC and BUFF stations, representing 223m and 255m elevation changes were calculated to be 45 and 50 Wh respectively (an approximately 0.4% increase in each case). From VINI to BOIS, an elevation gain of 1031m, the difference was a more sizable 616Wh (a 5.7% increase). The yearly mean values of power production for the VINI and BOIS stations are approximately 3350 kWh and 4100 kWh, an approximately 18% reduction. These very simplified results suggest that for a clear day in summer (assuming minimized influences from other sources, e.g. small differences in aerosols or water vapor) the difference of 5-6% in power production values can be loosely referred to as a theoretical upper-limit for the effects of elevation, leaving at least 10-12% of the difference, or two-thirds of the total difference, in power production to be explained by variation in cloud cover. If the same line of thinking is applied to the difference in yearly mean values between VINI and BUFF stations, a 10% reduction in power production (350 kWh) is present with an upper limit of 0.5% of that difference being attributable to the differences in

elevation between the two stations. This would leave 95% of the

difference between these values to be attributable to causes other than

the change in elevation between these stations. The effects of elevation

discussed herein are therefore considered implicit in subsequent pattern

analyses, and are theorized to account for no more than one-third of the

difference between extreme eastern Oklahoma and the western part of

the panhandle.

4.5.2 Yearly Patterns

In Section 4.2, average annual power production figures from the

2kW Sharp and Sanyo arrays were presented. An overall pattern of

increased GHI and power production with westward propagation across

the state is readily apparent, reaching a maximum in the panhandle

region. Power production is at a minimum in the southeastern region of

the state. Reasons for this (excluding the terrain effects previously

discussed) become apparent in the analysis of Figure 4.5.2-1 from

McManus 1999, which shows the annual mean frequency of different

cloud types. While there is not much of a gradient (less than 10%)

between the western and eastern regions of the state for total fractional

sky cover (FSC), there is notably higher frequency of the low level stratus

clouds in eastern OK when compared to western OK.   Such clouds are

shown to be quite detrimental to photovoltaic energy generation in Section 4.4.3 due to an inherently thick optical depth. This is not the case for high-level cirrus, which typically have a much shallower optical depth while remaining quite broad in total extent. Thus, although fractional sky cover may not vary greatly between these two regions, the differences in optical depth of the clouds accounting for the FSC would result in western Oklahoma receiving considerably greater amounts of beam radiation.

The general increase in cloudiness between eastern Oklahoma and western Oklahoma is further supported by the 30 year climatological average precipitation amounts presented in Figure 4.5.2-2. The annual precipitation maximum in southeastern Oklahoma is nearly collocated with the annual energy production minimum in Figures 4.2.2-1 and 4.2.3-1. The southeastern minimum grows along with a general westward decrease in total precipitation, closely mimicking that of the average annual power generation (although with an inverse relation). Also of interest is that there is a general thickening of optical depths in clouds that produce precipitation, easily observable to the casual observer in that "dark skies" are a reliable indicator of the presence of precipitation. In this manner, areas that receive higher values of precipitation, will likely

account for greater reductions in available radiation than those that experience equal fractional sky cover, although this suggested relationship is strictly qualitative.

4.5.3 Seasonal Patterns

In Section 4.3 the seasonal patterns in predicted in GHI and solar energy generation were discussed, however causes for these features were not presented in detail. Using climatological precipitation means and the cloud cover analysis provided by McMann 1990, reasons for the seasonal behavior of the 2kW solar energy arrays and measured GHI values are explored.

To begin, an analysis of mean seasonal GHI values is presented. Maps of mean seasonal GHI values are presented in Figures 4.3.1-1 through 4.3.1-4, showing a northeastward propagation of minimum GHI during the fall and to followed by a sagging slightly south to eastern Oklahoma during the winter months. This signal follows the climatological mean seasonal precipitation patterns for winter and fall presented in Figures 4.5.3-1 and 4.5.3-4. Note, the 11 inch precipitation contour in Figure 4.5.3-4 should be followed by additional contour levels as the sum of monthly fall mean precipitation in the eastern portion of the state exceed 18 inches in some locations. For verification, Figures 4.5.3-

5 through 4.5.3-7 show the climatological mean precipitation for September, October and November, respectively. Mean seasonal precipitation is at a maximum in southeastern Oklahoma during the spring months, being roughly collocated with the mean minimum values for GHI. Collocation for precipitation maximum and GHI minimum is not present in the summer months, suggesting that non precipitation producing cloud types must have been dominant. This conclusion is supported by results in McMann 1999 wherein cirrus cloud types reach a maximum and stratus cloud reach a minimum in terms of percentage of sky cover during the summer months (Figures 3.3a-3.3l). Westward movement across the state shows fairly close agreement between the structure of rainfall and GHI contour levels for all seasons save the fall, where NNE-SSW oriented mean rainfall contours suggest a different pattern than the NW-SE oriented mean GHI contour lines.

Investigation of the seasonal maps of energy generation from the 2kW array systems reveal even closer correlation between increased rainfall and reduced energy generation contours. Figures 4.3.2-1 through 4.3.2-4 and 4.3.3-1 through 4.3.3-4 display seasonal maps of solar energy generation for the Sharp and Sanyo 2kW arrays. Beginning with the winter months, there is a collocation of the southeastern rainfall

maximum and energy generation minimum with NNE/SSW oriented

contour lines gradually gaining N-S orientation with westward

propagation across the state. In spring, a very slight shift northward is

presented in the collocation feature, with close agreement maintained

between rainfall maximum and energy production minimum. With the

arrival of summer, as with the GHI comparison, the close agreement

between this minimum/maximum feature is lost, as is the case with GHI

values owing to non-precipitation producing cloud types being dominant

(Cirrus and Altocumulus, McMann 1999). Progressing into autumn,

Figures 4.5.3-5 through 4.5.3-7 allow for inference of the fall rainfall

maximum being located in roughly the same location as is seen in

October. This once again provides collocation between solar energy

generation minimum and rainfall maximum for the fall months.

4.5.4 Monthly Patterns

Month to month variations in GHI values within a given year are

much more pronounced than those for power generation for tilted

modules, owing to optimal solar geometry (maximum zenith angle and

angle of incidence) for flat surfaces arriving in the summer months while

the optimal angle for surfaces at latitude tilt are present at the vernal and

autumnal equinoxes. From their peak in the summer, GHI values then

reach a pronounced minimum value during the winter (at the winter solstice) leading to a strong sinusoidal shape with a yearly period in the monthly progression of GHI values (apparent in Figures 4.3.1-5 to 4.3.1-11). This sinusoidal pattern is much less pronounced in the energy generation by tilted modules owing to the solar geometry factors impacting beam radiation, as is discussed in detail in Section 4.3.2. Direct normal extraterrestrial beam radiation is at minimum during the summer months while the earth is at its greatest distance from the sun. Additionally, the utilizable beam radiation, determined by the angle of incidence (a function of zenith angle and module tilt), reaches a maximum at the equinoxes. This combination of factors results in the mean value of effective radiation and the resulting energy having a sinusoidal behavior with one half of the wavelength of GHI values, peaking in both the spring and the fall and reaching a relative minimum in summer and an absolute minimum in the winter, given cloud free conditions. The result of this pattern is apparent in the box and whisker plots of estimated power production for the BOIS station in Figures 4.3.2-6 and 4.3.3-6. This location provides the most arid and relatively cloud free conditions available, and thus the influence of the sinusoidal behavior of the beam radiation component is most pronounced at this

station. It also apparent in the generally more arid, cloud free western stations that peak energy production may occur in March or October, as is the case with the tail end distributions in the box and whisker plots for the BOIS and WOOD stations.

Through further analysis of these box and whisker plots of monthly power production estimates it is apparent that variability in potential power production increases suddenly from a minimum in the summer months to a maximum in October and November for the central and eastern Oklahoma stations: BIXB, MCAL, SPEN and NRMN. For western Oklahoma stations (MEDI, WOOD, BOIS) this maximum point in variability arrives in late winter in February, rather than in the spring. The overall pattern of increased variability correlates well with cloud cover and precipitation patterns. In Figure 4.5.4-1 mean monthly fractional sky cover percentages as determined by McMann 1999 show cloud cover at a minimum in the summer months reaching its nadir in August. Cloud cover then increases steadily through fall, reaching a maximum in January. This is supported by the seasonal maps of mean precipitation in Figures 4.5.3-1 through 4.5.3-7, which show precipitation amounts peaking in spring and fall.   Reductions in absolute available atmospheric moisture and increased amounts of frozen precipitation are

expected during the winter months, so a reduction in overall precipitation totals is present though fractional cloud cover reaches a maximum.

4.6 COST-BENEFIT ANALYSIS

In order to further aid in determining the value of a 2kW rooftop array installation, a simple cost benefit analysis has been performed. Installation costs for 2kW systems, per estimates for comparable systems from Sunrise Alternative Energy are provided in table 4.6-1. Using the mean energy production figures for the seven stations used in Section 4.3, the approximate number of years required to pay off the system are provided in table 4.6-2. These calculations are based on current electricity costs as provided by OG&E, an Oklahoma electric utility, which sells power for approximately $0.10/kWh (OG&E Energy Corp 2011). Time to payoff is approximately 24-30 years for a Sharp 2kW array and 28-34 years for the Sanyo 2kW array.

It is worthy to note that such ranges are likely large exaggerations. This occurs for several reasons. First, costs of electric power generation are likely to rise substantially over the next few decades with a general world-wide increase in energy demand (International Energy Agency 2010b). With the introduction of time of use pricing, which will cause electricity prices to rise to approximately $.25-$40 kWh at peak use

between 2pm and 7pm, payoff rates will likely be reduced by many years

(OG&E Energy Corp 2011). Especially considering that peak power

output from the rooftop arrays is located at mid-day, with a large portion

of daily power production collocated with peak rates. A much more in-

depth study of the timing of solar energy production versus variable

power pricing is needed for more accurate pay-off time periods to be

calculated.

CHAPTER 5: CONCLUSIONS

5.1 SUMMARY

The photovoltaic translation system created herein has provided a means to produce predictions of photovoltaic performance in the state of Oklahoma. Through a combination of four separate modeling systems, global horizontal radiation measurements from the Oklahoma Mesonet are able to be translated to power production estimates for any of the 500+ solar energy devices in the ever-growing Sandia Module Database (King 2004). The first of these models, the DISC model (Maxwell 1987) estimates the magnitude of direct normal radiation through the use of a quasi-physical model and GHI and zenith angle calculations. Estimation of this component allows the GHI measurements to be separated into direct and diffuse components. Next, estimates of the direct and diffuse radiation incident upon a tilted module surface are needed. The direct component is provided through simple solar geometry; however, the HDKR transposition model (Reindl et al. 1990) is required in order to estimate the diffuse component. At this juncture, the total radiation resource available to a tilted module is now known, and is ingested into the Sandia Performance Model (King 2004). This empirical model is built off of years of extensive testing of module performance testing, and

when coupled with the Inverter Performance Model (King 2007) predicts alternating-current power output. In this manner the GHI measurements from the Oklahoma Mesonet are translated into instantaneous power production.

Using this comprehensive photovoltaic modeling system, the performance of two different 2kW rooftop sized arrays and associated inverters was simulated for 16 years of available solar radiation data (1994-2009). Through correspondence with Mr. Bob Willis of Sunrise Alternative Energy, an Oklahoma renewable energy company that installs solar arrays, two specific 2kW systems were designed. The first was a 2.16 kW array of ten Sharp ND-216U1F polycrystalline photovoltaic modules paired with a Xantrex GT2.8 inverter. The second was a 2.0 kW array of ten Sanyo HIP-200BA3 modules with a Fronius IG2000 inverter device. Both designs are created to directly mimic the types of rooftop array systems that would currently be installed by Oklahoma residents. In this manner, potential end users may consult the results in Chapter 4, which are presented in easily interpretable kilowatt-hour output, to determine the likely power output of 2kW south-facing, latitude tilt rooftop array at their location. Chapter 4 presents yearly (Section 4.2) and seasonal mean power production in map format, while

median, quartiles and extrema are available at the monthly level for selected locations in the form of box and whisker plots (Section 4.3). Additionally, a limited review of case studies at the daily level explore how specific meteorological phenomena impact power generation (Section 4.4). Finally, causes for the patterns in the distribution of power generation minima/maxima are found to be closely collocated with areas of increased/decreased cloud cover through analysis of climatological mean precipitation and cloud cover observations while increased power output due to increased elevation is found to be only of consequence in the panhandle region (Section 4.5)

5.2 LIMITATIONS

The developed translation system could benefit from a wide variety of improvements. Foremost, verification of the model system predictions against photovoltaic systems currently in operation within the state of Oklahoma is needed. Potential sources of error were outlined in Chapter 3 and included pyranometer error, error in the radiation models (DISC and HDKR models) and error in the Sandia and Inverter Performance Models (SPM and IPM respectively). The collective impact of these errors upon the power output predictions of the translation system is not known, but could be evaluated through a future verification

study. Additionally, the translation system has been developed in a manner that does not include the potential impacts of shading or blockage, ground reflected radiation or the effects of topography. Improvements to the handling of missing data (Section 3.2.1), calculations of solar geometry variables, as well as the efficiency of the ingestion and processing of Mesonet data could all be made. The accessibility of the model could benefit from a more easily operable interface that allows a user to select their location, module type, size and orientation to evaluate the potential energy resource of a photovoltaic installation.

5.3 FUTURE DIRECTION

Other potential applications of this photovoltaic translation system include solar energy resource assessments, researching the impacts of meteorological events on solar power generation, and possible implementation of the translation system into a solar power forecasting framework. In terms of resource assessment, the developed translation system could be scaled up to produce output statistics for hundreds or thousands of arrays. This would then provide electric utilities or policy makers with an estimation of the energy resource in the region under consideration. At a smaller scale, this translation system could also be

applied to resource assessment at the university or community level,

simulating a smaller network of photovoltaic arrays in a similar manner.

Additionally, the model could be used to investigate how power

production may vary given within a given day based on the impacts of

different weather systems elaborating further on the work in Section 4.4.

This is, again, of particular interest when applied to the impacts of a large

number of grid-integrated PV systems. Data from the Oklahoma

Mesonet provides a particularly unique and valuable resource for such

research. Finally, it is believed that the developed modeling system

could be eventually incorporated into a solar energy forecasting system,

although the coarse nature of radiation parameterizations within

numerical weather prediction models would likely limit explicit power

prediction. Applications of this and other translation systems to the

creation of solar power forecasting will undoubtedly be the subject of

much future research in the field.

REFERENCES

Anderberg, M., Marion B., and Gray-Hann, P., 2006: Recent Upgrades and Revisions to PVWatts. *Proceedings of the Solar 2006 Conference*, Denver, CO.

ASHRAE, 2005: *Handbook of Fundamentals, SI Edition.* American Society of Heating, Refrigerating and Air-Conditioning Engineers.

Barnett, T. P., J. Ritchie, J. Foat, and G. Stokes, 1998: On the Space and Time Scales of the Surface Solar Radiation Field. *Journal of Climate*, **11,** 88-96.

Bennett, I., 1965: Monthly maps of mean daily insolation for the United States. *Solar Energy*, **9,** 145-158.

Bird, R. E. a. R. L. H., 1981: A Simplified Clear Sky Model for Direct and Diffuse Insolation on Horizontal Surfaces.SERI/TR-642-761.

Bohren, C. F. a. D. R. H., 2010: *Absorption and scattering of light by small particles.* Wiley-Interscience.

Bower, W., M. Behnke, W. Erdman and C. Whitaker, (BEW), 2007: Performanace Test Protocol for Evaluating Inverters Used in Grid-Connected Photovoltaic Systems.

Brock, F. V., K. C. Crawford, R. L. Elliott, G. W. Cuperus, S. J. Stadler, H. L. Johnson, and M. D. Eilts, 1995: The Oklahoma Mesonet: A Technical Overview. *Journal of Atmospheric and Oceanic Technology*, **12,** 5-19.

Brotzge, J. A., 2004: A Two-Year Comparison of the Surface Water and Energy Budgets between Two OASIS Sites and NCEP‚ÄìNCAR Reanalysis Data. *Journal of Hydrometeorology*, **5,** 311-326.

Brotzge, J. A., and S. J. Richardson, 2003: Spatial and Temporal Correlation among Oklahoma Mesonet and OASIS Surface-Layer Measurements. *Journal of Applied Meteorology*, **42,** 5-19.

Bugler, J. W., 1977: The determination of hourly insolation on an inclined plane using a diffuse irradiance model based on hourly measured global horizontal insolation. *Solar Energy*, **19,** 477-491.

Campbell-Scientific, 1996: LI200S Instruction Manual. Campbell Scientific.

Clothiaux, E. E., and Coauthors, 1999: The Atmospheric Radiation Measurement Program Cloud Radars: Operational Modes. *Journal of Atmospheric and Oceanic Technology*, **16,** 819-827.

Collares-Pereira, M., and A. Rabl, 1979: The average distribution of solar radiation-correlations between diffuse and hemispherical and between daily and hourly insolation values. *Solar Energy*, **22,** 155-164.

Crawford, T. M., 1998: *Development of a diagnostic surface energy budget model using Oklahoma Mesonet and ARM data / by Todd Michael Crawford.* 1998.

Crawford, T. M., and H. B. Bluestein, 2000: An Operational, Diagnostic Surface Energy Budget Model. *Journal of Applied Meteorology*, **39,** 1196.

de Miguel, A., J. Bilbao, R. Aguiar, H. Kambezidis, and E. Negro, 2001: Diffuse solar irradiation model evaluation in the North Mediterranean Belt area. *Solar Energy*, **70,** 143-153.

Dissing, D., and G. Wendler, 1998: Solar Radiation Climatology of Alaska. *Theoretical and Applied Climatology*, **61,** 161-175-175.

Duffie, J. A. a. W. A. B., 2006: *Solar Energy Thermal Processes.* Wiley Interscience.

Eckert, P. a. D. K., 1996: Characterizing (Rating) Performance of Large PV Arrays for All Operating Conditions. *25th IEEE PV Specialists Conference*, 1385-1388.

Energy Information Agency 2010: Oklahoma Electricity Profile.

Engerer, D. P. E. S. E., Distribution Planning and Protection, 2010: Personal Communication. FirstEnergy Corp.

Erbs, D. G., S. A. Klein, and J. A. Duffie, 1982: Estimation of the diffuse radiation fraction for hourly, daily and monthly-average global radiation. *Solar Energy*, **28,** 293-302.

Fanney, A. H., P. D. Brian, and W. D. Mark, 2009: Comparison of Predicted to Measured Photovoltaic Module Performance. *Journal of Solar Energy Engineering*, **131,** 021011-021011-021010.

Fanney, A. H. e. a., 2002: Short-Term Characterization of Building Integrated Photovoltaic Modules. *Proc. of Solar Forum*, Reno, NV June 15-19.

Fiebrich, C. A., J. E. Martinez, J. A. Brotzge, and J. B. Basara, 2003: The Oklahoma Mesonet's Skin Temperature Network. *Journal of Atmospheric and Oceanic Technology*, **20,** 1496-1504.

Gao, W., R. L. Coulter, B. M. Lesht, J. Qiu, and M. L. Wesely, 1998: Estimating Clear-Sky Regional Surface Fluxes in the Southern Great Plains Atmospheric Radiation Measurement Site with Ground Measurements and Satellite Observations. *Journal of Applied Meteorology*, **37,** 5-22.

Giacomelli, S. K. a. G., 2002: Solar Radiation Availability for Plant Growth in Arizona Controlled Environment Agriculture Systems. *Controlled Environment Agriculture Center*.

Godfrey, C. M., and D. J. Stensrud, 2010: An Empirical Latent Heat Flux Parameterization for the Noah Land Surface Model. *Journal of Applied Meteorology & Climatology*, **49,** 1696-1713.

Granger, O. E., 1980: Climatology of global solar radiation in California and an interpolation technique based on orthogonal functions. *Solar Energy*, **24,** 153-168.

Group, T. S., 2006: Massachusetts Surprising Candidate for Solar Power Leadership.

Gueymard, C., 1987: An anisotropic solar irradiance model for tilted surfaces and its comparison with selected engineering algorithms. *Solar Energy*, **38,** 367-386.

Gueymard, C. A., 2003: Direct solar transmittance and irradiance predictions with broadband models. Part II: validation with high-quality measurements. *Solar Energy*, **74,** 381-395.

Gueymard, C. A., 2009: Direct and indirect uncertainties in the prediction of tilted irradiance for solar engineering applications. *Solar Energy*, **83,** 432-444.

Guichard, F. o., D. B. Parsons, J. Dudhia, and J. Bresch, 2003: Evaluating Mesoscale Model Predictions of Clouds and Radiation with SGP ARM Data over a Seasonal Timescale. *Monthly Weather Review*, **131,** 926-944.

Hay, J. E., 1979: Calculation of monthly mean solar radiation for horizontal and inclined surfaces. *Solar Energy*, **23,** 301-307.

Hay, J. E. a. M., D.C., 1986: Calculation of Solar Irradiances for Inclined Surfaces: Verification of Models Which Use Hourly and Daily Data. *Report to International Energy Agency*, **SHCP Task IX**.

Henderson, P. W., and R. Pincus, 2009: Multiyear Evaluations of a Cloud Model Using ARM Data. *Journal of the Atmospheric Sciences*, **66,** 2925-2936.

Hottel, H. C. a. B. B. W., 1942: Performance of flat-plate solar-heat collectors. *Transactions of American Society of Mechanical Engineers*, **64**.

Hunt, E. D., J. B. Basara, and C. R. Morgan, 2007: Significant Inversions and Rapid In Situ Cooling at a Well-Sited Oklahoma Mesonet Station. *Journal of Applied Meteorology & Climatology*, **46,** 353-367.

International Energy Agency, I., 2010a: *World Energy Outlook 2010.*

International Energy Agency, I., 2010b: Trends in Photovoltaic Applications: Survey report of selected IEA countries between 1992 and 2009IEA-PVPS T1-19:2010.

Iqbal, M., 1980: Prediction of hourly diffuse solar radiation from measured hourly global radiation on a horizontal surface. *Solar Energy*, **24,** 491-503.

Isaaks, E. H. and S., R. Mohan, 1990: An Introduction to Applied Geostatistics. Oxford University Press.

Kambezidis, H. D., B. E. Psiloglou, and C. Gueymard, 1994: Measurements and models for total solar irradiance on inclined surface in Athens, Greece. *Solar Energy*, **53,** 177-185.

Kasten, F., and A. T. Young, 1989: Revised optical air mass tables and approximation formula. *Appl. Opt.*, **28,** 4735-4738.

King, D. L., W. E. Boyson, and B. R. Hansen, 1997: Improved accuracy for low-cost solar irradiance sensorsSAND--97-3175C; CONF-980735--; Other: ON: DE98002961; BR: EB2202000; TRN: TRN: AHC29814%%106, Medium: ED; Size: 4 p. pp.

King, D. L., W. E. Boyson, and J. A. Kratochvil, 2002: Analysis of factors influencing the annual energy production of photovoltaic systems. *Photovoltaic Specialists Conference, 2002. Conference Record of the Twenty-Ninth IEEE*, 1356-1361.

King, D. L., J. Kratochvil and W. Boyson, 1997: Measuring Solar Spectral and Angle-of-Incidence Effects on PV Modules and Solar Irradiance Sensors. *26th IEEE PV Specialists Conference*, 1113-1116.

King, D. L., Sigifredo Gonzalez, Gary M. Galbraith, and William E. Boyson, 2007: Performance Model for Grid-Connected Photovoltaic Inverters. *Sandia Report*, **SAND2007-5036**.

King, D. L., W.E. Boyson, J.A. Kratochvil, 2004: Photovoltaic Array Performance Model.

Klucher, T. M., 1979: Evaluation of models to predict insolation on tilted surfaces. *Solar Energy*, **23,** 111-114.

Kollias, P., and Coauthors, 2007: The Atmospheric Radiation Measurement Program Cloud Profiling Radars: Second-Generation Sampling Strategies, Processing, and Cloud Data Products. *Journal of Atmospheric and Oceanic Technology*, **24,** 1199-1214.

Krivova, N. A., S. K. Solanki, and Y. C. Unruh, 2011: Towards a long-term record of solar total and spectral irradiance. *Journal of Atmospheric and Solar-Terrestrial Physics*, **73,** 223-234.

Kroposki, B., M. W., K. D., B. W., and K. J., 2000: Comparison of Module Performance Characterization Methods. *28th IEEE PV Specialists Conference,* 1407-1411.

Laue, E. G., 1970: The measurement of solar spectral irradiance at different terrestrial elevations. *Solar Energy*, **13,** 43-50, IN41-IN44, 51-57.

Liu, B. Y. H., and R. C. Jordan, 1963: The long-term average performance of flat-plate solar-energy collectors: With design data for the U.S., its outlying possessions and Canada. *Solar Energy*, **7,** 53-74.

Loutzenhiser, P. G., H. Manz, C. Felsmann, P. A. Strachan, T. Frank, and G. M. Maxwell, 2007: Empirical validation of models to compute solar irradiance on inclined surfaces for building energy simulation. *Solar Energy*, **81,** 254-267.

Marion, B., 2010: Overview of the PV Module in PVWattsPR-520-49607.

Maui-Solar-Energy-Software-Corporation, 2004: v5.0.

Maxwell, E., R. George, and S. Wilcox, 1998: A Climatological Solar Radiation Model. *Proc. of the 1998 Annual Conference, American Solar Energy Society*, Albuquerque, NM.

Maxwell, E. L., 1987: Quasi-physical model for converting hourly global horizontal to direct normal insolation. *Solar '87 Conference*, Portland, OR, American Solar Energy Society, pp. 35-46.

McManus, G. D., 1999: *A cloud and global solar radiation climatology for the U. S. Great Plains 1952-1991.* 1999.

McPherson, R. A., D. J. Stensrud, and K. C. Crawford, 2004: The Impact of Oklahoma's Winter Wheat Belt on the Mesoscale Environment. *Monthly Weather Review*, **132,** 405-421.

McPherson, R. A., and Fiebrich, C.A. Crawford, K. C., James K. R., Grimsley, D. L., Martinez, J. E., Basara, J. B. Illston, B. G., Morris, D. A., Kloesel, K. A., Melvin, A. D., Shrivastava, H., Wolfinbarger, J., Bostic, J. P., Demko, D. B., Elliott, R. L., Stadler, S. J., Carlson, J. D., Sutherland, A. J., 2007: Statewide Monitoring of the Mesoscale Environment: A Technical Update on the Oklahoma Mesonet. *Journal of Atmospheric and Oceanic Technology*, **24,** 301-321.

Muneer, T., 2004: *Solar Radiation and Daylight Models.* Butterworth-Heinemann.

Myers, D. R. a. G. C. A., 2008: *Validation and Ranking Methodologies for Solar Radiation Models.* Springer.

NREL, 2007: National Solar Radiation Database 1991-2005 Update: User's ManualNREL/TP-581-41364.

NREL: NREL Solar Maps. 2011 [Available online at http://www.nrel.gov/gis/solar.html.]

OG&E Energy Corp: Oklahoma Rate Tariffs. [Available online at http://oge.com/residential-customers/billing-and-payment/Pages/RateInfo.aspx.]

Orgill, J. F., and K. G. T. Hollands, 1977: Correlation equation for hourly diffuse radiation on a horizontal surface. *Solar Energy*, **19,** 357-359.

Perez, R., R. Seals, P. Ineichen, R. Stewart, and D. Menicucci, 1987: A new simplified version of the perez diffuse irradiance model for tilted surfaces. *Solar Energy*, **39,** 221-231.

Perez, R., P. Ineichen, R. Seals, J. Michalsky, and R. Stewart, 1990: Modeling daylight availability and irradiance components from direct and global irradiance. *Solar Energy*, **44,** 271-289.

Randall, C. M. a. M. E. W. J., 1977: Hourly Insolation Models and Meteorological Data Bases Including Improved Direct Insolation EstimatesATR-78(7592)-1.

Reindl, D. T., W. A. Beckman, and J. A. Duffie, 1990: Evaluation of hourly tilted surface radiation models. *Solar Energy*, **45,** 9-17.

Reindl, D. T., W. A. Beckman, and J. A. Duffie, 1990: Diffuse fraction correlations. *Solar Energy*, **45,** 1-7.

RNCOS, 2011: US Photovoltaic Market Analysis.

Rojo, A. G., and P. R. Berman, 2010: Rayleigh scattering revisited: From gases to crystals. *Am. J. Phys.,* **78,** 94-101.

Rosenberg, N. J., 1964: Solar Energy and Sunshine in Nebraska. *Neb. Agr. Exp. Sta. Bull*, **213,** 28.

Sanyo-Energy-Corp, 2005: HIT Photovoltaic Module - HIP-200BA3.

Sharp-Electronics-Corporation, 2007: Sharp ND-216U1F Multi-Purpose Module.

Sherwood, L., 2010: U.S. Solar Marke Trends 2009 Executive Summary.

Skartveit, A., and J. A. Olseth, 1987: A model for the diffuse fraction of hourly global radiation. *Solar Energy*, **38,** 271-274.

Snead, M., and S. Barta, 2008: The Economic Impact of Oil and Gas Production and Drilling on the Oklahoma Economy.

Spencer, J. W., 1971: Fourier Series Representation of the Position of the Sun. *Search*, **2,** 1.

Sridhar, V., and R. L. Elliott, 2002: On the development of a simple downwelling longwave radiation scheme. *Agricultural and Forest Meteorology*, **112,** 237-243.

Stokes, G. M., and S. E. Schwartz, 1994: The Atmospheric Radiation Measurement (ARM) Program: Programmatic Background and Design of the Cloud and Radiation Test Bed. *Bulletin of the American Meteorological Society*, **75,** 1201-1221.

Temps, R. C., and K. L. Coulson, 1977: Solar radiation incident upon slopes of different orientations. *Solar Energy*, **19,** 179-184.

Topline Strategy Group 2006: Massachusetts Surprising Candidate for Solar Power Leadership. RNCOS

Torres, J. L., M. De Blas, A. García, and A. de Francisco, 2010: Comparative study of various models in estimating hourly diffuse solar irradiance. *Renewable Energy*, **35,** 1325-1332.

Vliet, G. C., 2004: Texas Solar Radiation Database (TSRDB). *Journal of Solar Energy Engineering*, **126,** 575-580.

Whitaker, C. T., T. Townsend, J. Newmiller, D. King, W. Boyson, J. Kratochvil, D. Collier and D. Osborn, 1997: Application and Validation of

a New PV Performance Characterization Method. *26th IEEE PV Specialists Conference*, 1253-1256.

Woolf, H. M., 1968: On the Computation of Solar Evaluation Angles and the Determination of Sunrise and Sunset TimesNASA TM-X -164.

Wu, X., X.-Z. Liang, and S. Park, 2007: Cloud-Resolving Model Simulations over the ARM SGP. *Monthly Weather Review*, **135,** 2841-2853.

Zhou, B., and Q. Xu, 1999: Computing Surface Fluxes from Mesonet Data. *Journal of Applied Meteorology*, **38,** 1370-1383.

APPENDIX A

TABLES

Table 4.3-1. Mesonet stations chosen for monthly analyses. Stations were chosen to represent different climatological regions as well as the largest amount of potential end users. (2006 US Census Data)

Mesonet Site	ID	Region	Nearest City	Population
Bixby	BIXB	Northeast	Tulsa	382,782
Boise City	BOIS	Panhandle	Guymon	10,625
Medicine Park	MEDI	Southwest	Lawton	87,540
McAlester	MCAL	Southeast	McAlester	18,333
Norman	NRMN	Central	Norman	102,827
Spencer	SPEN	Central	Oklahoma City	537,738
Woodward	WOOD	Northwest	Woodward	12,033

Table 5.2-1. Total cost of installation for Sharp and Sanyo 2kW rooftop systems.

Estimate courtesy of Sunrise Alternative Energy Corporation.

Cost Category	Cost Sharp 2.24 kW Array	Cost Sanyo 2.15 kW Array
10 Panels	$7,250	$8,350
Inverter System	$2,750	$2,800
Mounting Racks	$1,800	$1,800
Misc. Components	$500	$500
Installation	$2,000	$2,000
Total before Tax Credit	**$14,300**	**$15,400**
30% Tax Credit	$4,290	$4,620
Total Cost	**$10,010**	**$10,780**

Table 5.2-2. Mean yearly power production and estimated time needed to capitalize on initial investment costs for the Sharp and Sanyo array systems.

Station	Sharp Mean Power Output (kWh)	Years to Offset Cost	Sanyo Mean Power Output (kWh)	Years to Offset Cost
BIXB	3324	30	3132	34
BOIS	4064	24	3828	28
MCAL	3218	31	3039	35
MEDI	3584	27	3378	31
NRMN	3645	27	3266	33
SPEN	3438	29	3245	33
WOOD	3718	26	3540	30
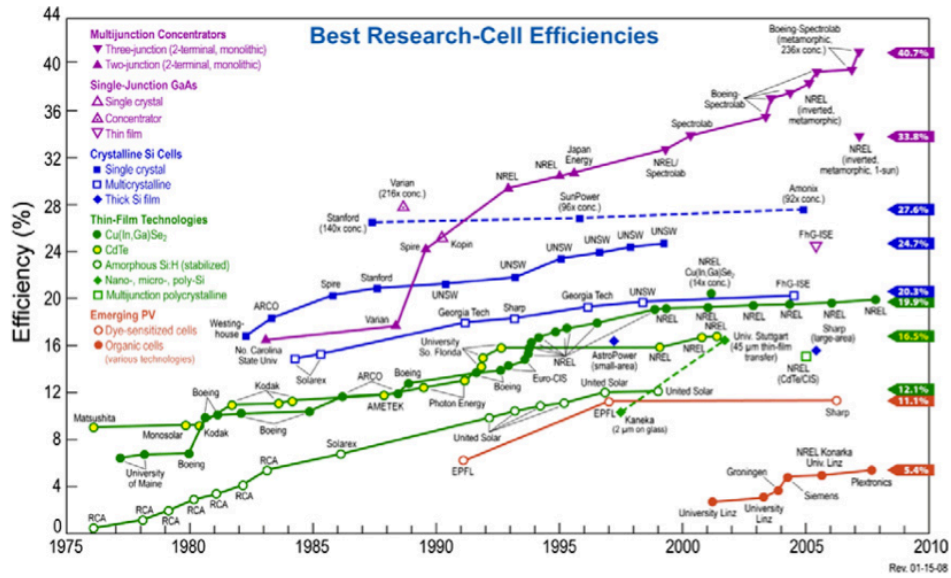
Figure 1.1.1-1. Time series of the advancements in solar cell

efficiencies by cell type (Image adapted from Razykov 2011).
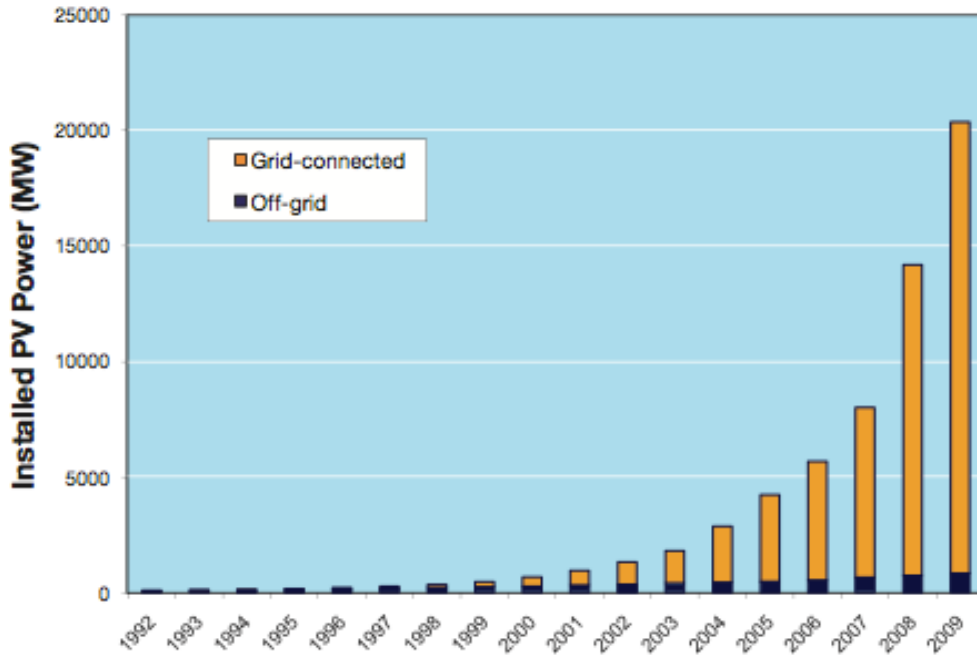
Figure 1.1.1-2. – Installed PV capacity in IEA participating countries

(Image adapted from International Energy Agency 2010a).
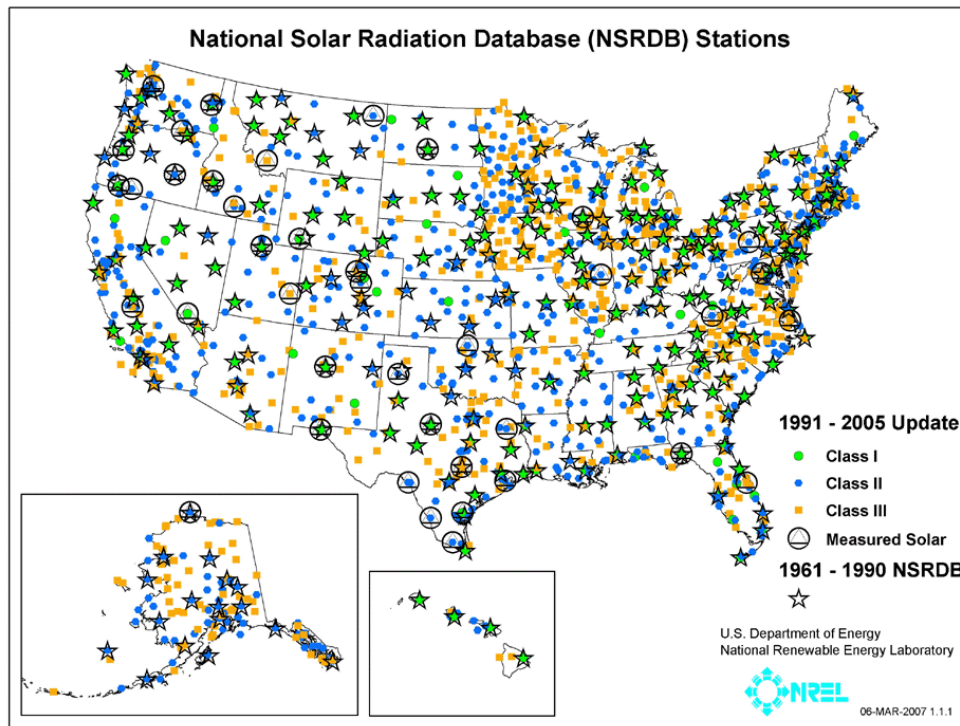
Figure 1.1.3-1. Locations of solar radiation observations included in the

National Solar Radiation Database and subsequent NREL national

analyses. Image courtesy of NREL.
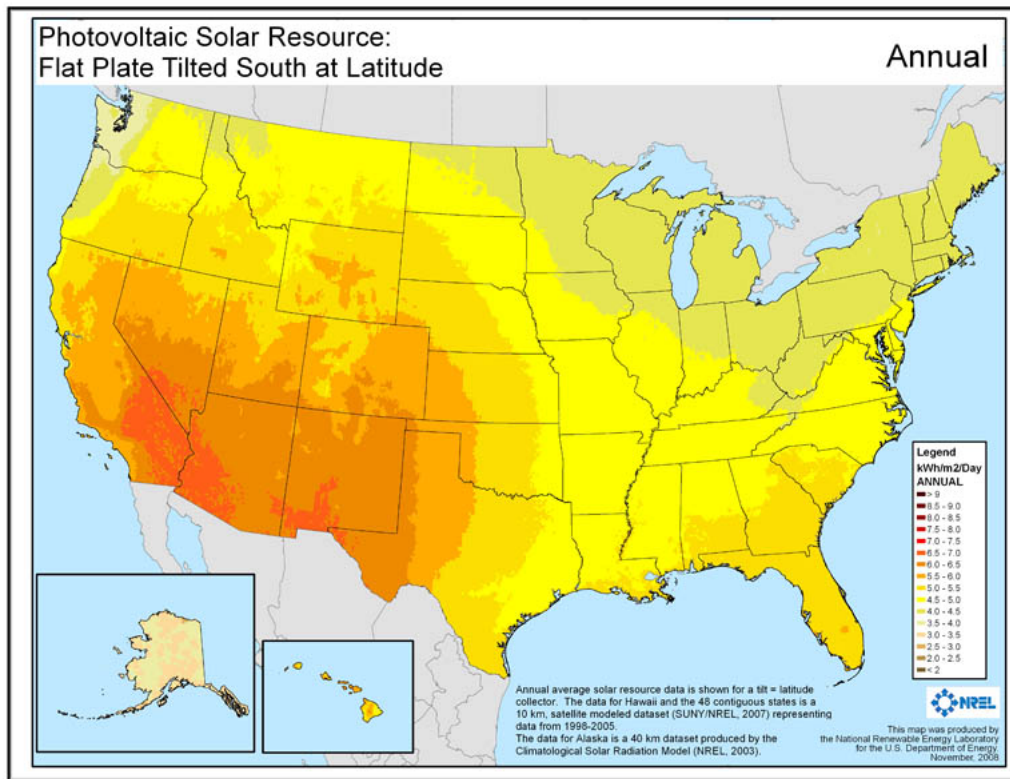
Figure 1.1.3-2. NREL map of annual mean solar radiation available to a south-facing surface at latitude tilt. Image courtesy of NREL.
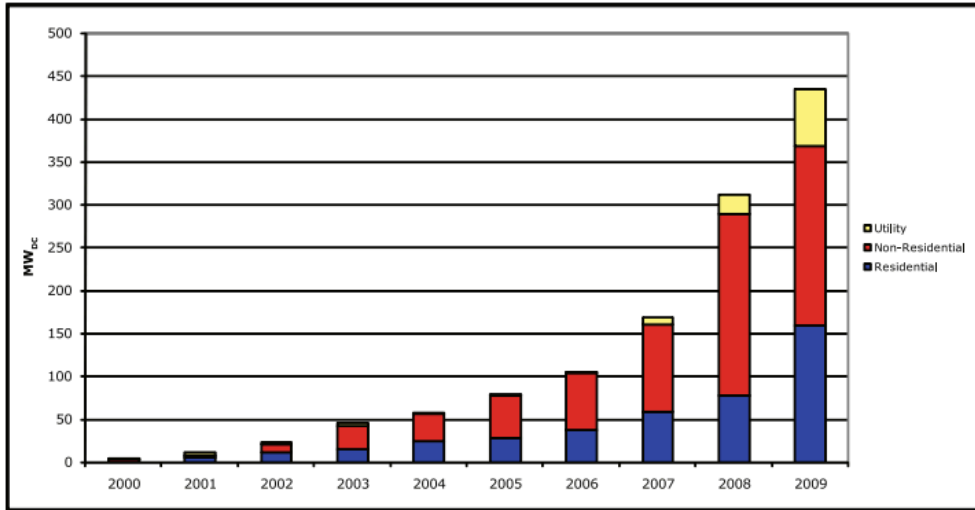
Figure 1.2-1. Installed PV capacity in the United States by location of

installation. Image courtesy of Sherwood 2010.
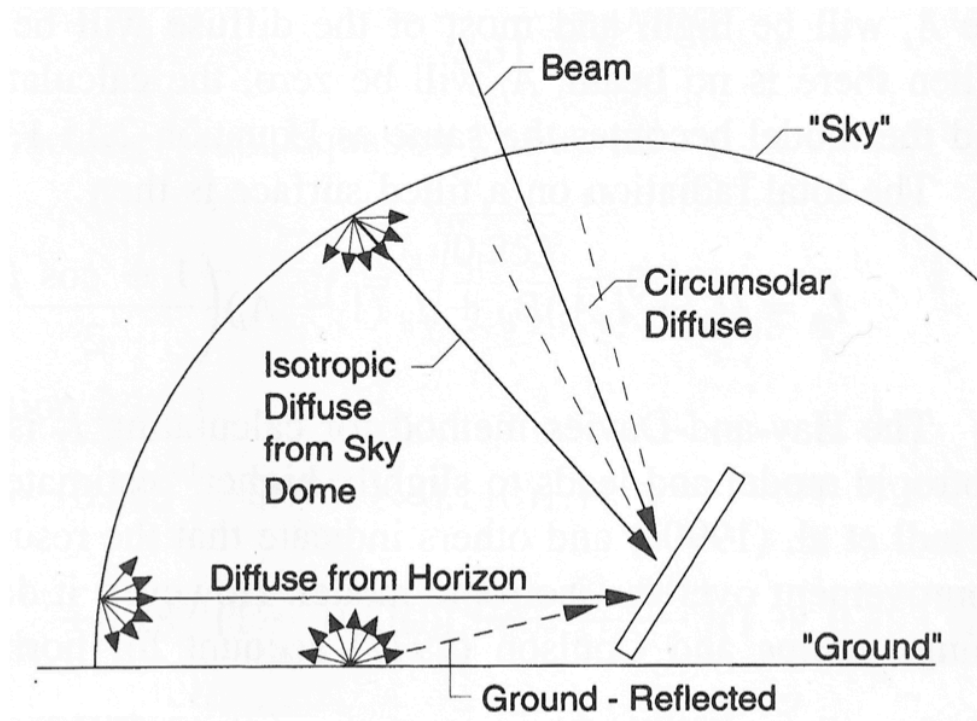
Figure 2.2.4-1. Three sources of diffuse radiation contribute to the E_d component of radiation at a tilted surface: Isotropic, Circumsolar and Horizon Brightening radiation. Figure adapted from Duffie and Beckman 2006 Figure 2.16.1.

Figure 4.1.3-1. Semivariogram for Sharp 2kW array annual mean

production. Points represent the sample variogram, the line is the

exponential modeled fit (nugget = 0.0, sill = 135.0, range = 60.0 km).
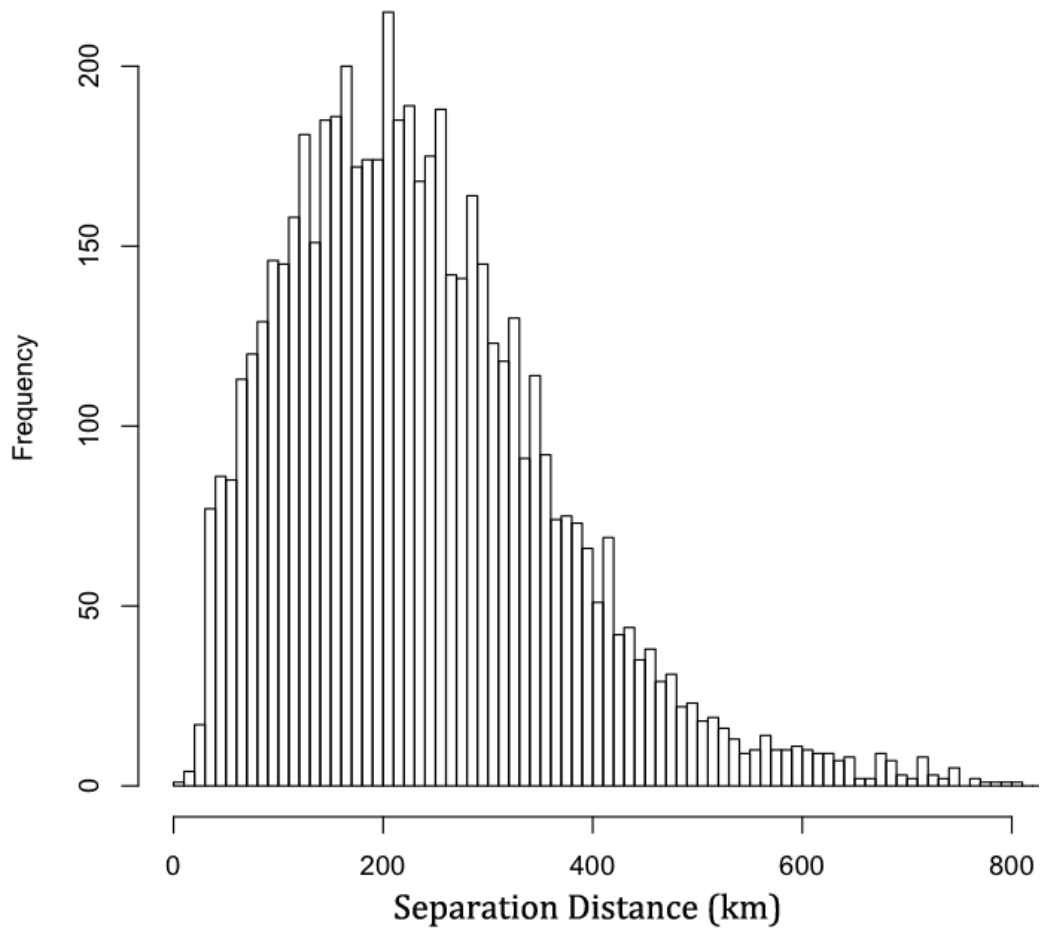
Figure 4.1.3-2. Histogram of station separation distances for the 108

Mesonet stations.

Semivariogram: with Trend Mean Power Production for Sharp 2kW Array
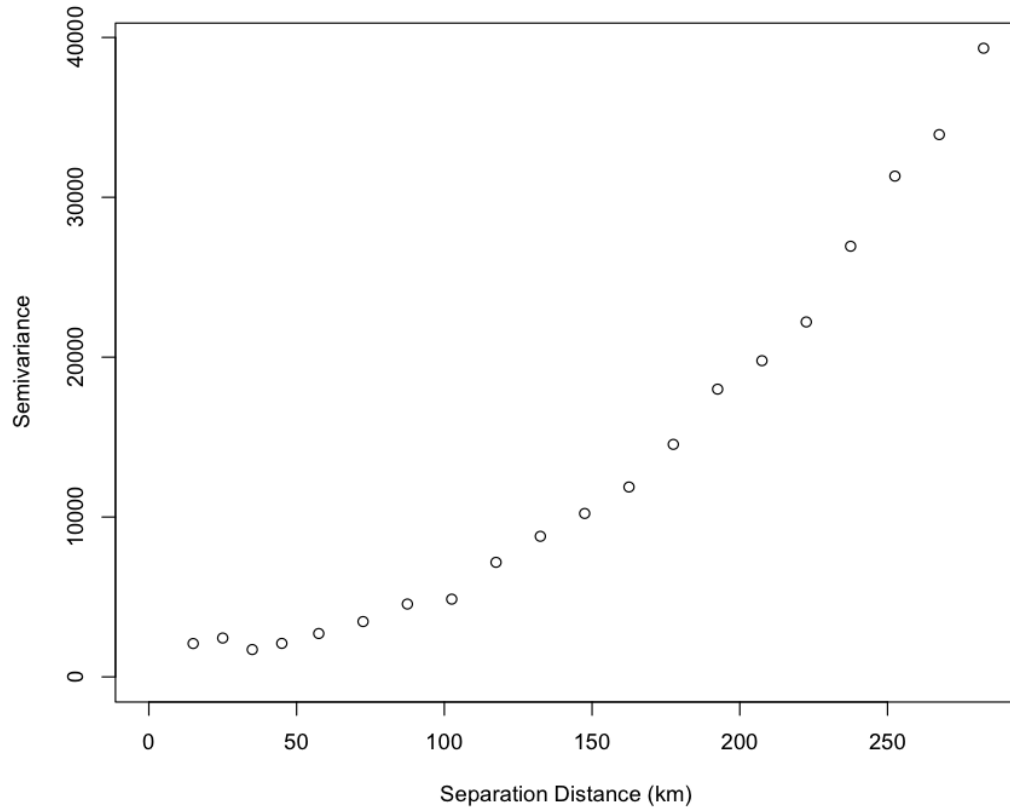
Figure 4.1.3-3. Semivariogram for Sharp 2kW array annual mean

production with a strong westward oriented trend.
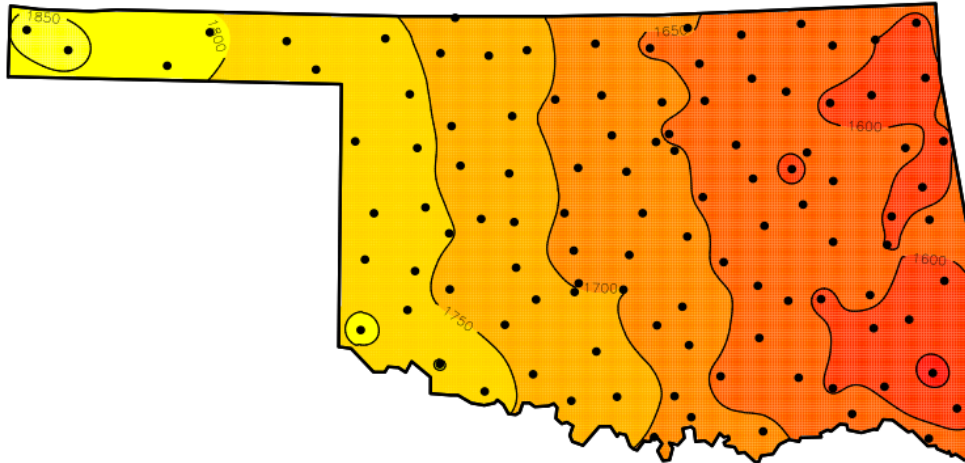
Figure 4.2.1-1. Mean GHI expressed (kWh/m^2).
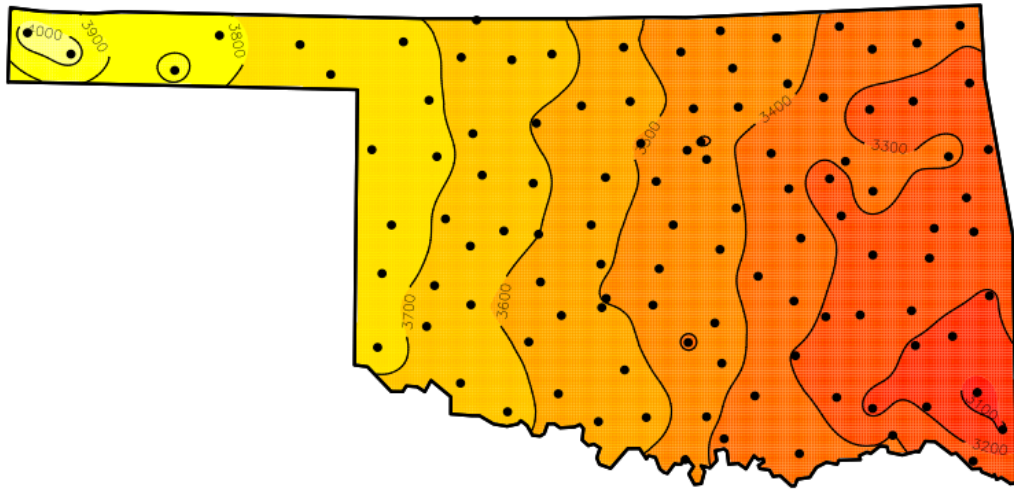
Figure 4.2.2-1. Sharp 2kW array mean annual power production (kWh).
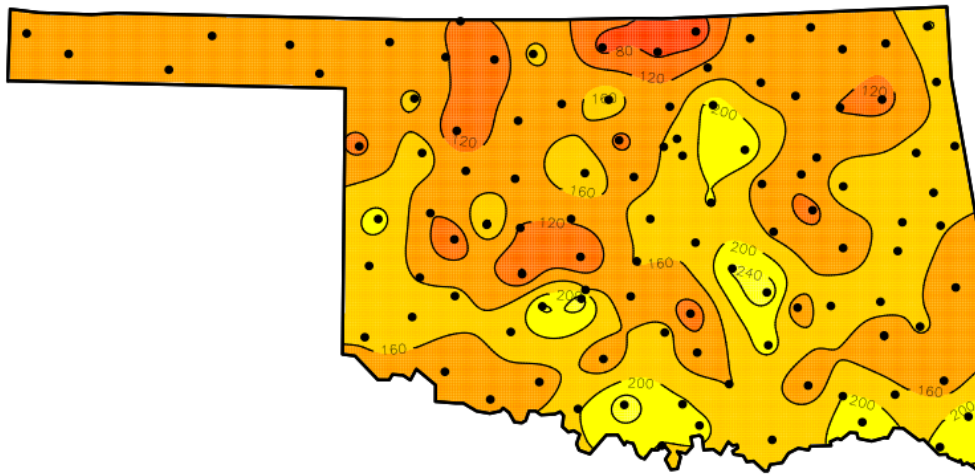
Figure 4.2.2-2. Interquartile ranges for annual mean Sharp 2kW power production (kWh).
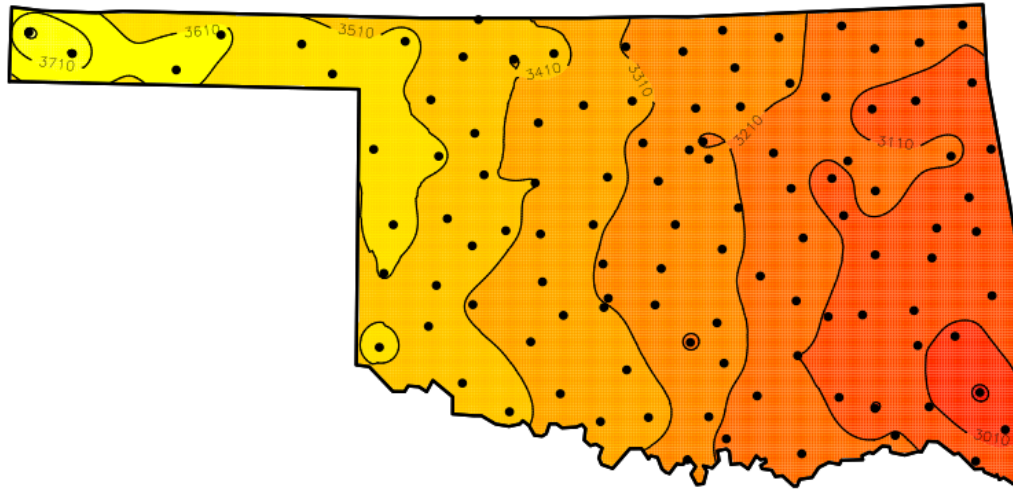
Figure 4.2.3-1. Sanyo 2kW array mean annual power production (kWh).
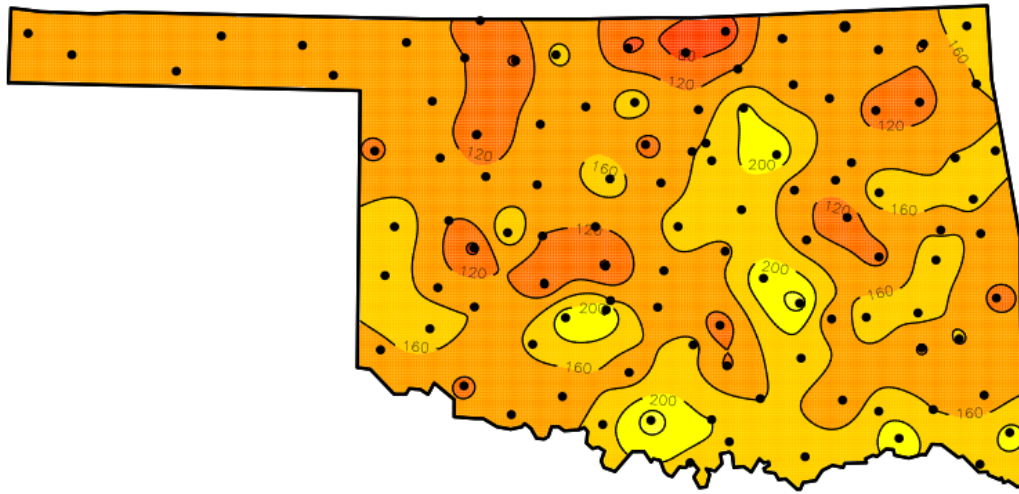
Figure 4.2.3-2. Interquartile ranges for annual mean Sanyo 2kW power production (kWh).
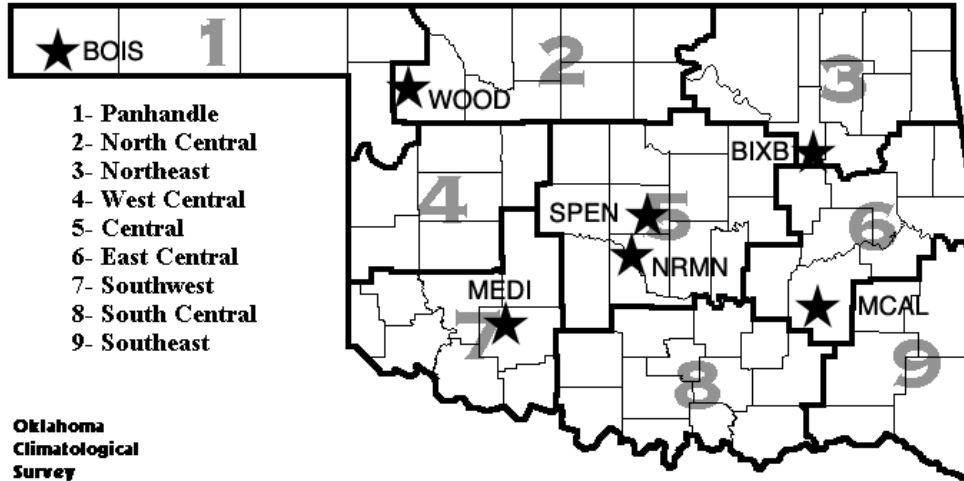
Figure 4.3-1. Mesonet sites chosen for monthly analysis, as listed in

Table 4.3-1 are identified by the black stars and located in 6 of the 9

Oklahoma Climate Divisions. (Climate Divison Map courtesy of OCS)
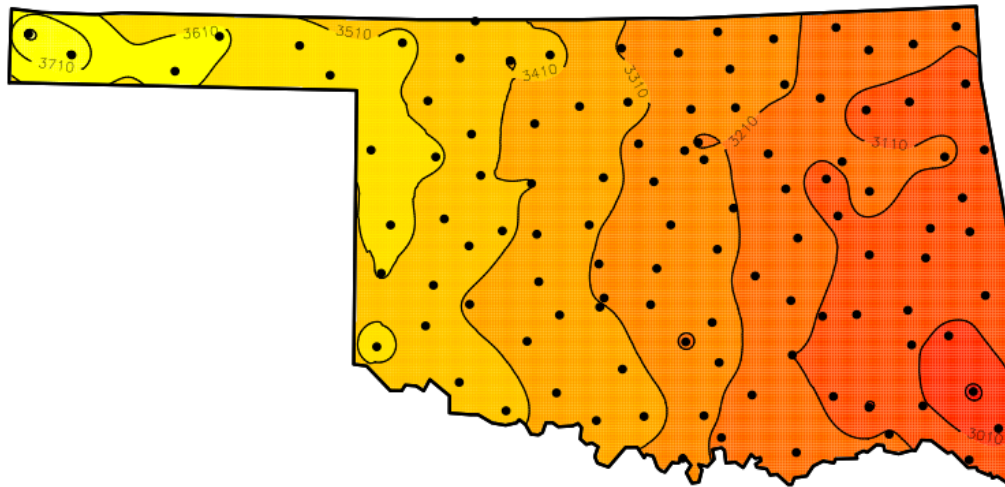
Figure 4.3.1-1. Winter (DJF) mean GHI (kWh/m^2).
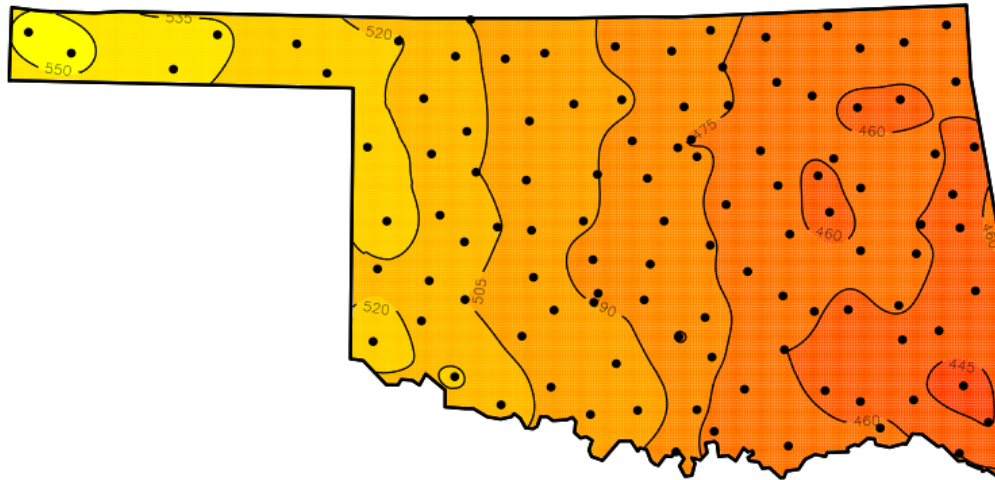
Figure 4.3.1-2. Spring (MAM) mean GHI (kWh/m^2).
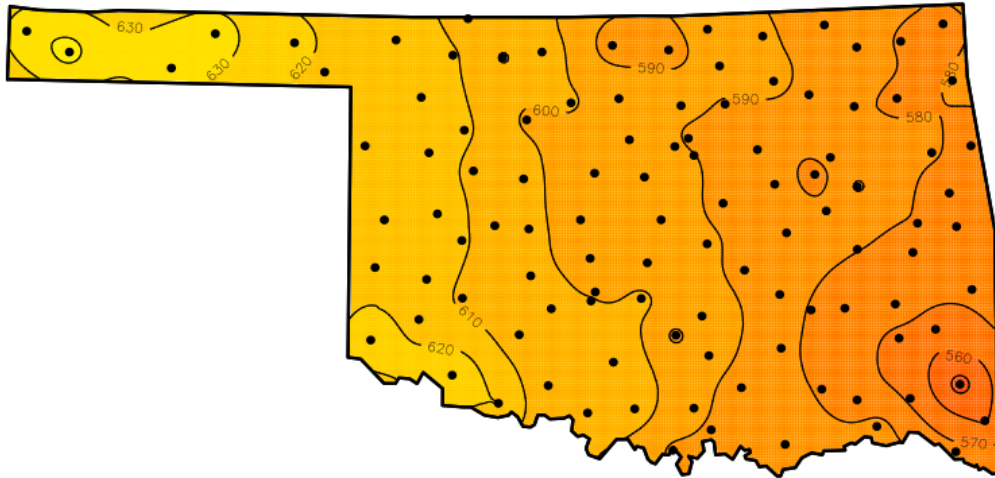
Figure 4.3.1-3. Summer (JJA) mean GHI in (kWh/m^2).
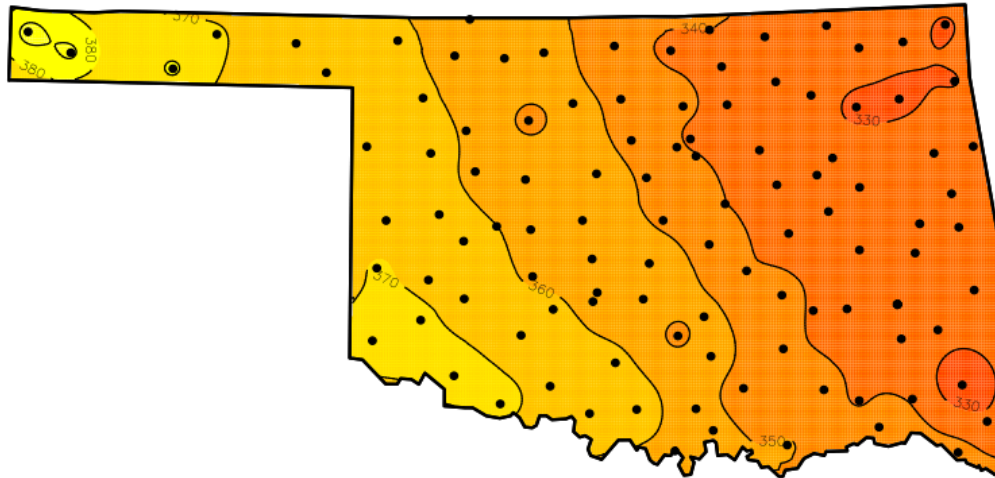
Figure 4.3.1-4. Fall (SON) average GHI (kWh/m^2).
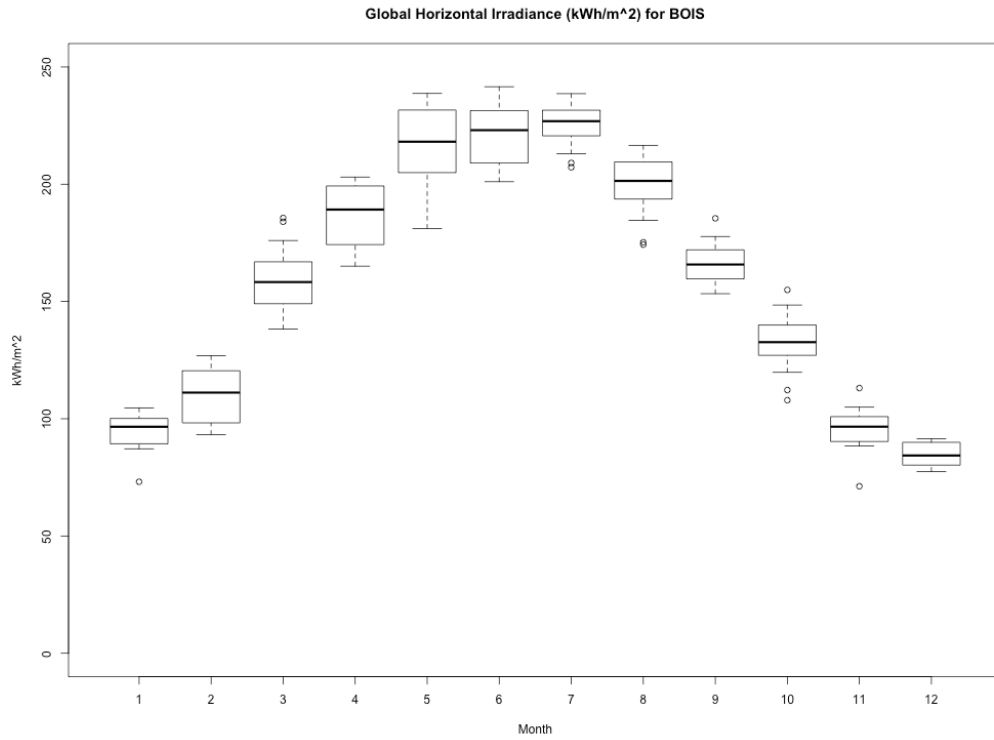
Figure 4.3.1-5. Monthly GHI at BOIS station (kWh/m^2).
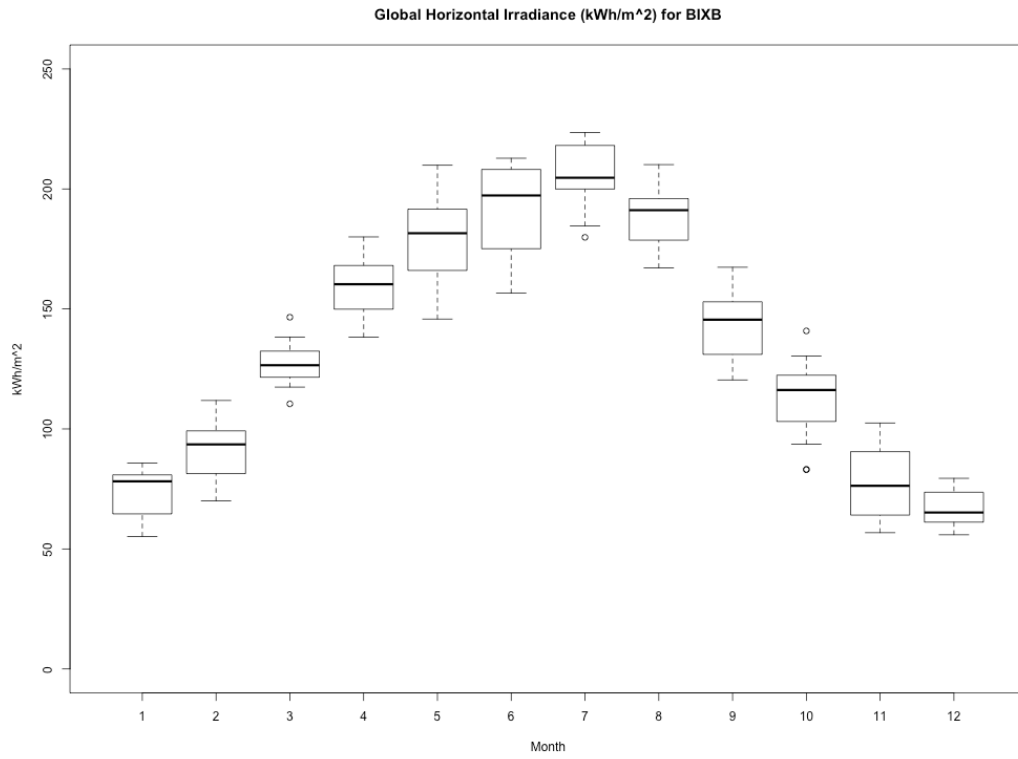
Figure 4.3.1-6. Monthly GHI for BIXB station (kWh/m^2).
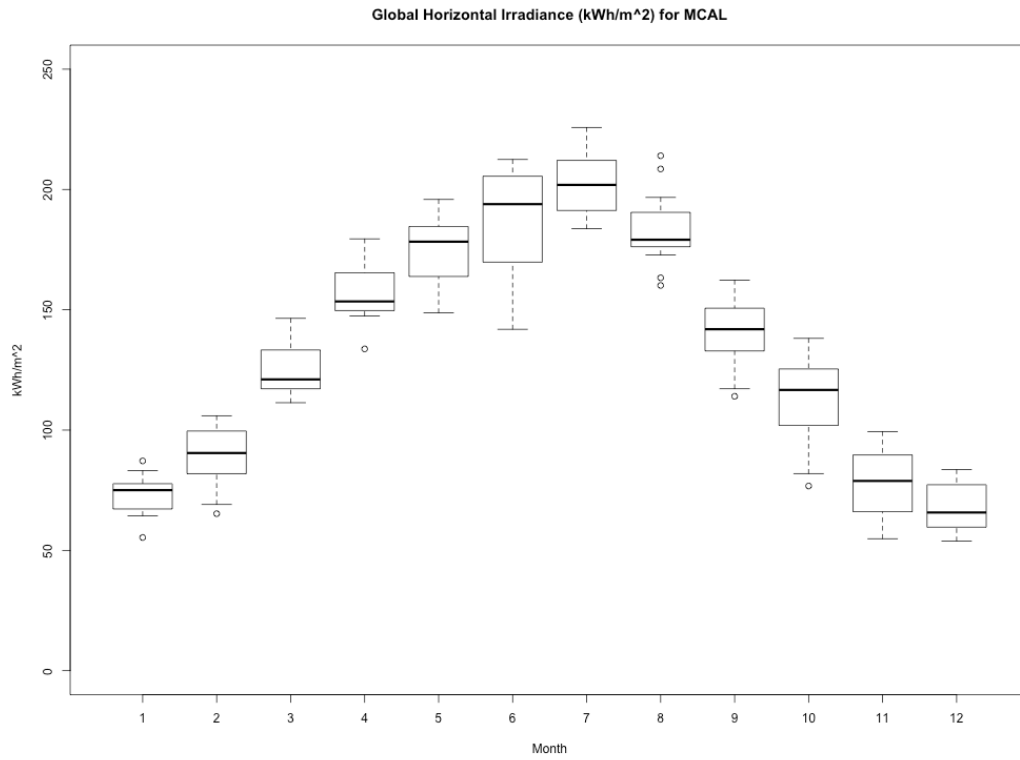
Figure 4.3.1-7. Monthly GHI for MCAL station (kWh/m^2).

138
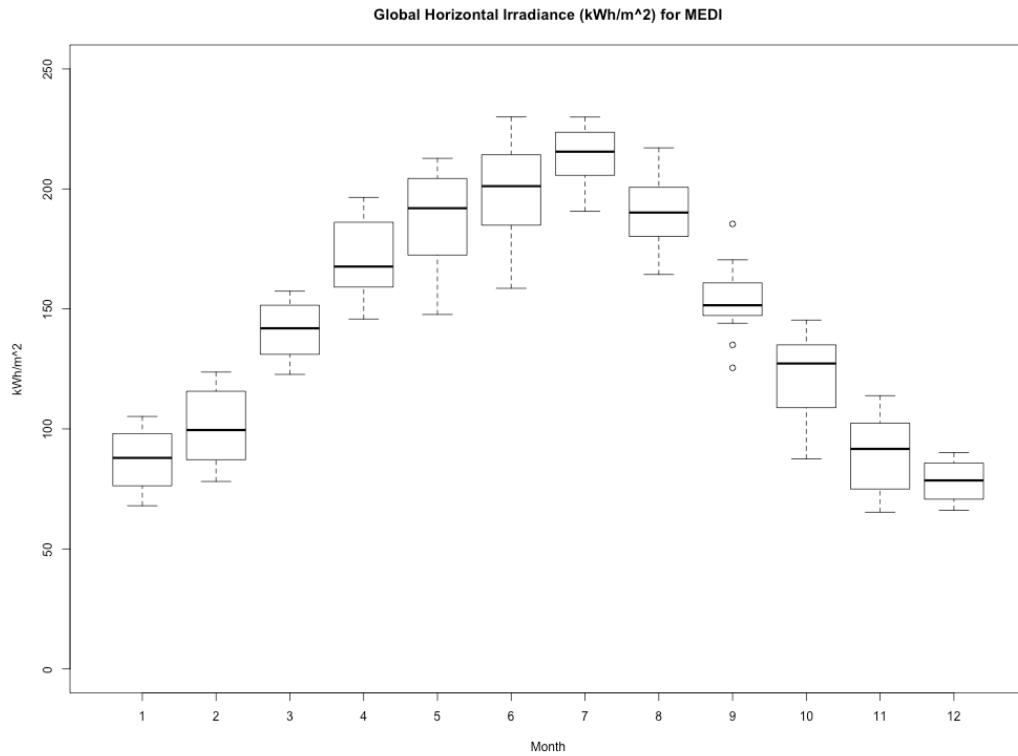
Figure 4.3.1-8. Monthly GHI for MEDI station (kWh/m^2).
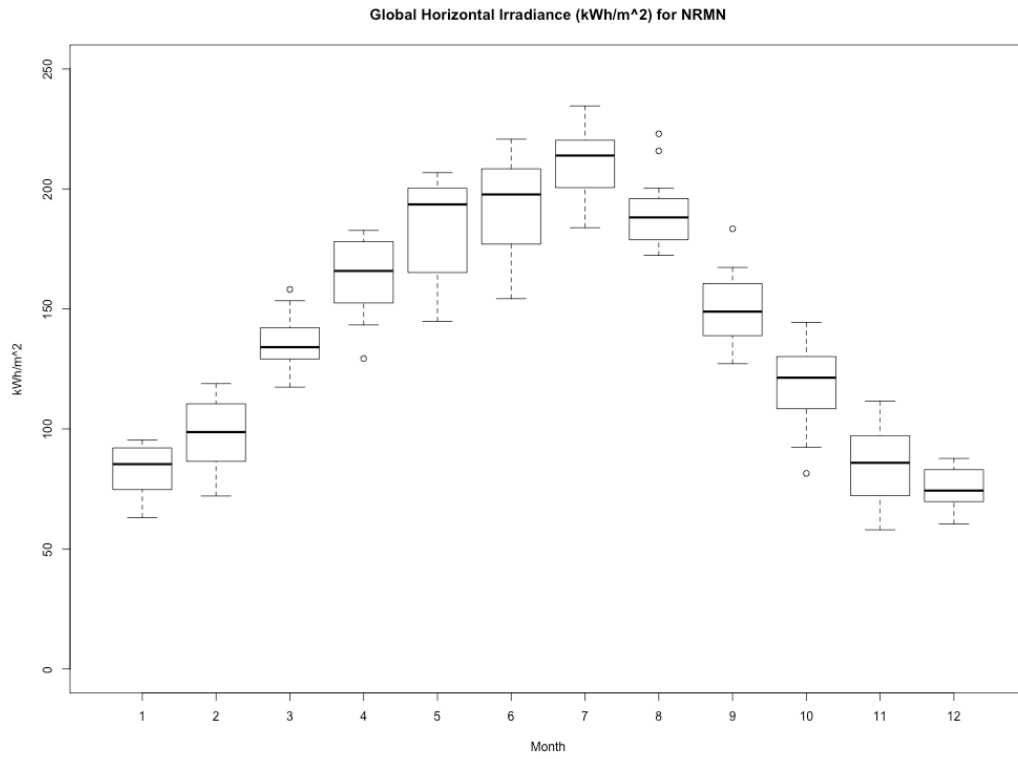
Figure 4.3.1-9. Monthly GHI for NRMN station (kWh/m^2).
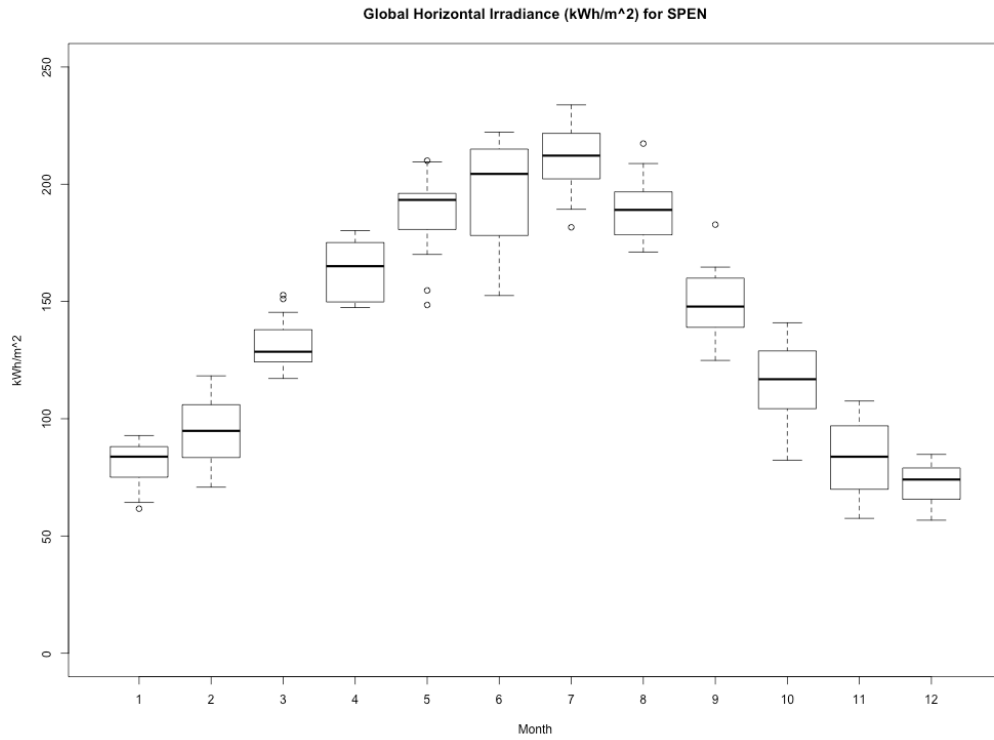
Figure 4.3.1-10. Monthly GHI for SPEN station (kWh/m^2).

141
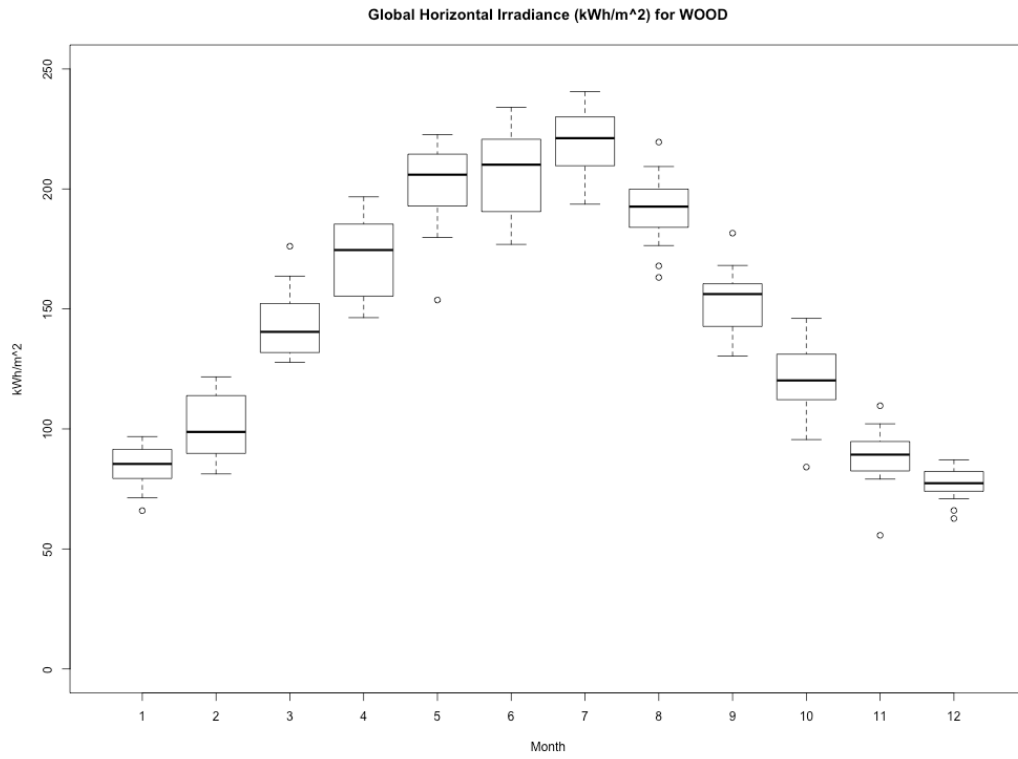
Figure 4.3.1-11. Monthly GHI for WOOD station (kWh/m^2).
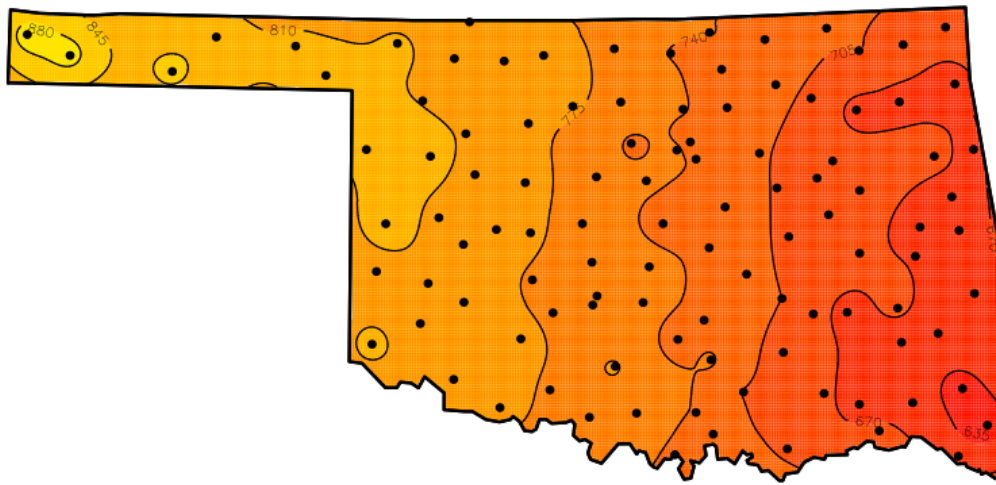
Figure 4.3.2-1. Winter (DJF) Sharp 2kW mean power production (kWh).
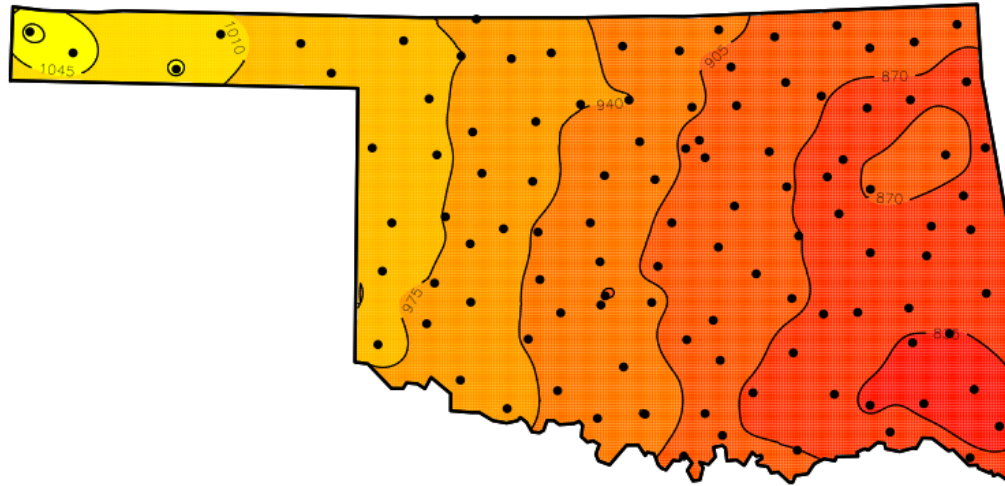
Figure 4.3.2-2. Spring (MAM) Sharp 2kW mean power production

(kWh).
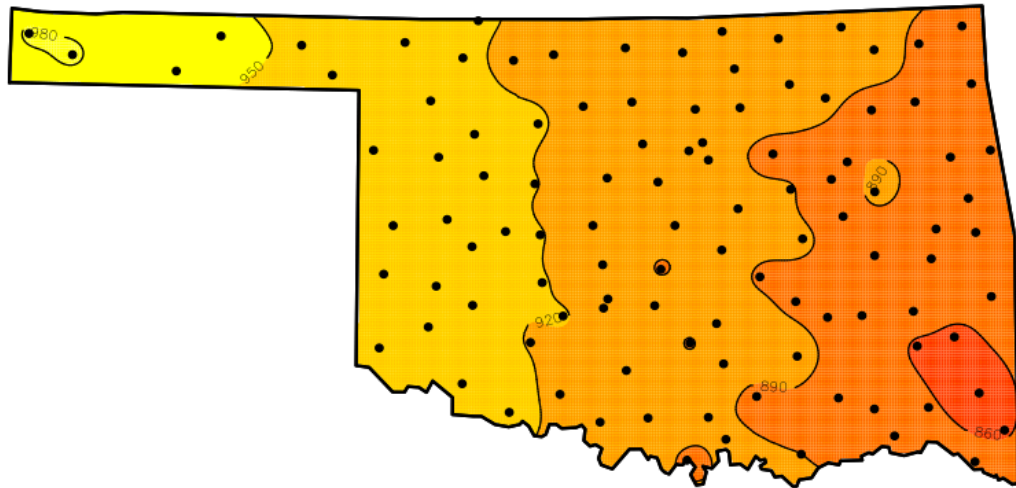
Figure 4.3.2-3. Summer (JJA) Sharp 2kW mean power production (kWh).
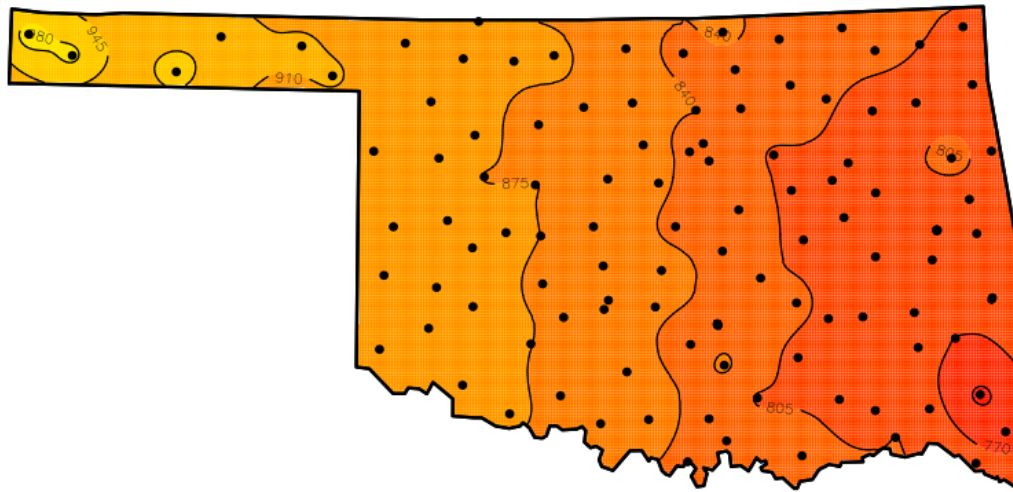
Figure 4.3.2-4. Fall (SON) Sharp 2kW mean power production (kWh).
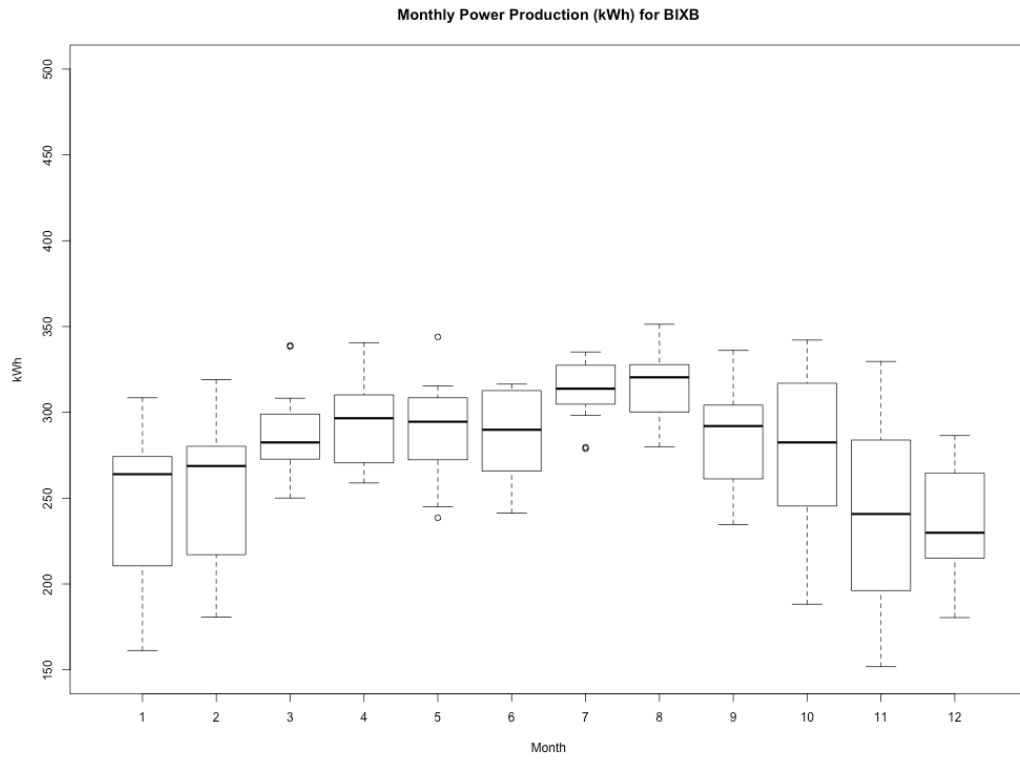
Figure 4.3.2-5. Sharp 2kW monthly power production for BIXB station (kWh).
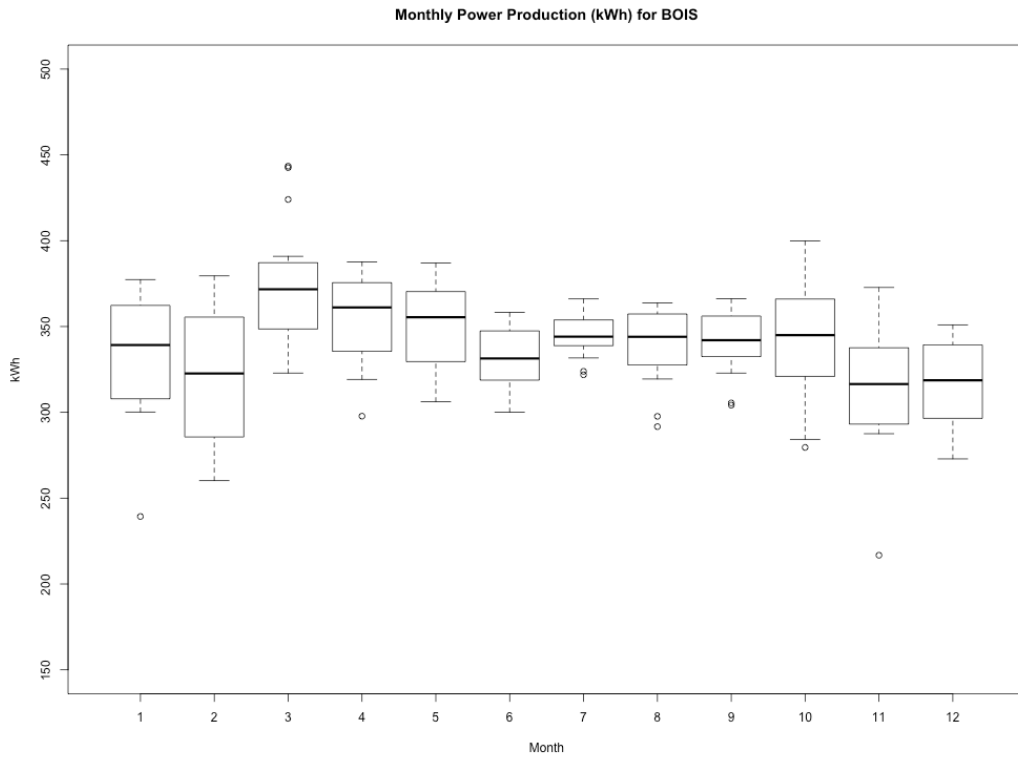
Figure 4.3.2-6. Sharp 2kW monthly power production for BOIS station (kWh).

148
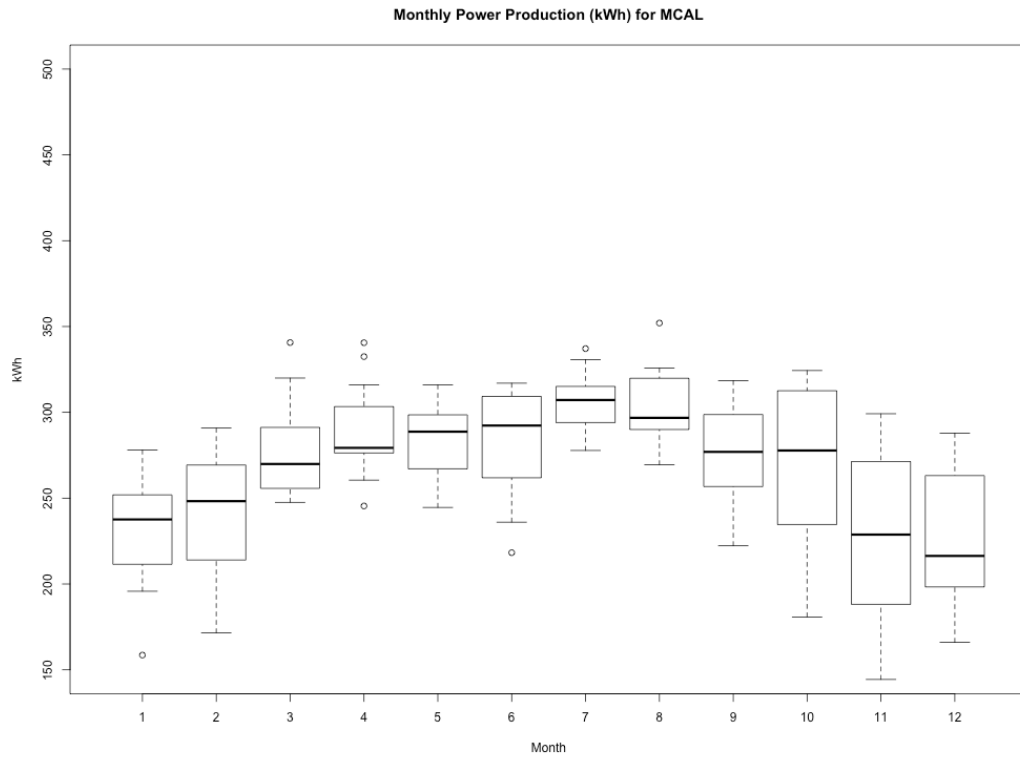
Figure 4.3.2-7. Sharp 2kW monthly power production for MCAL station (kWh).
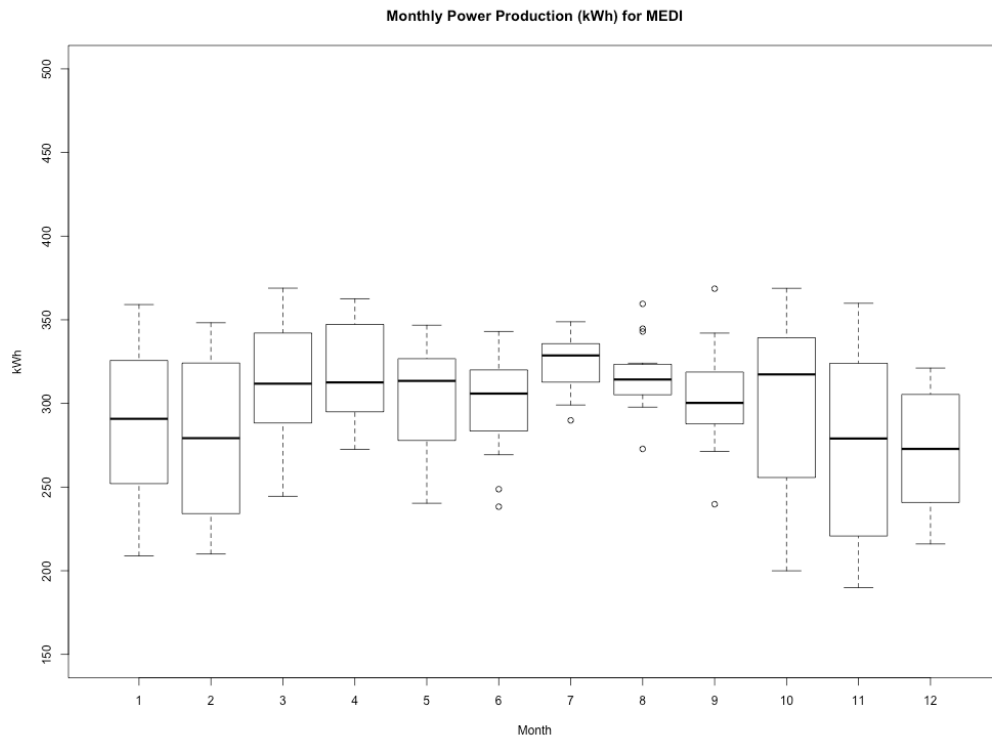
Figure 4.3.2-8. Sharp 2kW monthly power production for MEDI station
(kWh).
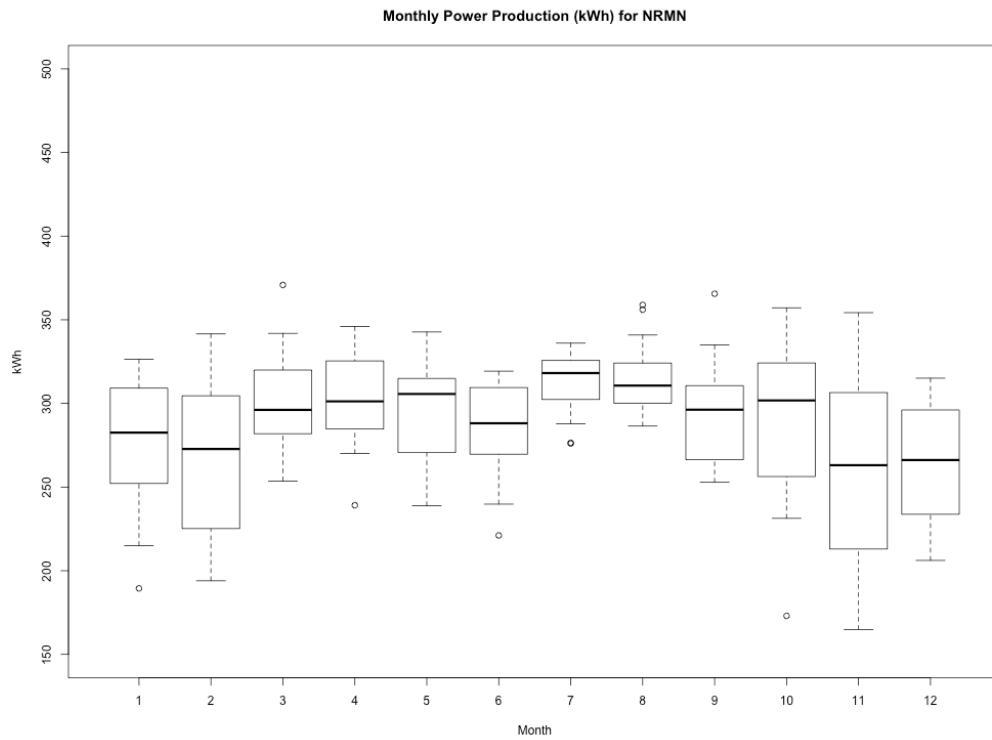
Figure 4.3.2-9. Sharp 2kW monthly power production for NRMN station (kWh).
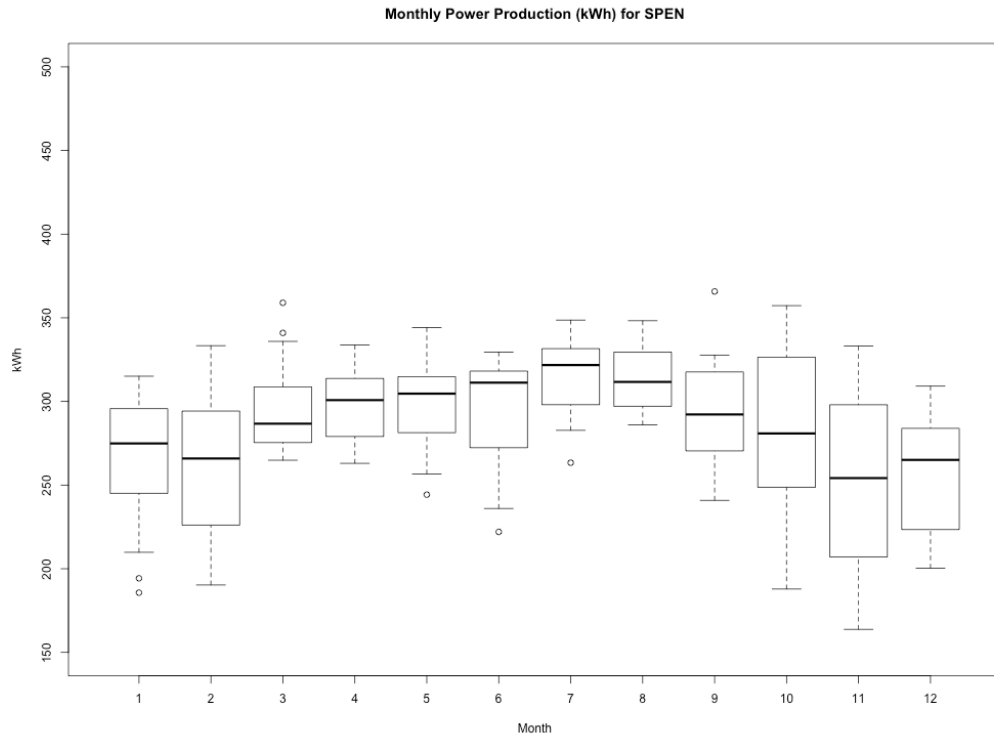
Figure 4.3.2-10. Sharp 2kW monthly power production for SPEN station

(kWh).
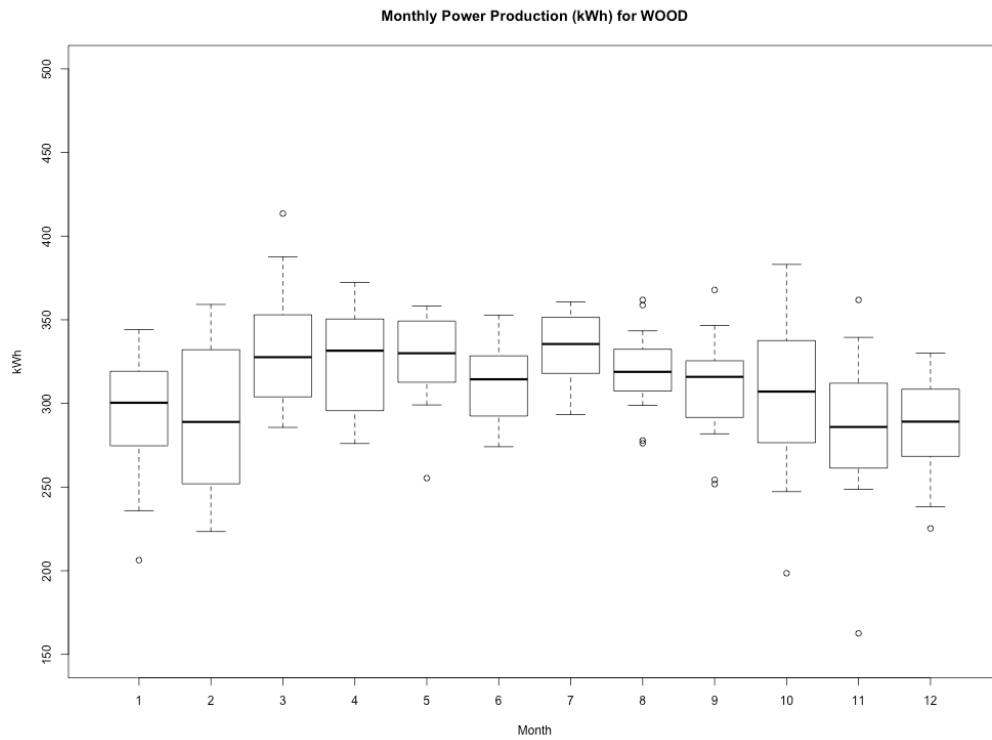
Figure 4.3.2-11. Sharp 2kW monthly power production for WOOD

station (kWh).
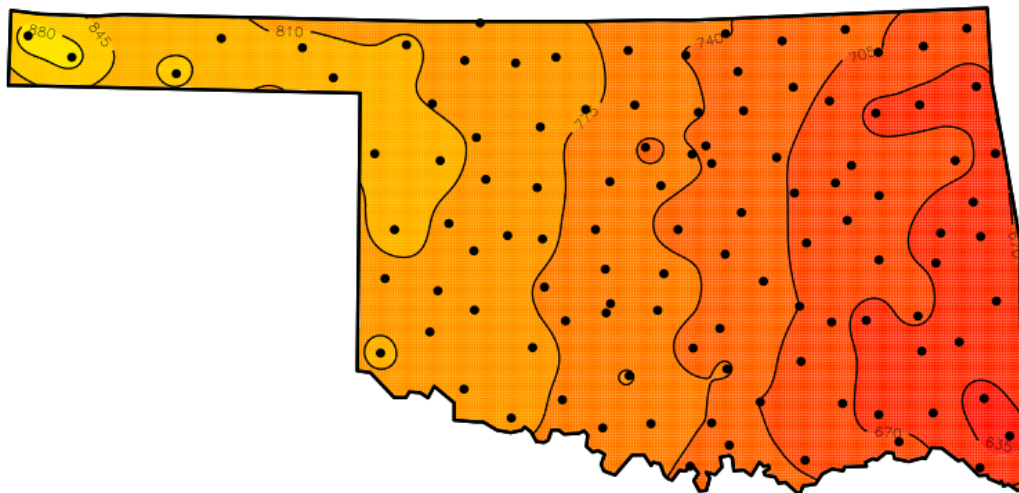
Figure 4.3.3-1. Winter (DJF) Sanyo 2kW mean power production (kWh).
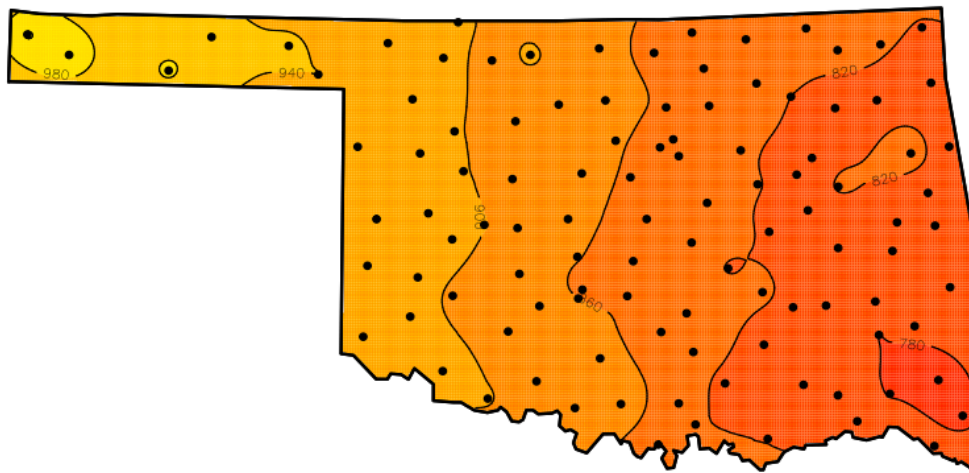
Figure 4.3.3-2. Spring (MAM) Sanyo 2kW mean power production

(kWh).
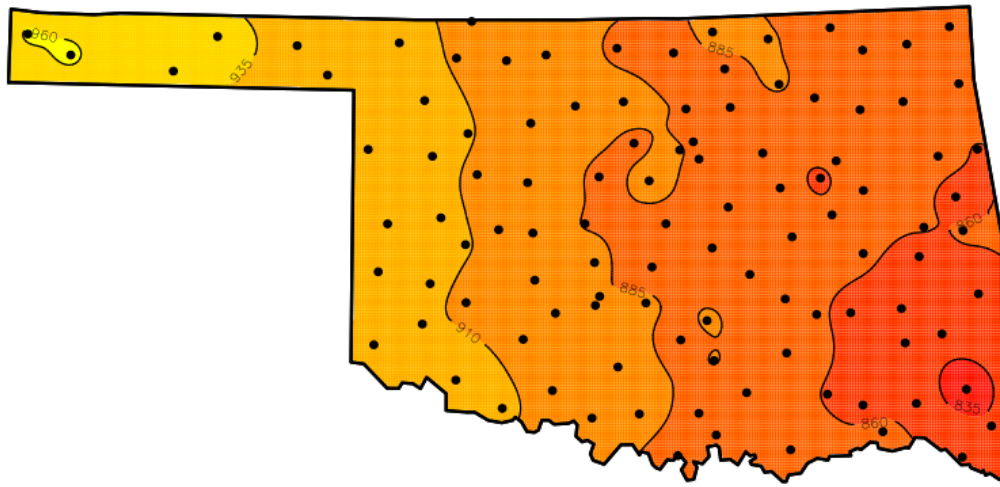
Figure 4.3.3-3. Summer (JJA) Sanyo 2kW mean power production
(kWh).
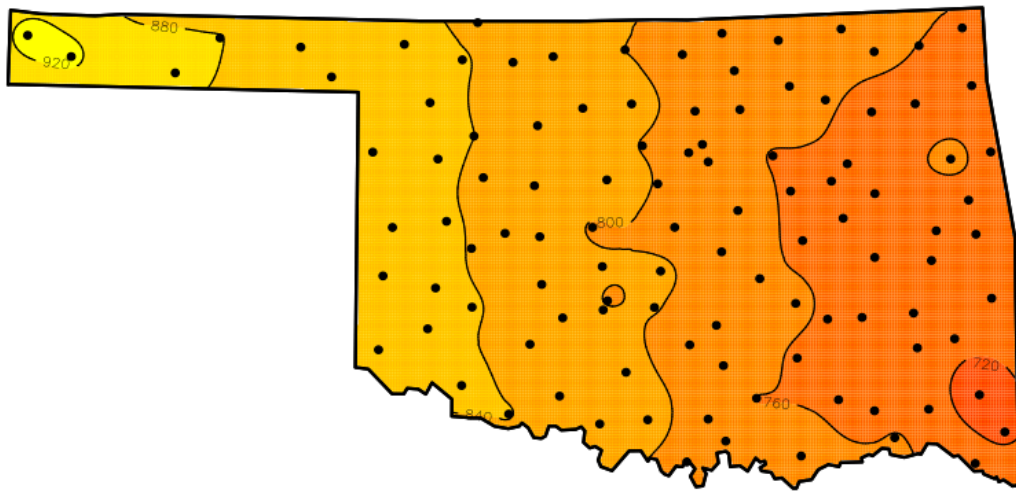
Figure 4.3.3-4. Fall (SON) Sanyo 2kW mean power production (kWh).
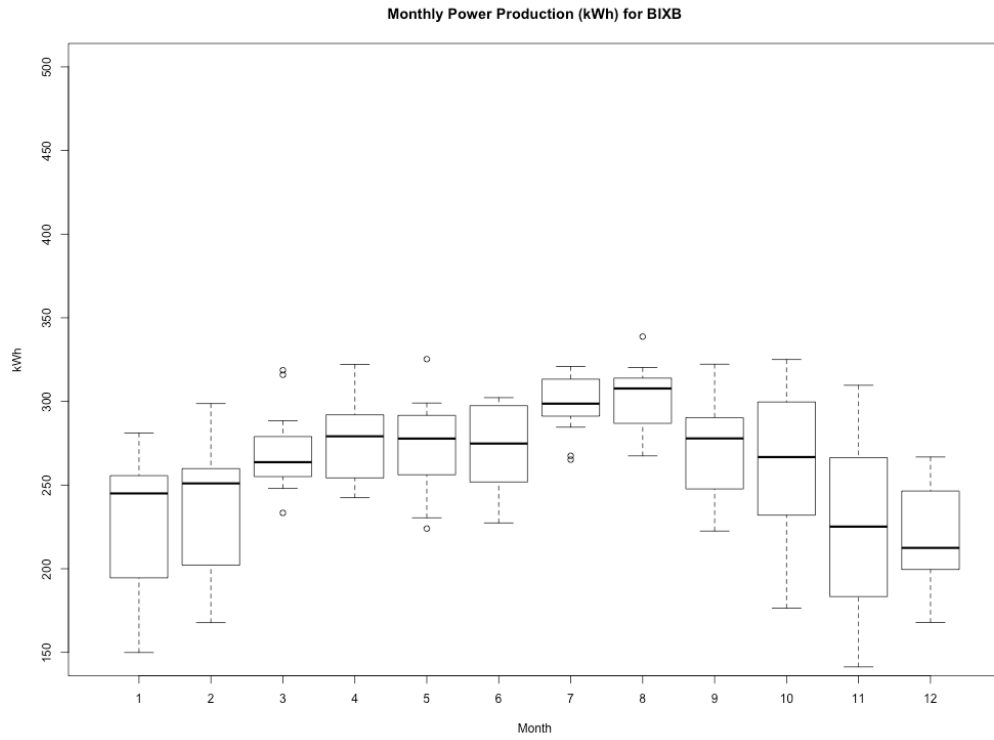
Figure 4.3.3-5. Sanyo 2kW monthly power production for BIXB station (kWh).
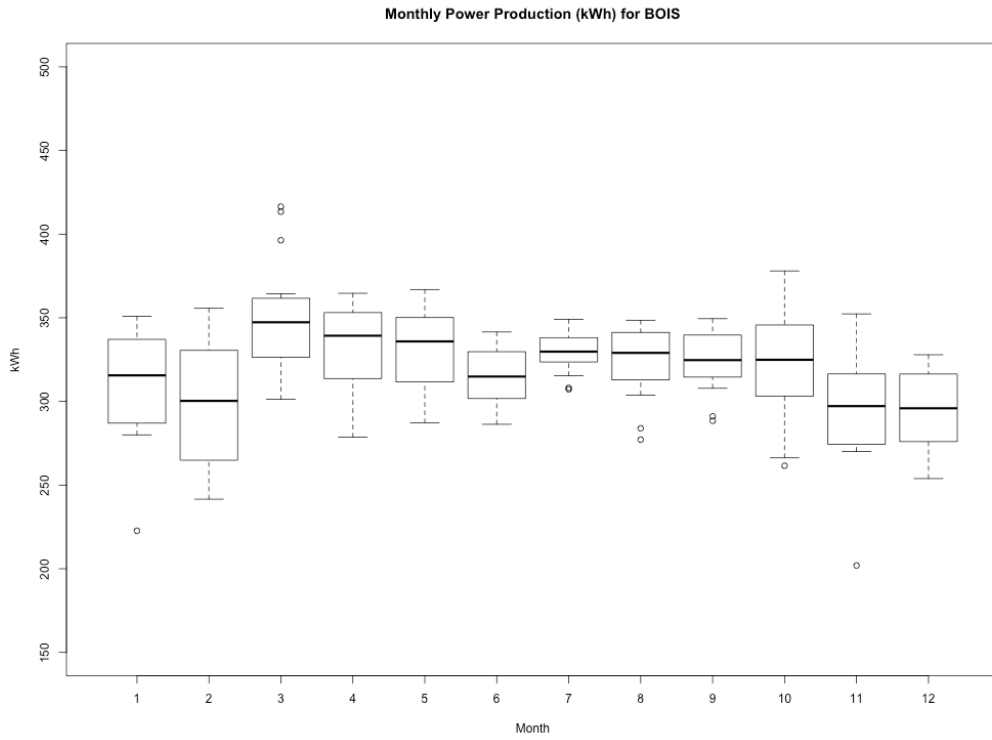
Figure 4.3.3-6. Sanyo 2kW monthly power production for BOIS station

(kWh).

Monthly Power Production (kWh) for MCAL
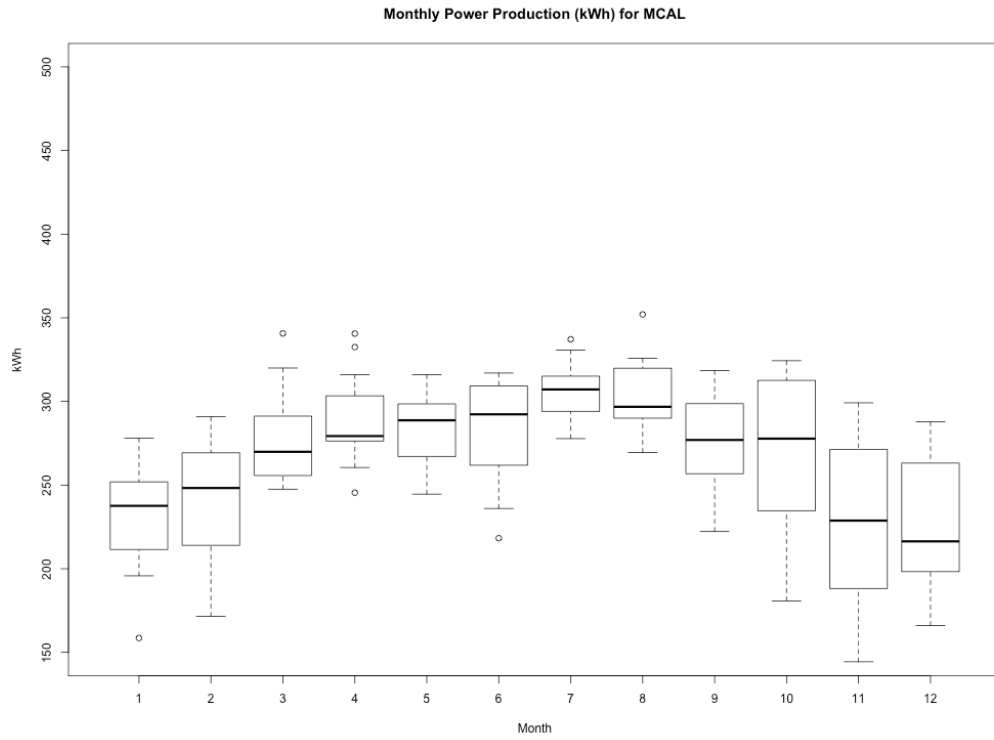
Figure 4.3.3-7. Sanyo 2kW monthly power production for MCAL station (kWh).
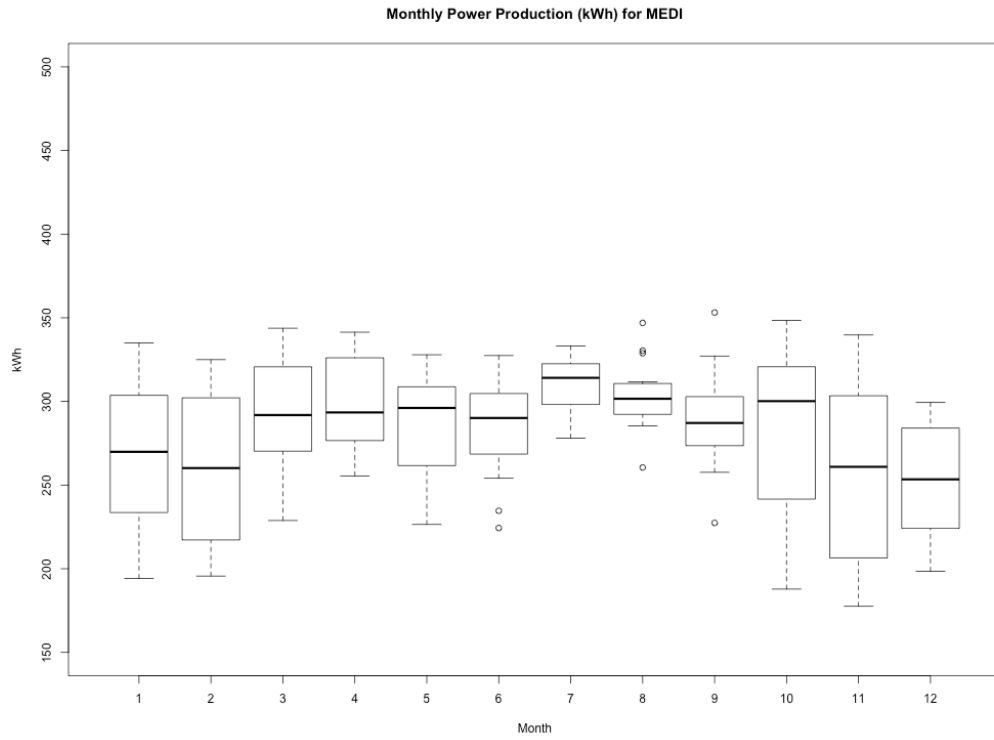
Figure 4.3.3-8. Sanyo 2kW monthly power production for MEDI station

(kWh).
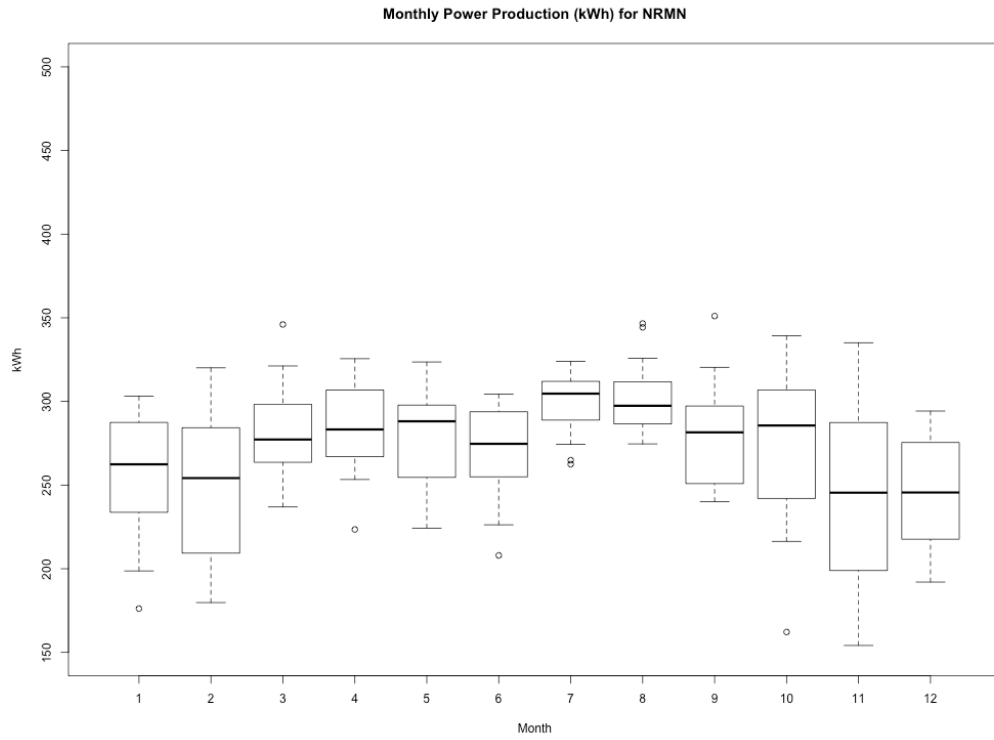
Figure 4.3.3-9. Sanyo 2kW monthly power production for NRMN station

(kWh).
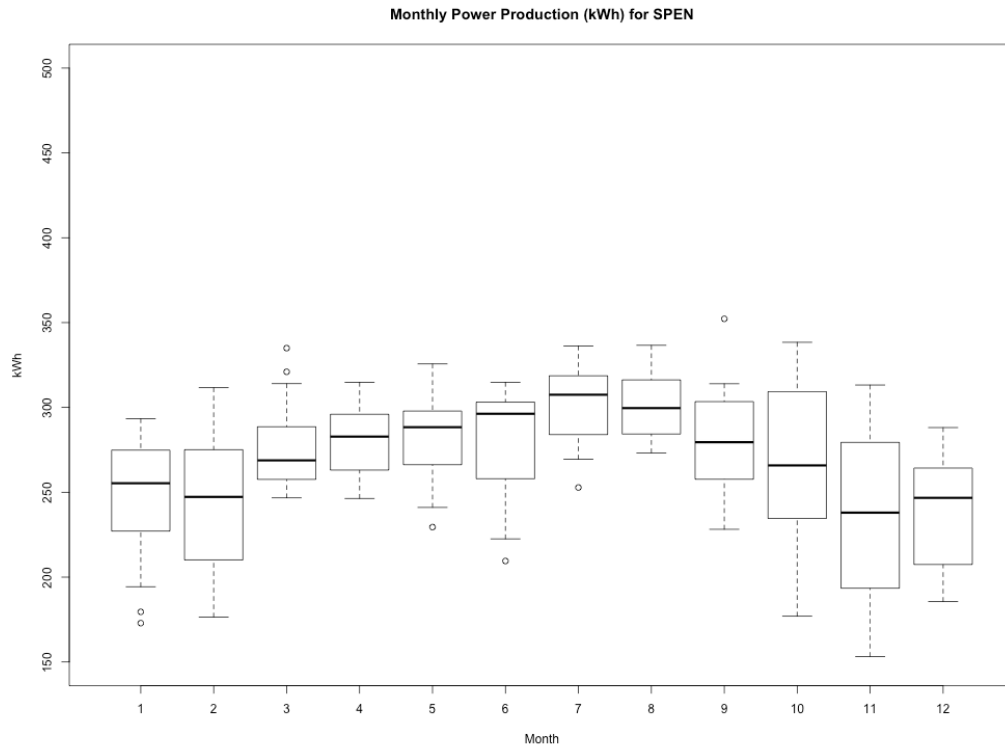
Figure 4.3.3-10. Sanyo 2kW monthly power production for SPEN station

(kWh).

Monthly Power Production (kWh) for WOOD
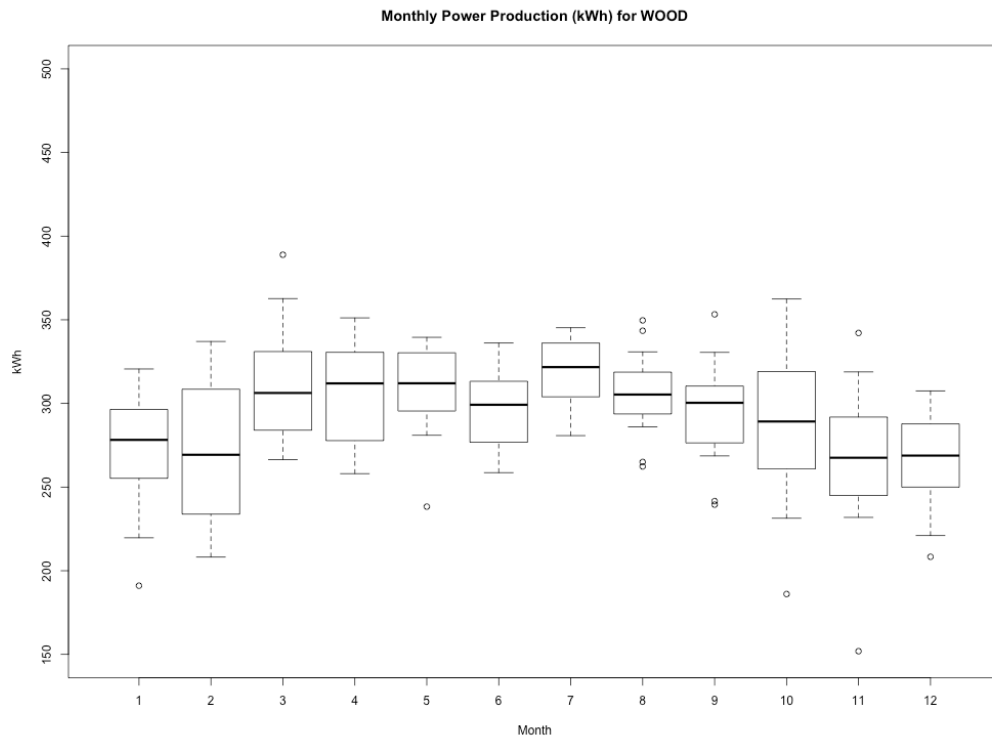
Figure 4.3.3-11. Sanyo 2kW monthly power production for WOOD

station (kWh).
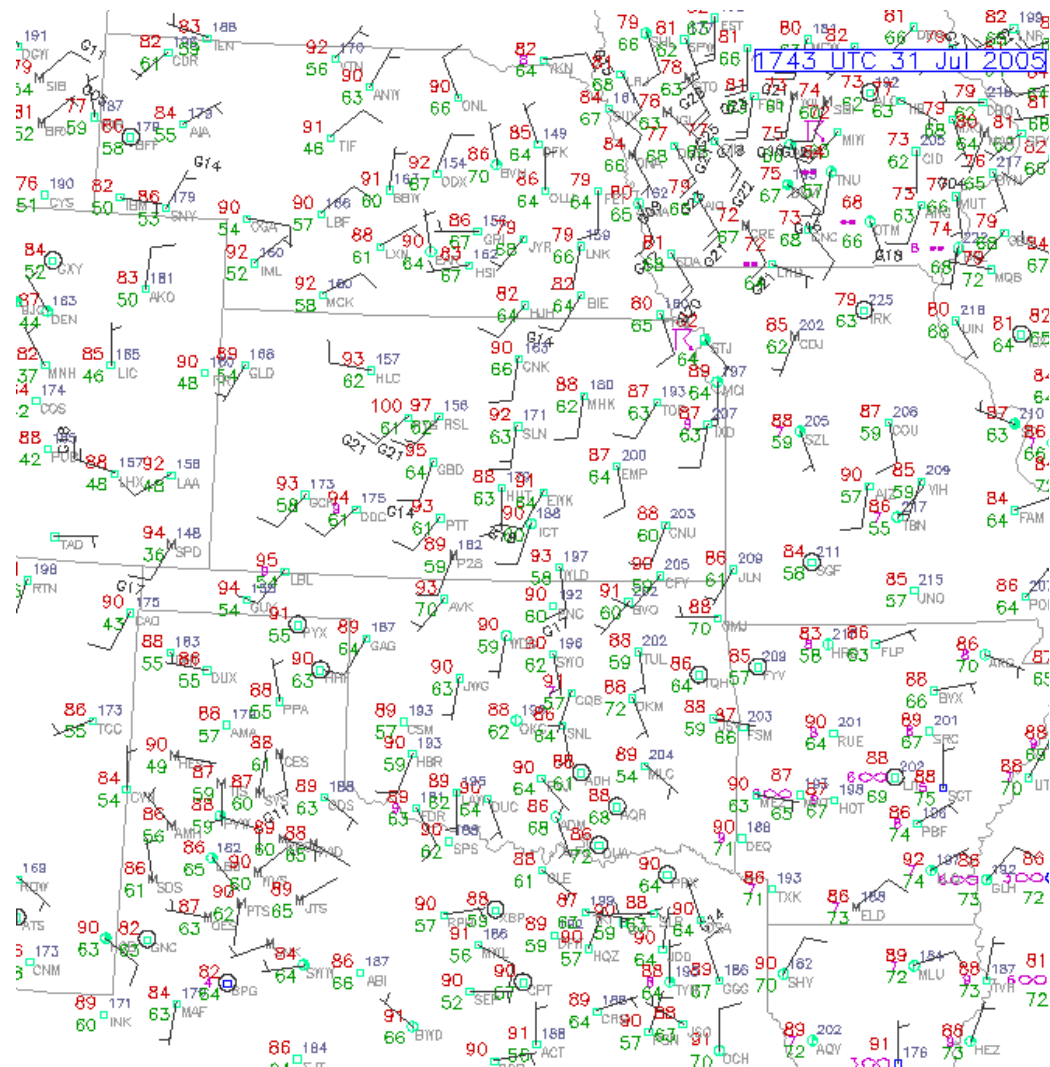
Figure 4.4.1-1. July 31st, 2005. 18Z surface conditions for Clear Day

Case (Image Courtesy of UCAR).
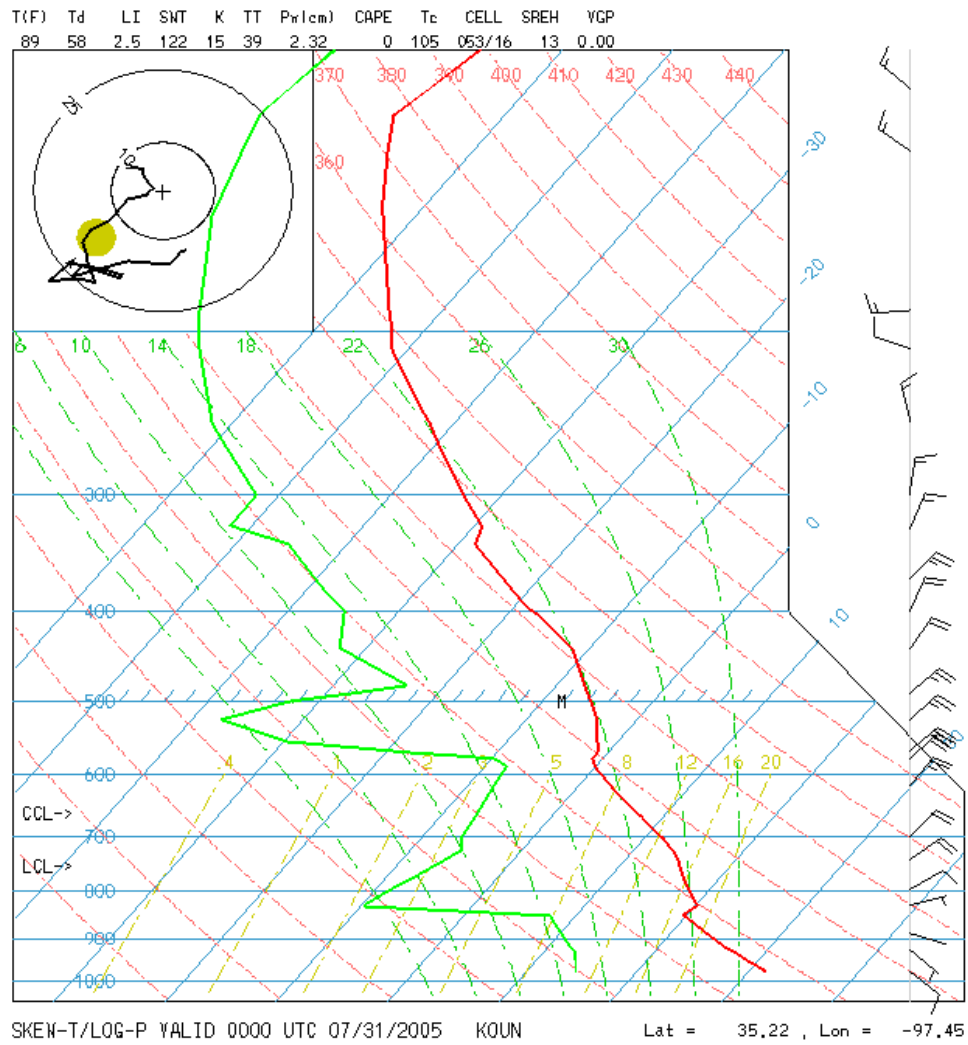
Figure 4.4.1-2. July 31st, 2005. 00Z sounding for Clear Day Case (Image Courtesy UCAR).
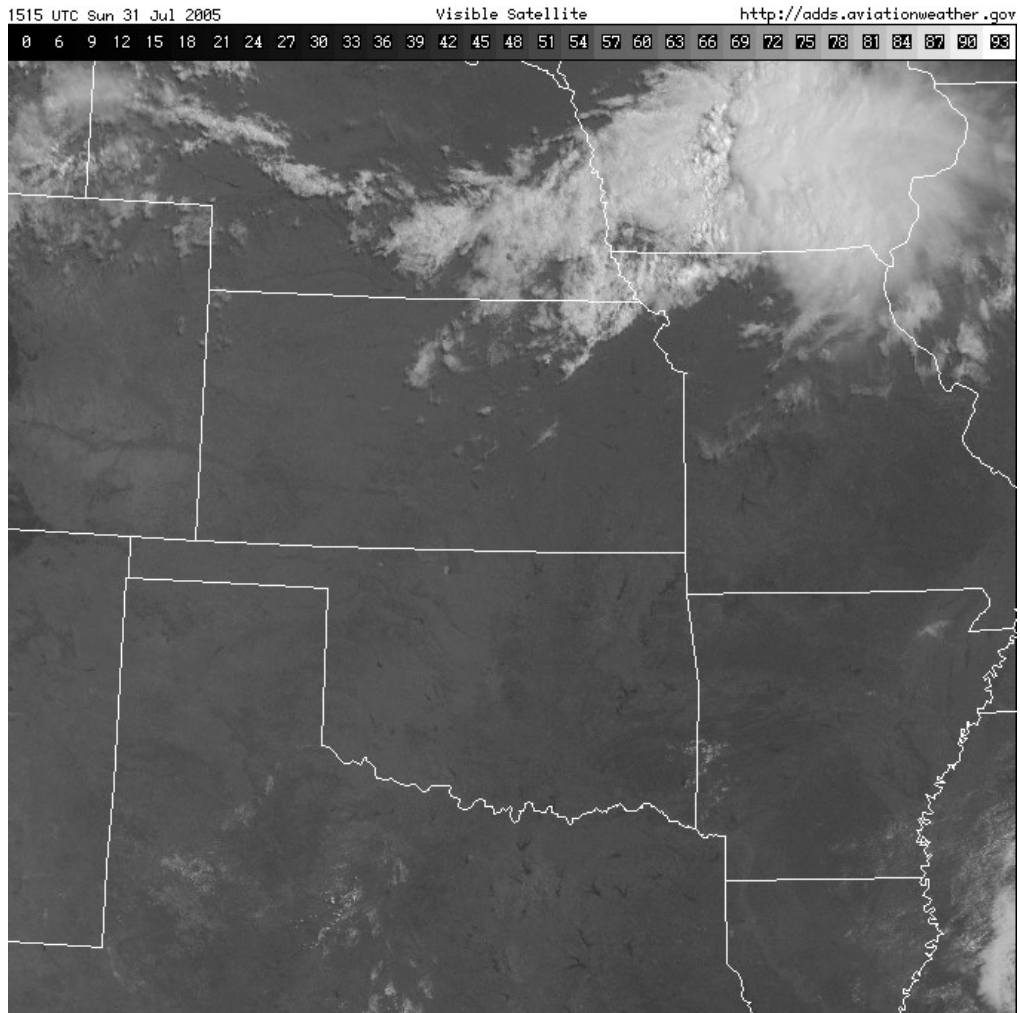
Figure 4.4.1-3. July 31st, 2005. 15Z satellite image for Clear Day Case
(Courtesy of UCAR).
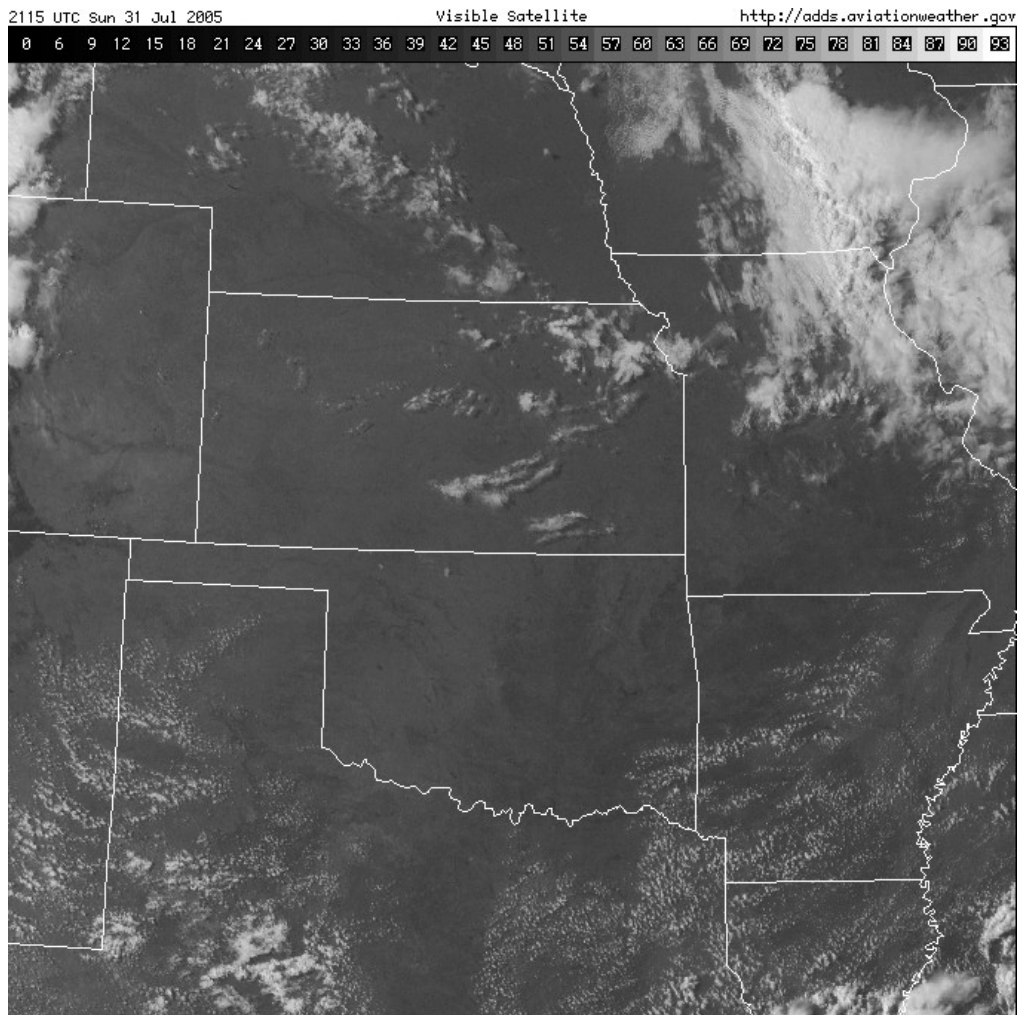
Figure 4.4.1-4. July 31st, 2005. 21Z satellite image for Clear Day Case
(Courtesy of UCAR).

Radiation and Power Production on Clear Day at NRMN 7/31/2005
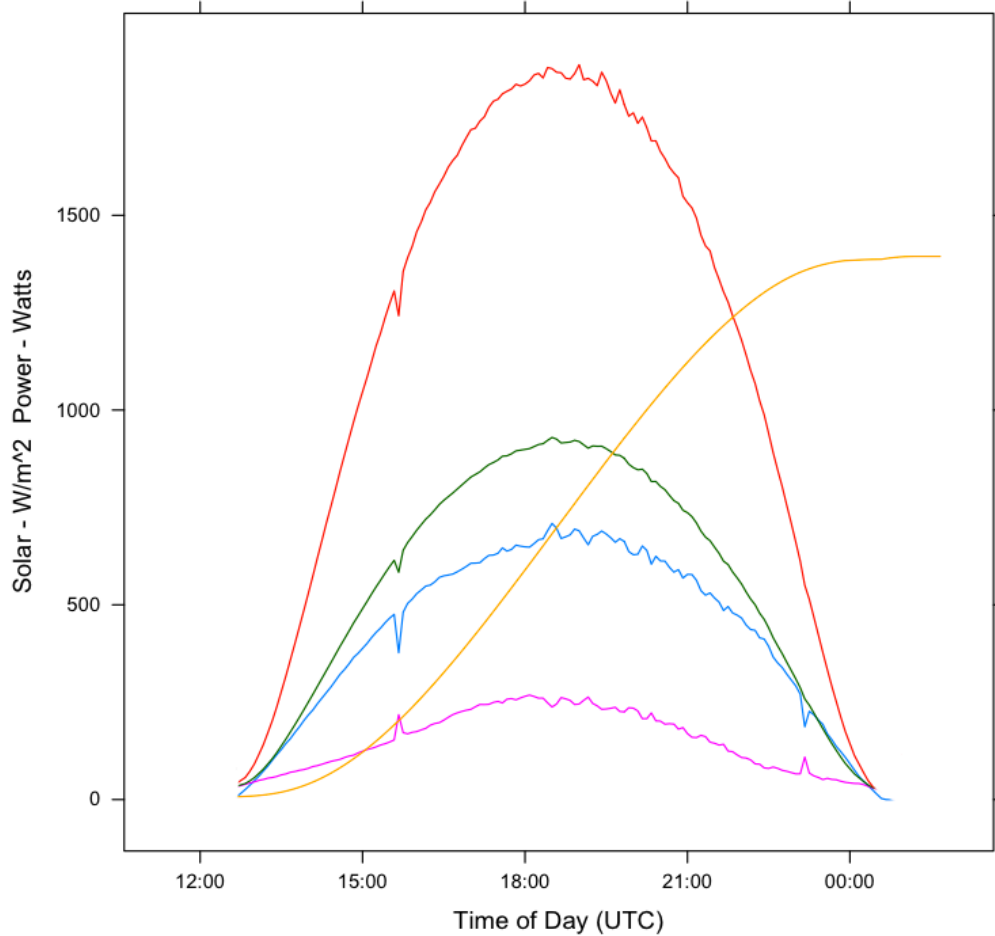
Figure 4.4.1-5. July 31st, 2005. Radiation and power production for

Clear Day Case. The red line indicates instantaneous power output from

the Sharp 2kW array in Watts. The green line is the effective radiation,

the blue line is beam radiation and the pink line is diffuse radiation. All

radiation values are reported in W/m^2. The gold line represents the sum

of the generated power in decawatt-hours (chosen for scale).
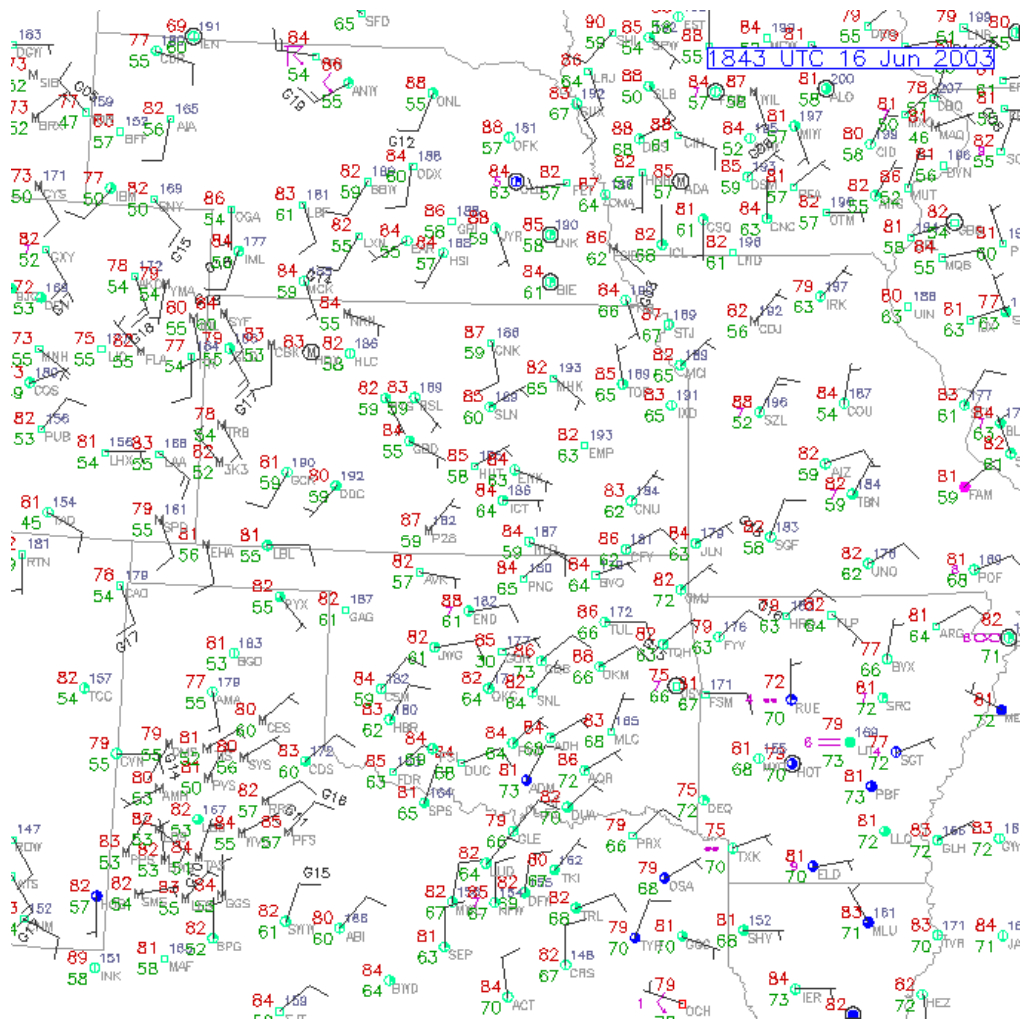
Figure 4.4.2-1. June 16th, 2003. 19Z surface conditions for Clear Day

Case (Courtesy of UCAR).
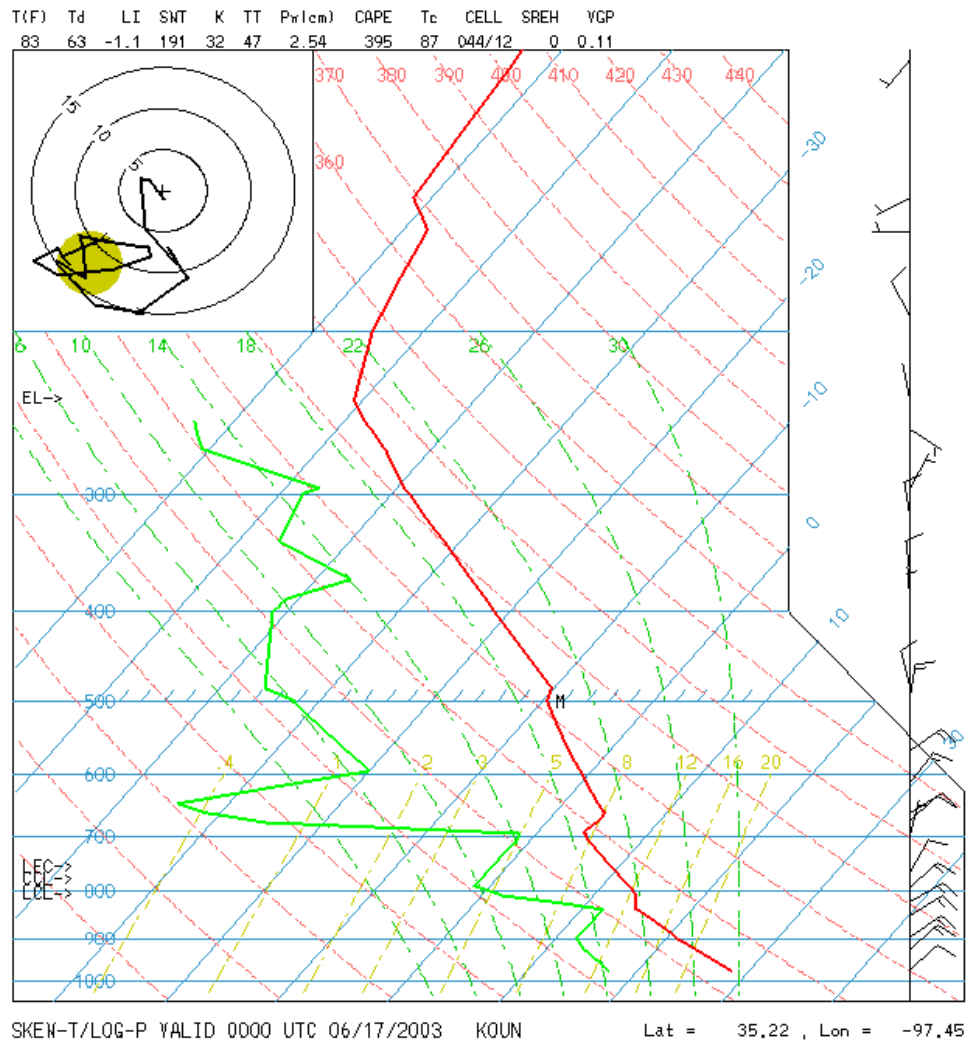
Figure 4.4.2-2. June 16th, 2005. 00Z sounding for Cumulus Day Case

(from 6/17 as 6/16 was not available) (Courtesy of UCAR).

171
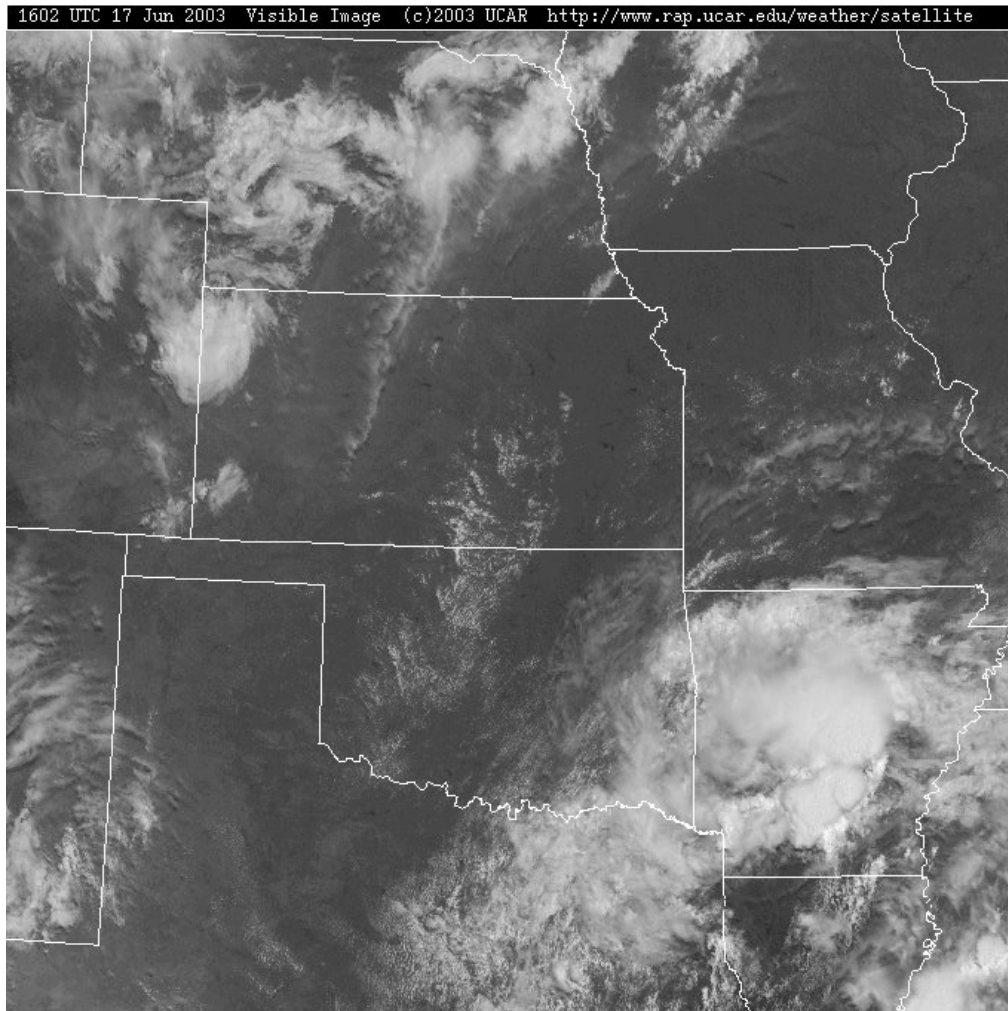
Figure 4.4.2-3. June 16th, 2003. 16Z satellite image for Cumulus Day

Case (Courtesy of UCAR).
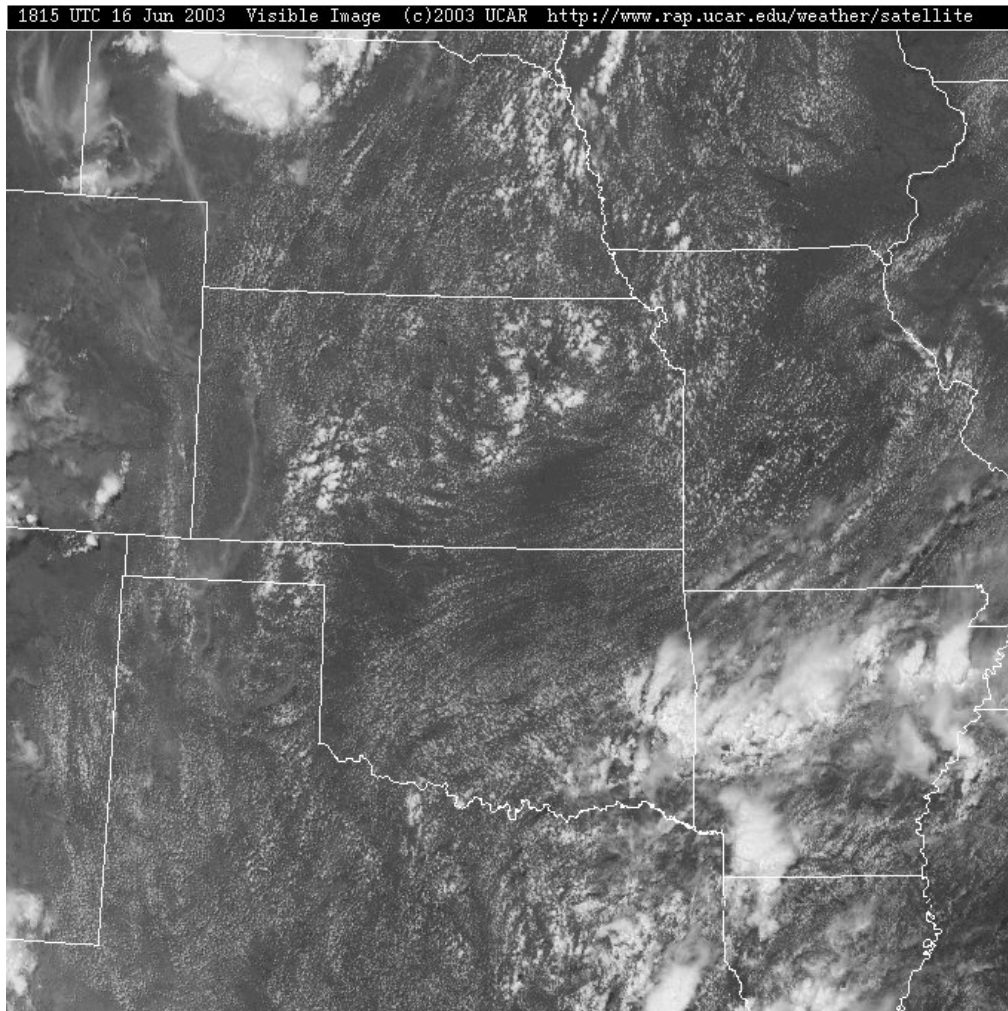
Figure 4.4.2-4. June 16th, 2003. 18Z satellite image for Cumulus Day

Case (Courtesy of UCAR).
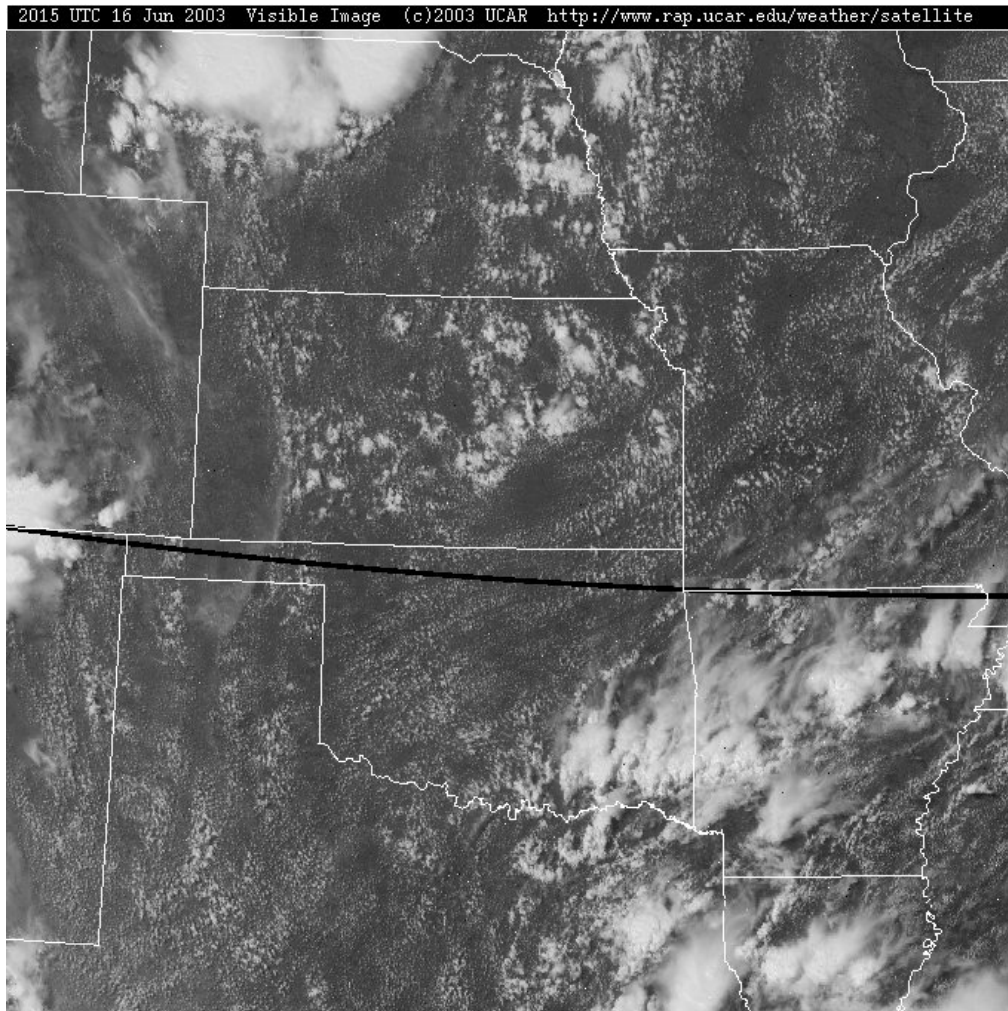
Figure 4.4.2-5. June 16th, 2003. 20Z satellite image for Cumulus Day

Case (Courtesy of UCAR).

**Figure 4.4.2-6.** June 16th, 2003. Radiation and power production for Cumulus Day Case, same as Figure 4.4.1-5.
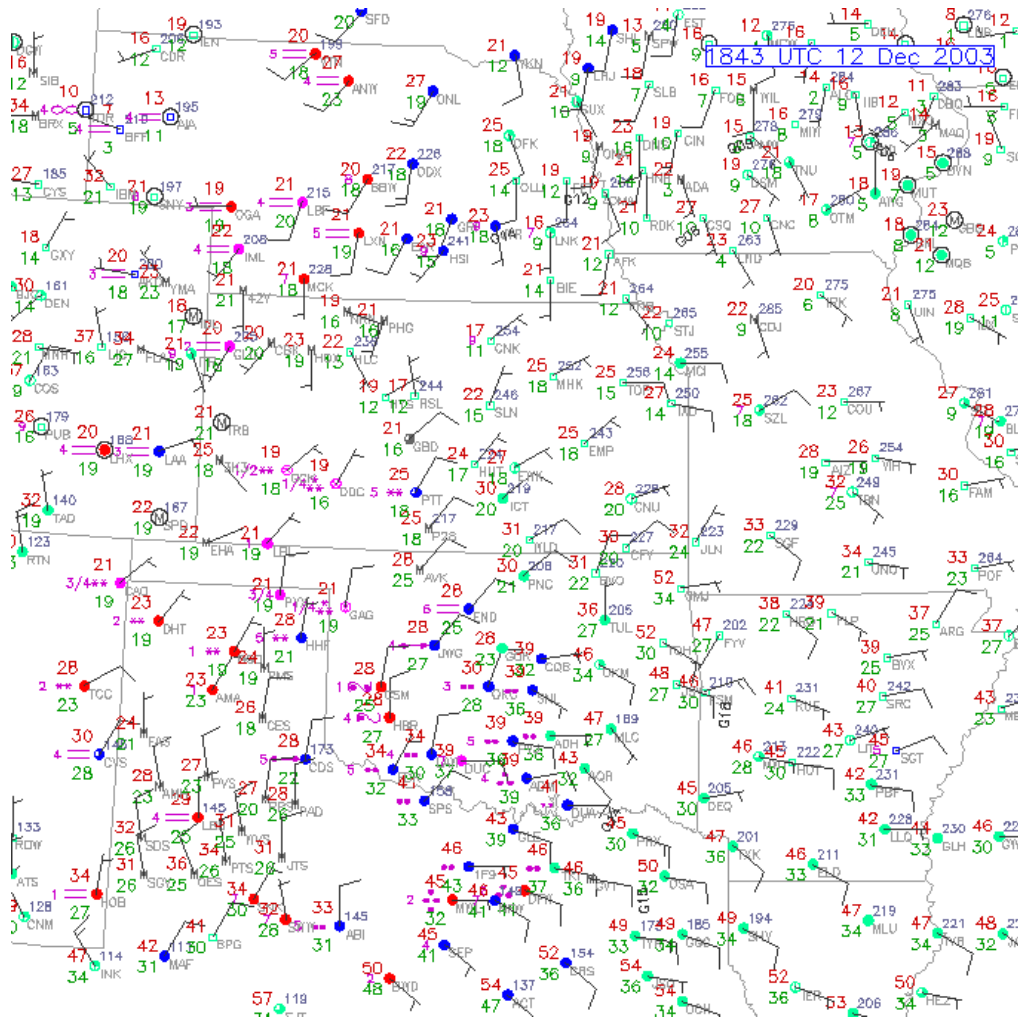
Figure 4.4.3-1. December 12th, 2003. 19Z surface conditions for

Cumulus Day Case (Courtesy of UCAR).
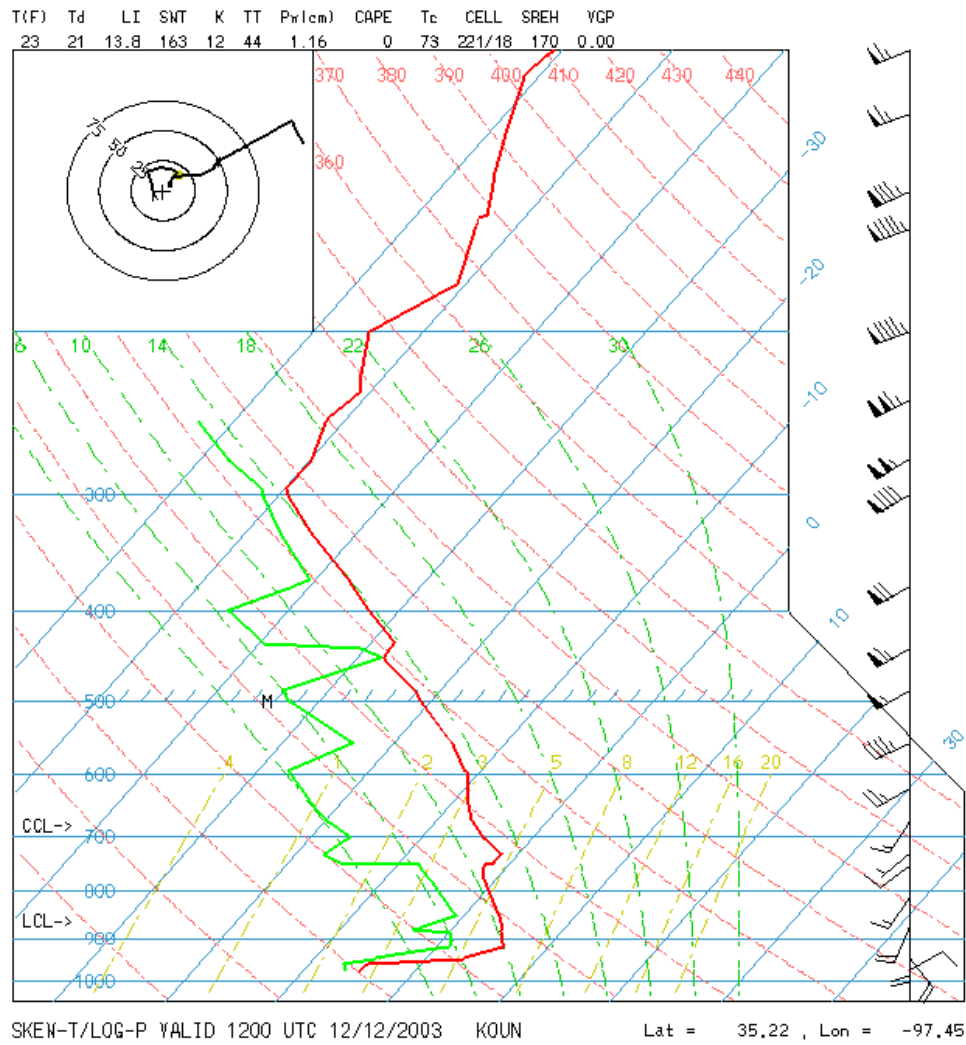
Figure 4.4.3-2. December 12th, 2005. 12Z OUN sounding for Overcast

Day Case (Courtesy of UCAR).
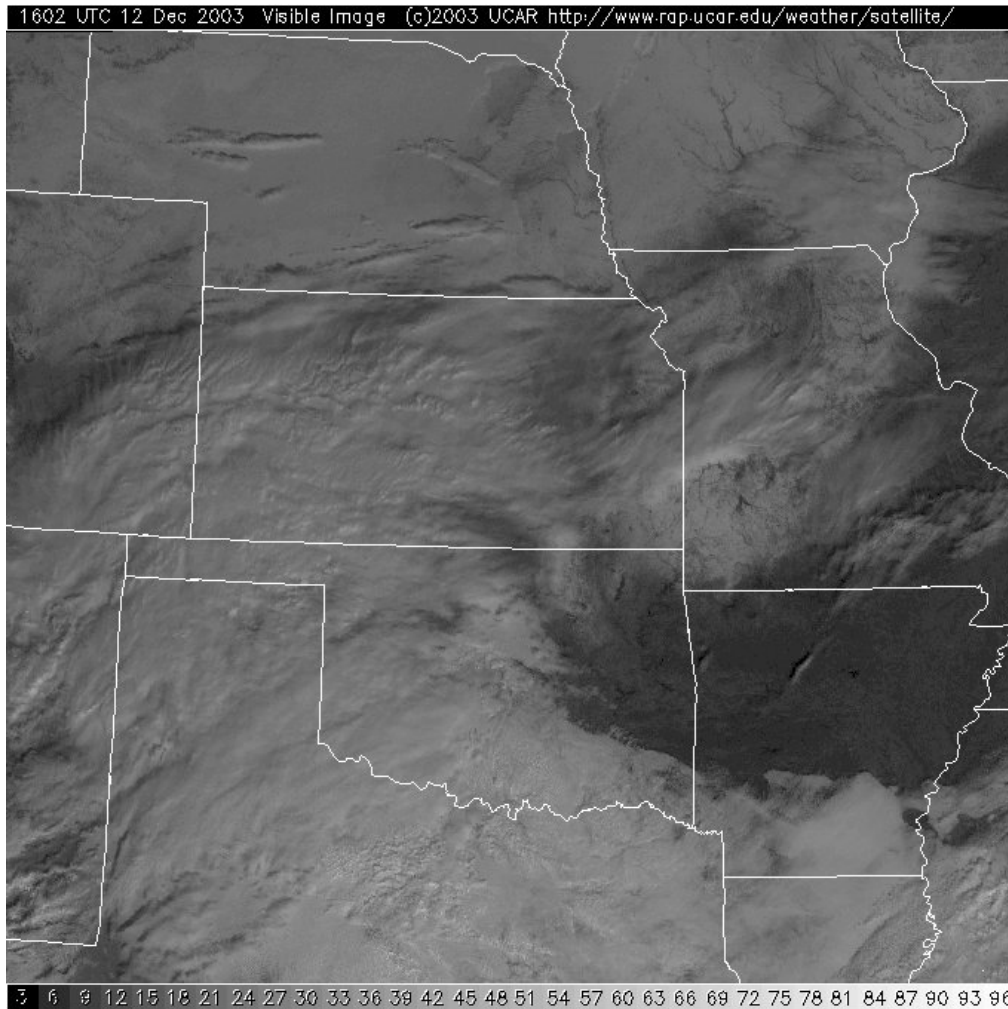
Figure 4.4.3-3. December 12th, 2003. 16Z satellite image for Overcast
Day Case (Courtesy of UCAR).
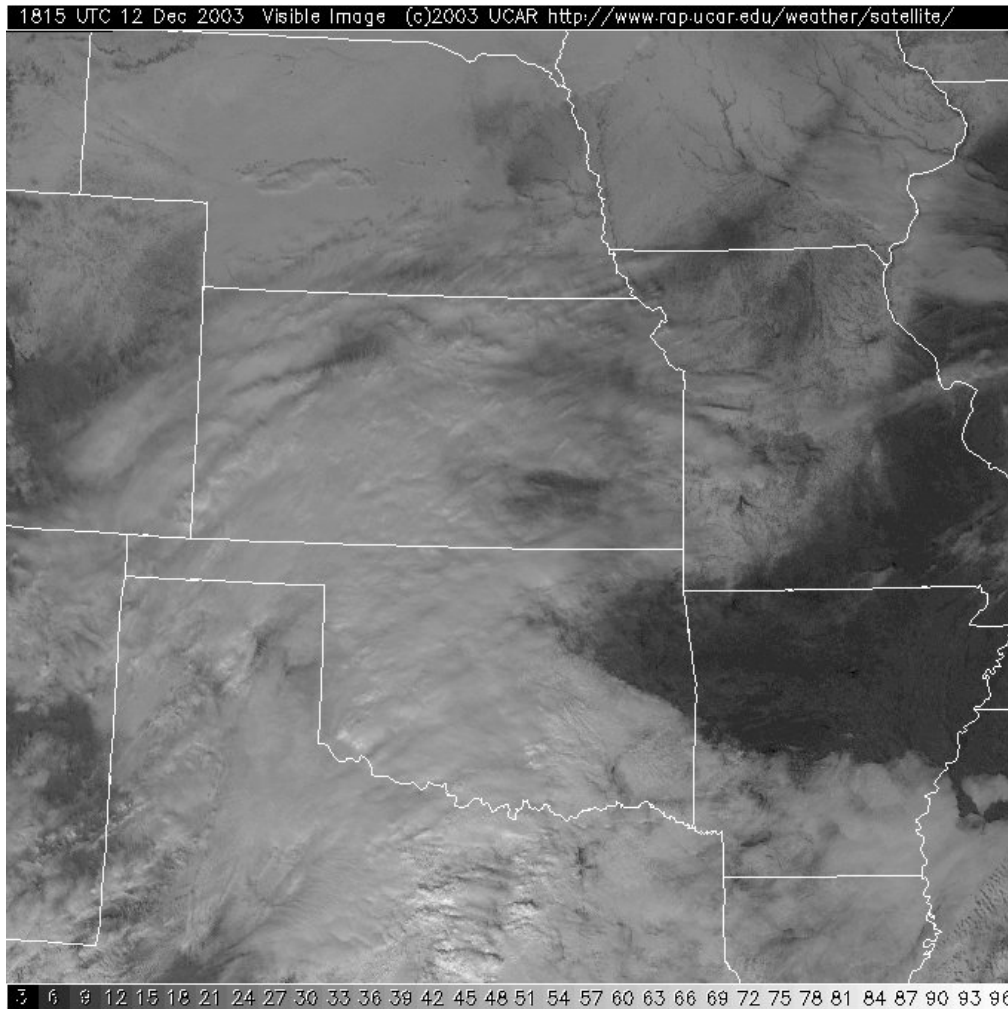
Figure 4.4.3-4. December 12th, 2003. 18Z satellite image for Overcast

Case (Courtesy of UCAR).
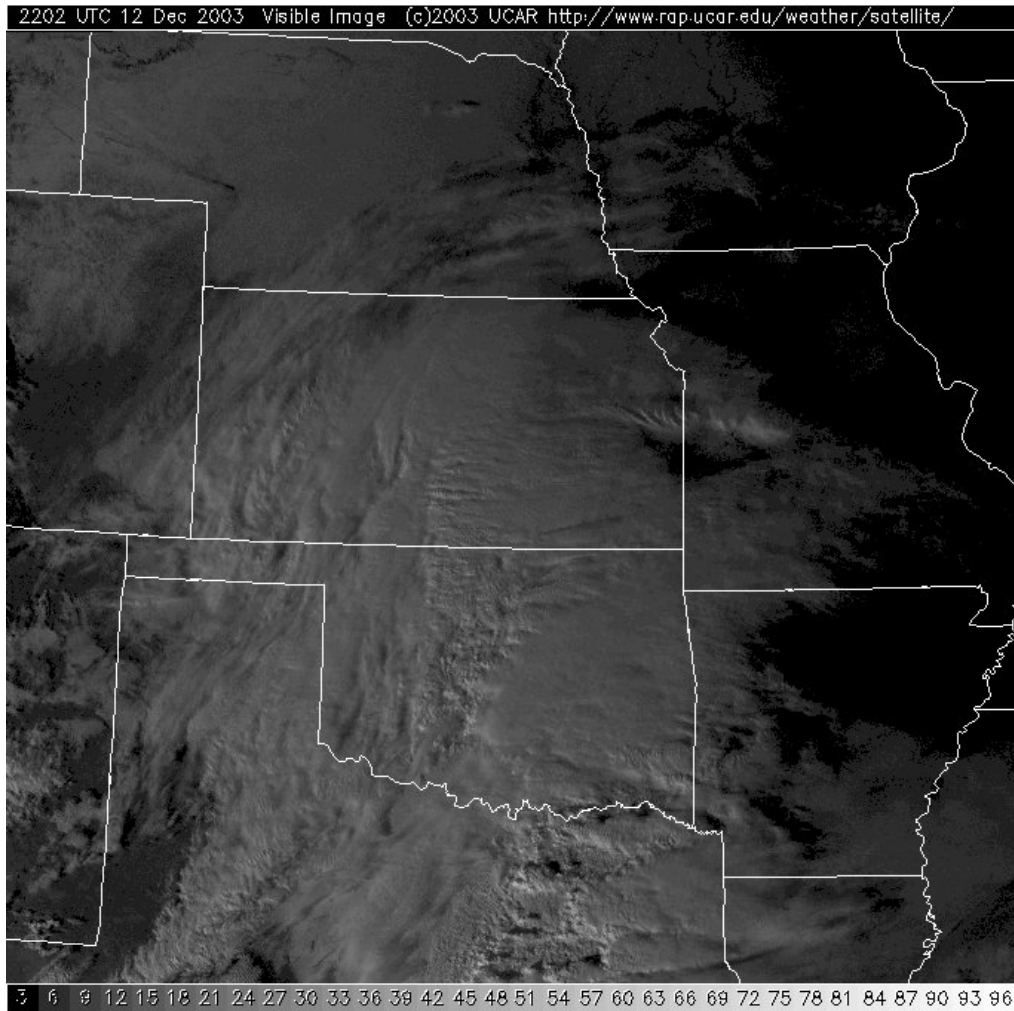
Figure 4.4.3-5. December 12th, 2003. 22Z satellite image Overcast

Day Case (Courtesy of UCAR).

Figure 4.4.3-6. December 12th, 2003. Radiation and power production

for Overcast Day Case. Same as Figure 4.4.1-5.
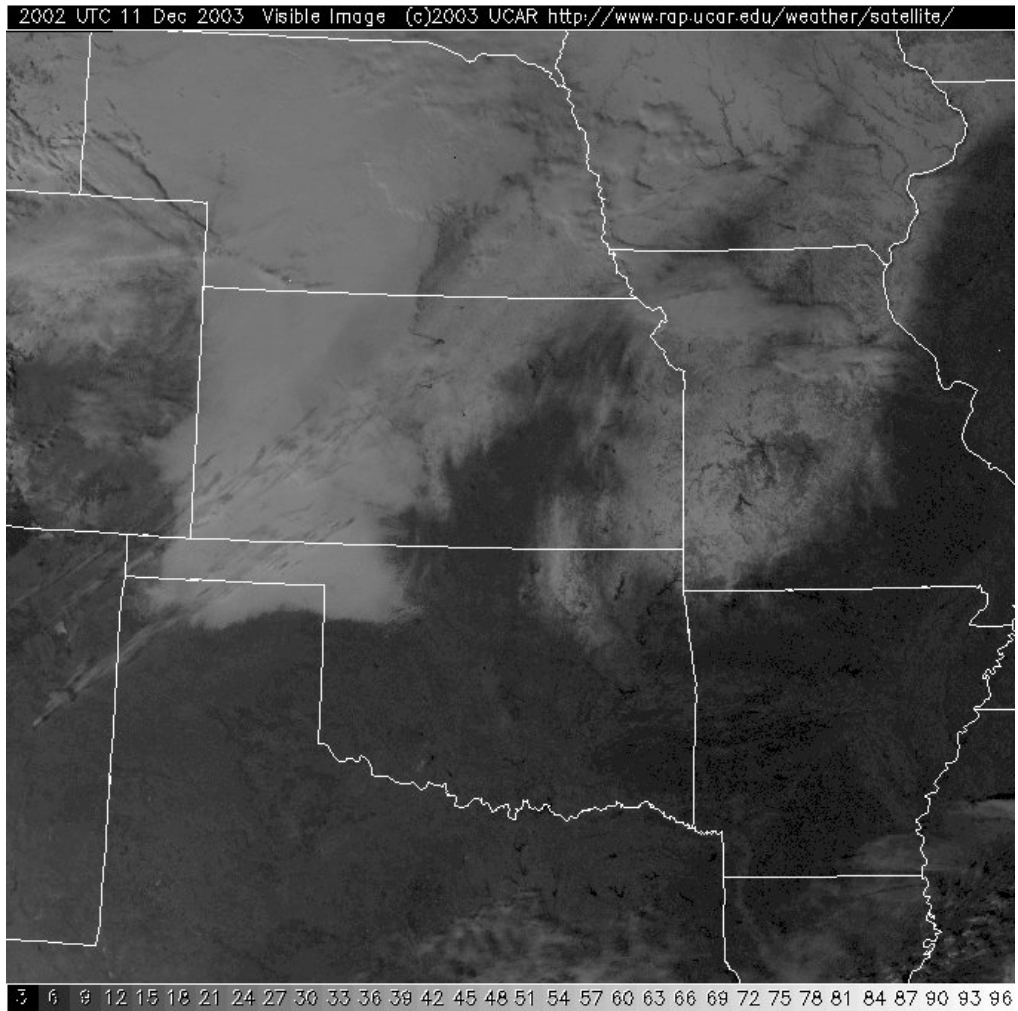
Figure 4.4.3-7. December 11th, 2003. 20Z satellite image for day

previous to Overcast Day Case for comparison (Courtesy of UCAR).

Radiation and Power Production on Clear Day at NRMN 12/11/2003
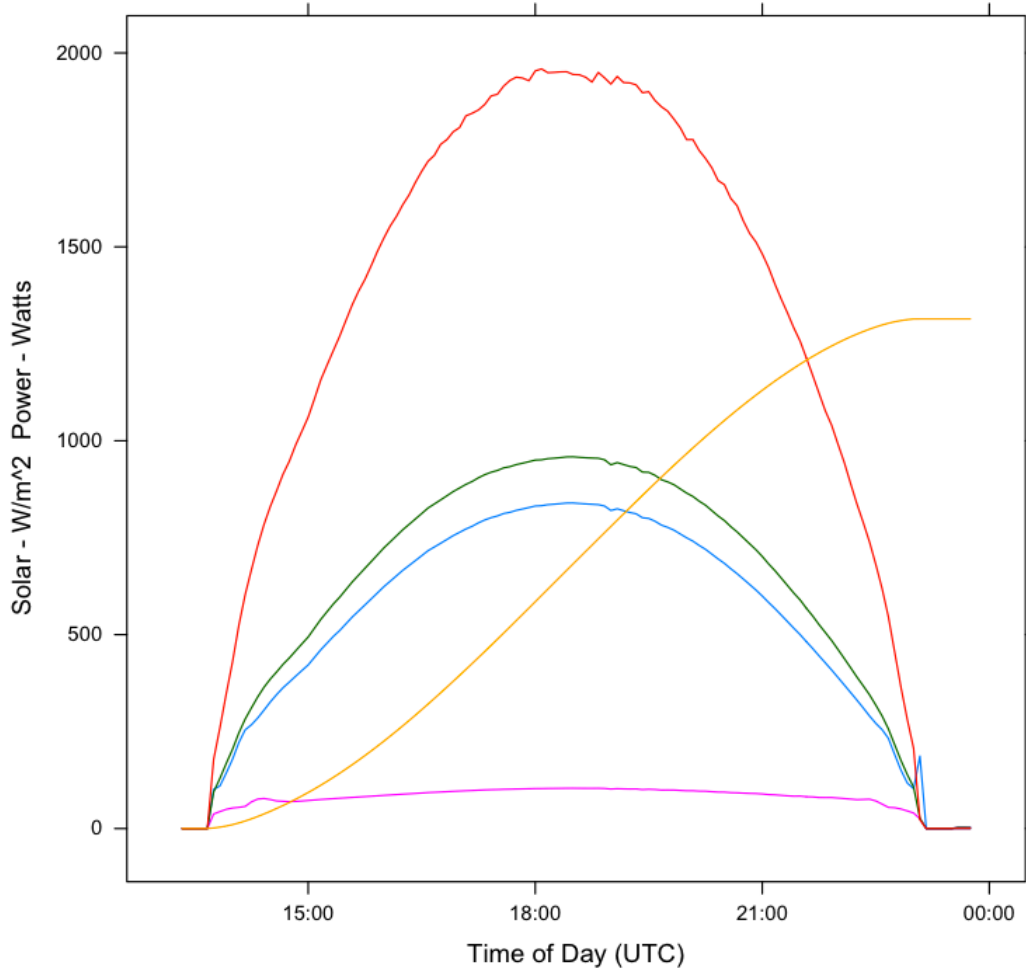
Figure 4.4.3-8. December 11th, 2003. Radiation and power production for the clear day previous to the Overcast Day Case for comparison. Same as Figure 4.4.1-5.
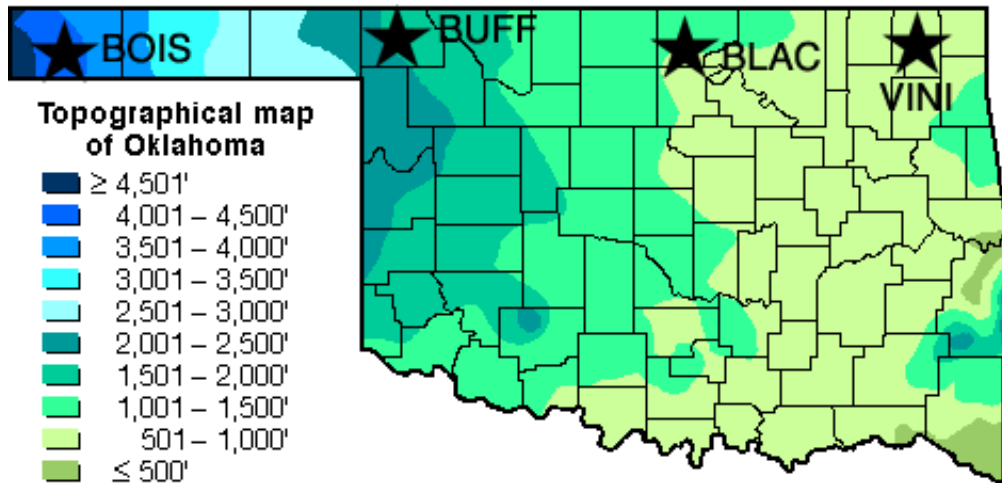
Figure 4.5.1-1. Topographic map of Oklahoma showing location

elevation in feet. Stars denote the locations of the Mesonet stations

chosen for the elevation analysis. (Courtesy of OCS).
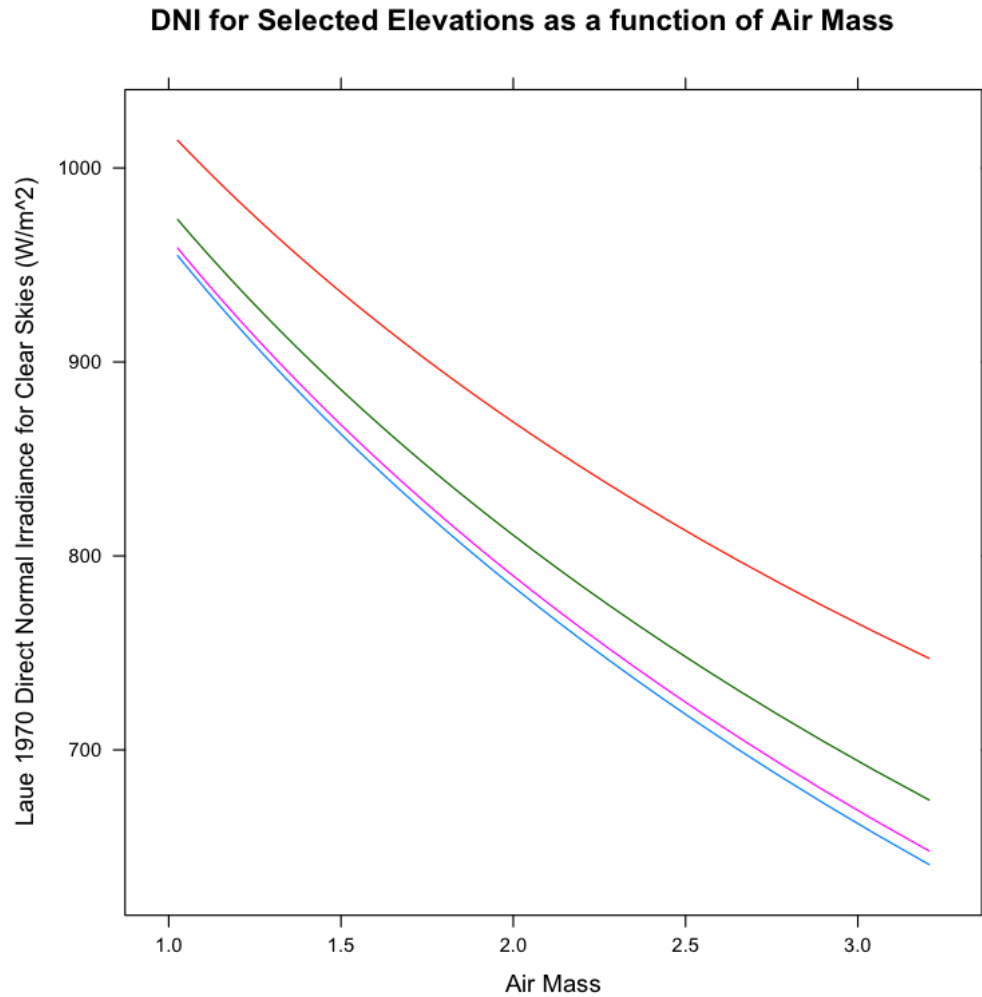
Figure 4.5.1-2. Direct Normal Irradiance values as calculated in Laue

1970 are plotted as a function of air mass for selected elevations. Lines

are colored as follows by increasing elevation: VINI - blue (263m), BLAC

– pink (304m), BUFF – green (559m) and BOIS – red (1267m).
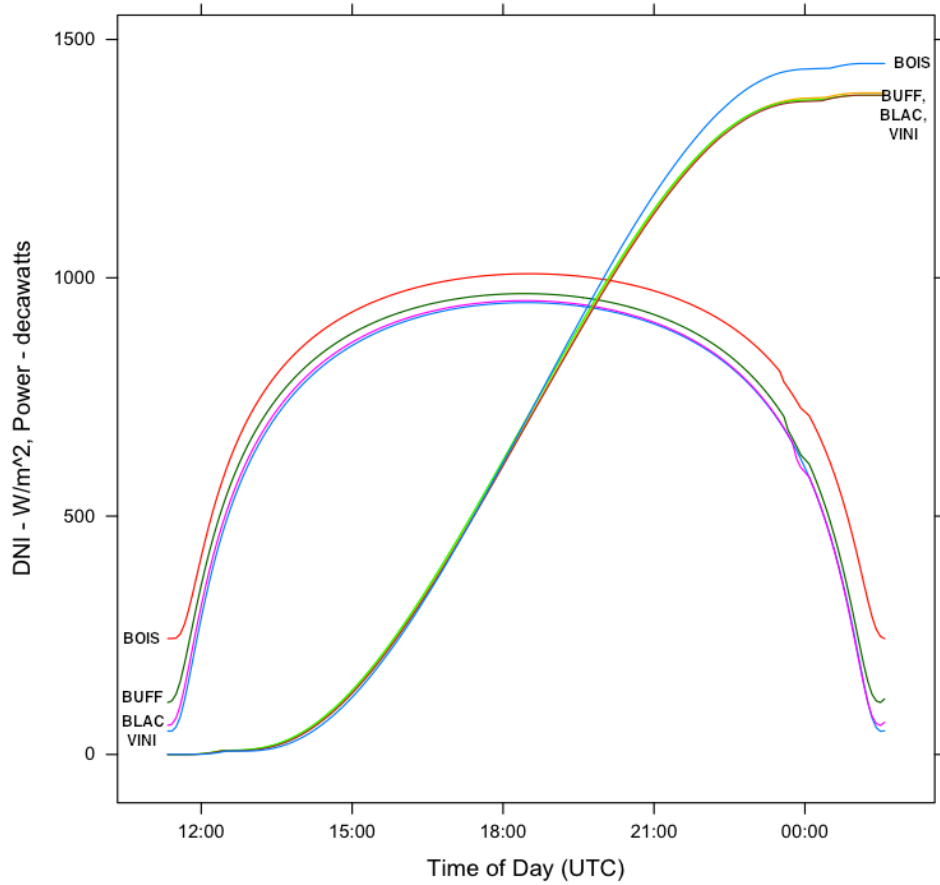
Figure 4.5.1-3. Estimated DNI and resulting power production under

clear skies for July 31st, 2005. DNI values are given by the sinusoidal

curve as follows: VINI (blue), BLAC (pink), BUFF (green) and BOIS

(red). Total power production is given in decawatt-hrs by the remaining

four lines as follows: BOIS (teal), BUFF (gold), BLAC (green), VINI

(brown).
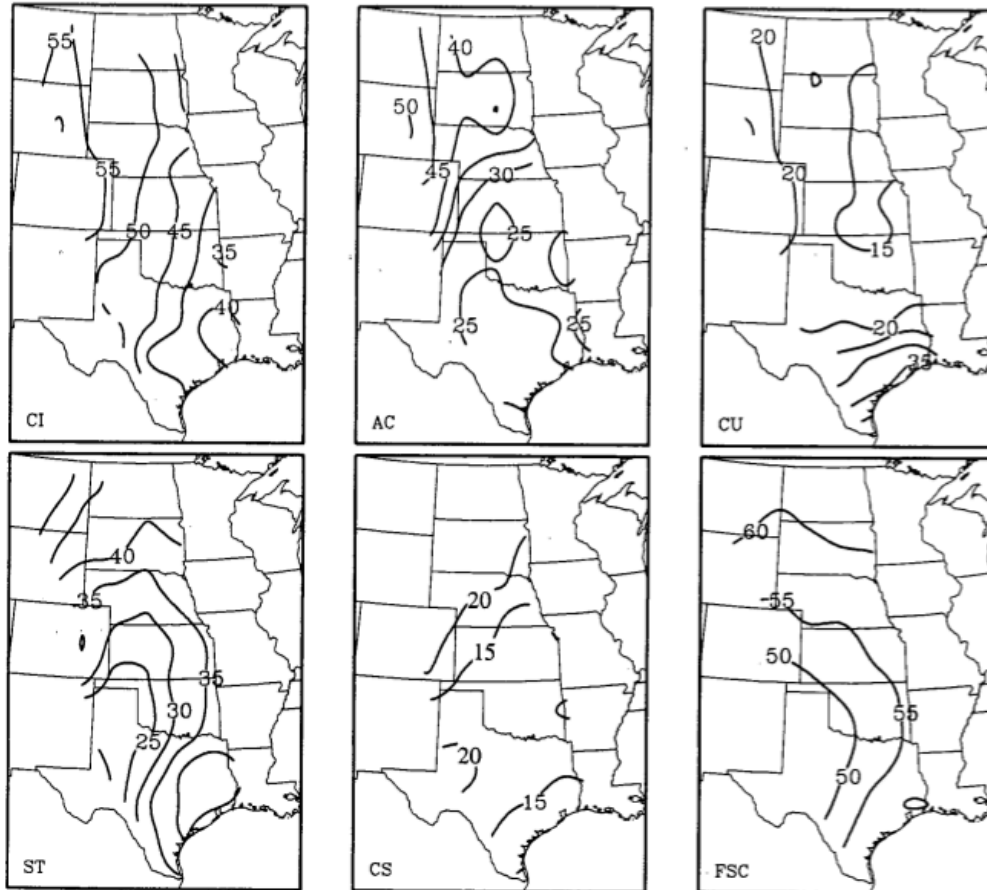
Figure 4.5.2-1. Spatial patterns of annual mean frequency of occurrence of different cloud types between 1952-1991: Cirrus (CI), Altocumulus (AC), Cumulus (CU), Stratus (ST), Clear Sky (CS), Fractional Sky Cover (FSC). Values for cloud types are percentages of observations of a given type while FSC is given as the percentage of total coverage of the sky hemisphere. Adapted from McManus 1999 Figure 3.1.
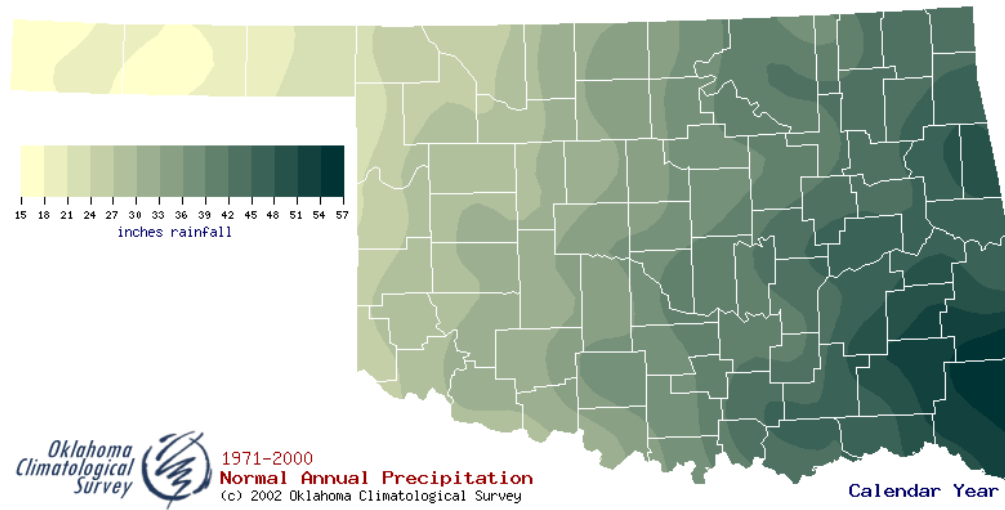
**Figure 4.5.2-2.** Climatological mean precipitation for 1971-2000 (Image courtesy of OCS).

Normal Rainfall
Winter 2007-2008

Dec 1, 2007 through Feb 29, 2008
Created 2009-09-22 16:24:48 UTC. Copyright © 2009
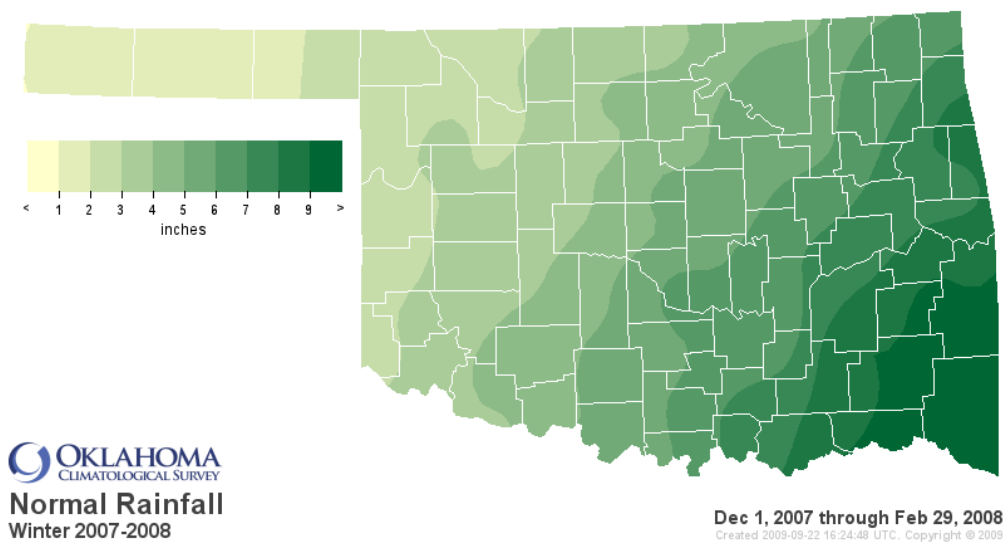
Figure 4.5.3-1. Climatological mean seasonal precipitation for winter

(DJF) (Courtesy OCS).
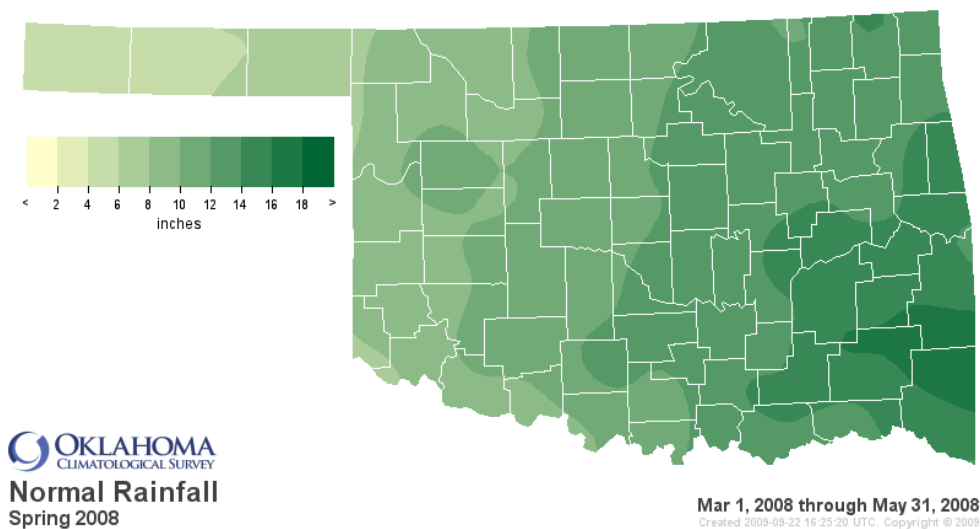
Figure 4.5.3-2. Climatological mean seasonal precipitation for spring

(MAM) (Courtesy OCS).
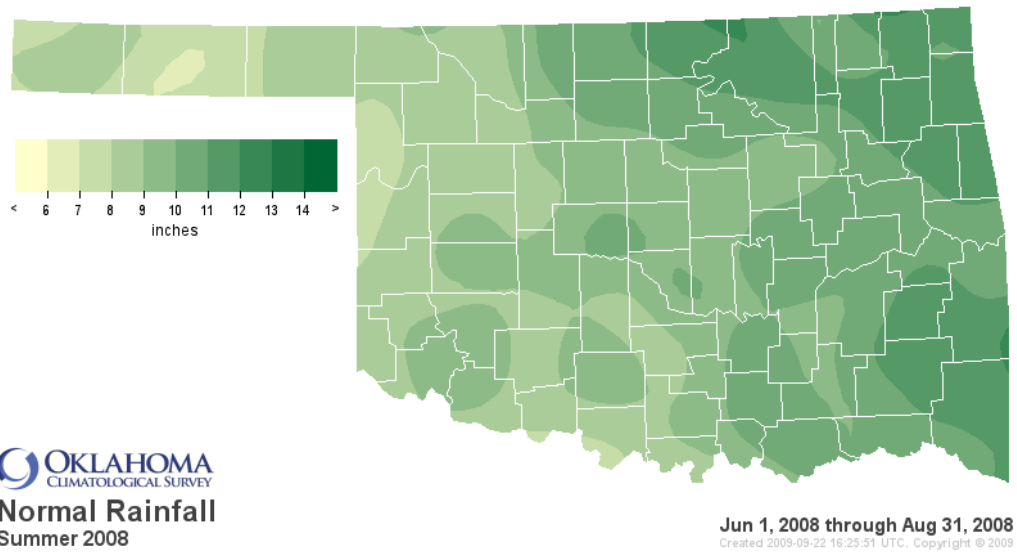
**Figure 4.5.3-3.** Climatological mean seasonal precipitation for summer

(JJA) (Courtesy OCS).
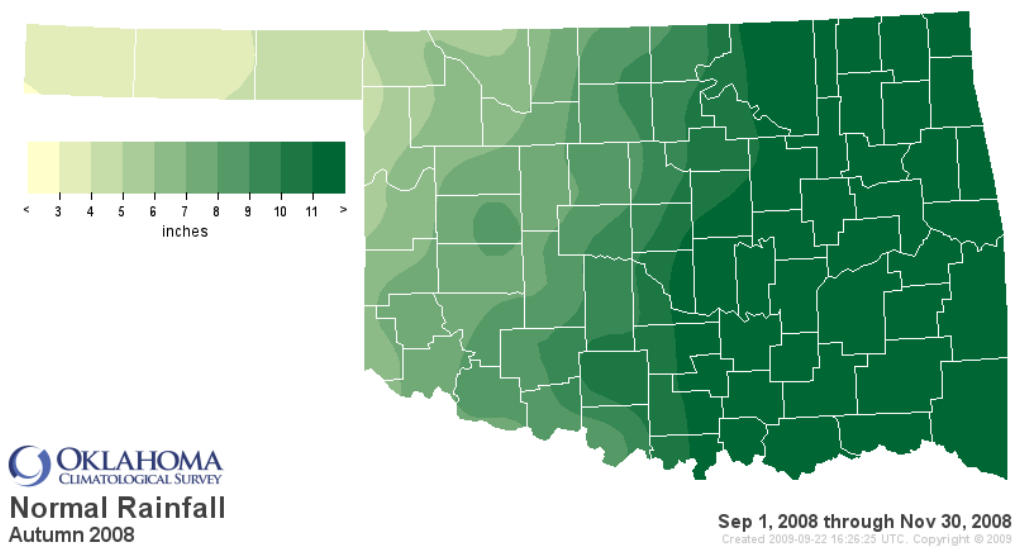
**Figure 4.5.3-4.** Climatological mean seasonal precipitation for autumn (SON) (Courtesy OCS).
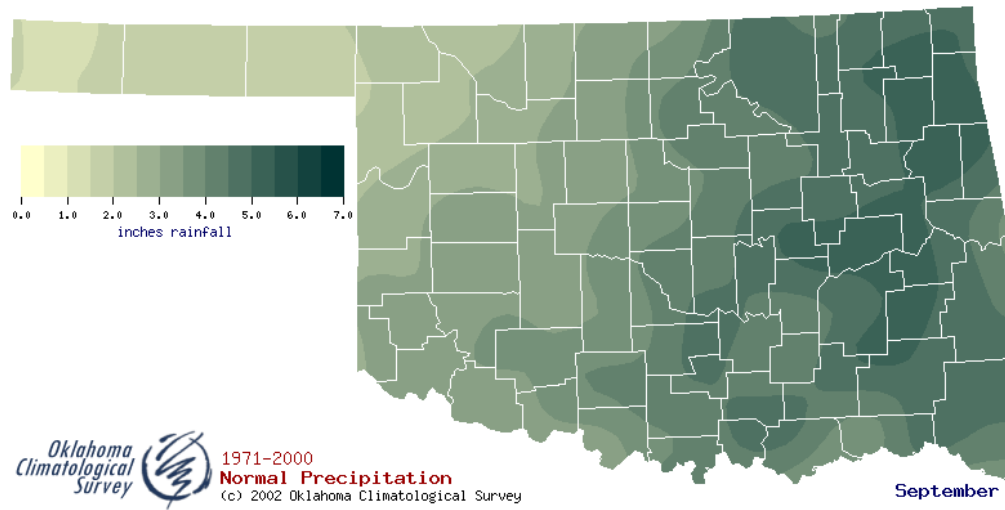
**Figure 4.5.3-5.** Climatological mean precipitation for September

(Courtesy OCS).
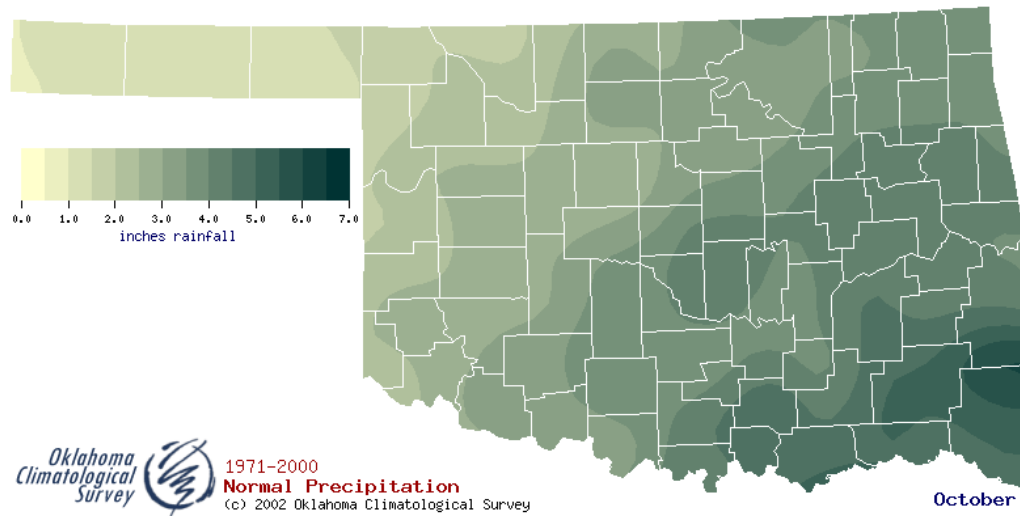
**Figure 4.5.3-6.** Climatological mean precipitation for October (Courtesy OCS).
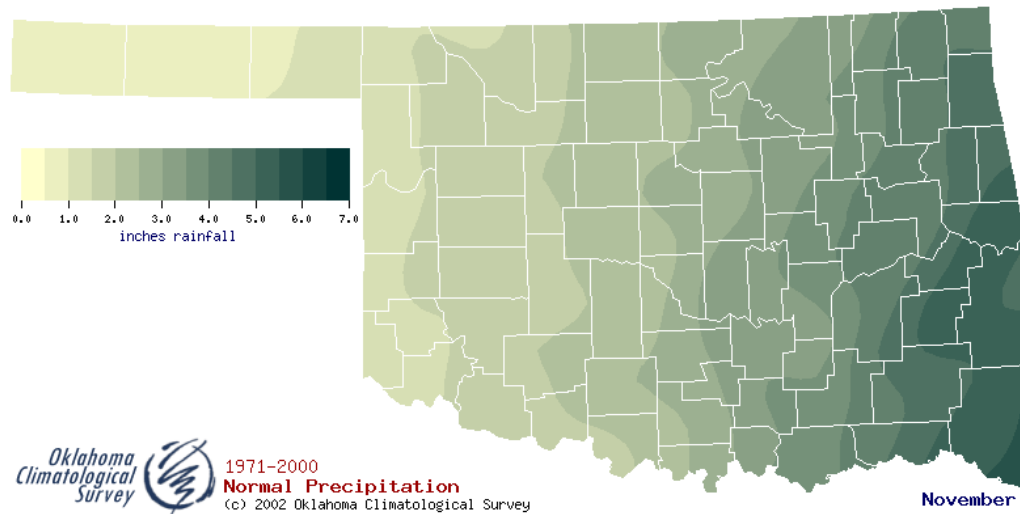
Figure 4.5.3-7. Climatological mean precipitation for November

(Courtesy OCS).
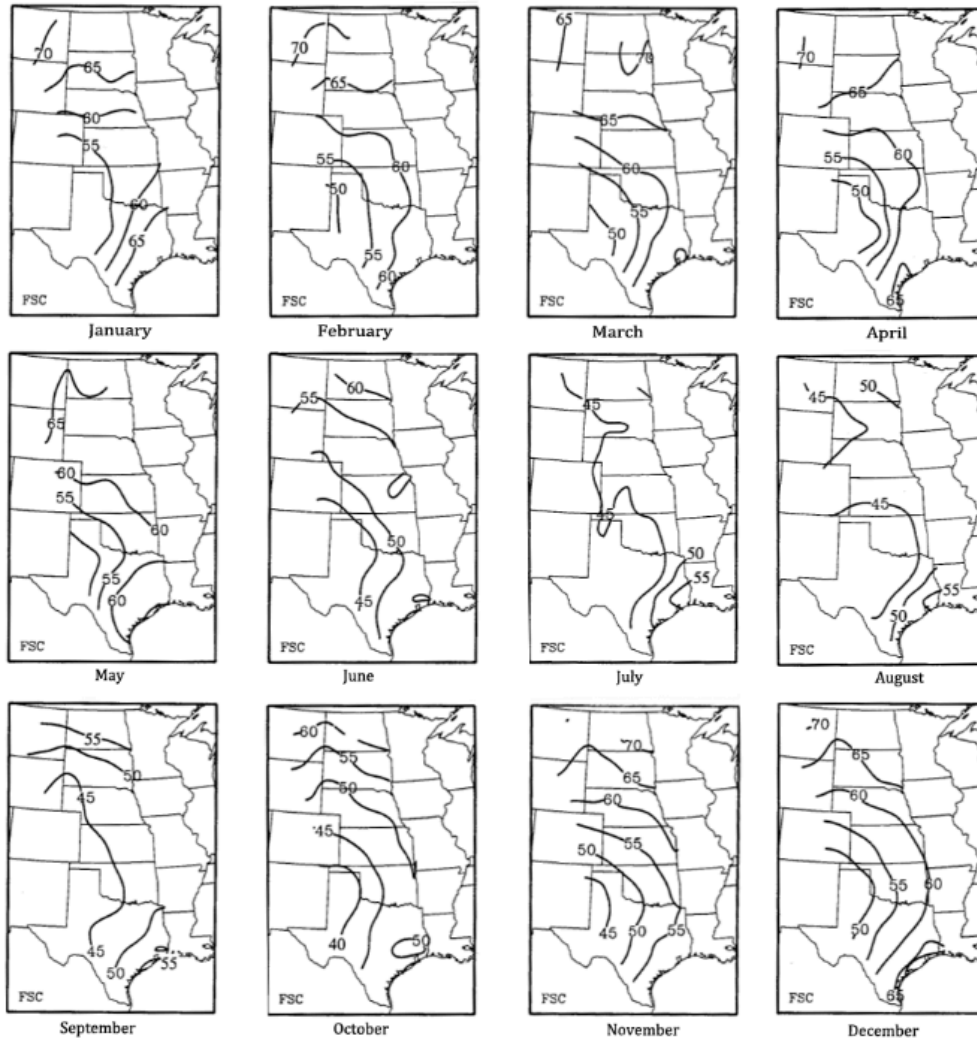
Figure 4.5.4-1. Monthly fractional sky cover (FSC), adapted from figures 3.3a through 3.3l in McMann 1999.

196

APPENDIX C

ACRONYM DEFINITIONS

AC – Alternating Current

AM – Air Mass

ARM – Atmospheric Radiation Measurement Program

BLUE – Best Linear Unbiased Estimator

CC – Cloud Cover

DC – Direct Current

DISC – Direct Insolation Simulation Code

DJF – Period between December 1st and February 28th

DNI – Direct Normal Irradiance

FSC – Fractional Sky Cover

GHI – Global Horizontal Irradiance

HDKR – Hay-Davies-Klucher-Reindl

IEA – International Energy Agency

IPM – Inverter Performance Model

IQR – Interquartile Range

JJA – Period between June 1st and August 31st

KWh – Kilowatt-hours

MAM – Period between March 1st and May 31st

MBE – Mean Bias Error

OASIS - Oklahoma Atmospheric Surface-Layer Instrumentation System

OCS – Oklahoma Climate Survey

OK – Ordinary Kriging

OUN – Norman, Oklahoma Weather Forecast Office

NREL – National Renewable Energy Laboratory

PV - Photovoltaics

PWV – Precipitable Water Vapor

RMSE – Root Mean Square Error

SON – Period between September 1st and November 30th

SPM – Sandia Performance Model

APPENDIX D

PARAMETER AND VARIABLE DEFINITIONS

General

A_i – Anisotropy Index

AM – Air mass value

AM_a – Absolute air mass

C – n x n covariance matrix

D – n x 1 covariance matrix

E_b – Beam radiation incident upon a tilted surface

E_{bh} – Beam radiation, horizontal component

E_d – Diffuse radiation incident upon a tilted surface

E_{d_cir} – Circumsolar component of diffuse radiation on titled surface

E_{d_iso} – Isotropic component of diffuse radiation on titled surface

E_{ext} – Extraterrestrial radiation incident on normal surface

E_{h_ext} - Extraterrestrial radiation, horizontal component

E_g – Global horizontal radiation

E_n – Direct normal radiation

E_{sc} – Radiation solar constant

F – modulating factor (Klucher 1979)

f – modulating factor (Reindl 1990)

I_{mp} - Current at maximum power point

K_d – Clearness condition for diffuse horizontal radiation

K_n – Clearness condition for direct normal irradiance

K_{nc} – Clearness condition for direct normal irradiance under clear skies

K_t – Clearness condition for global horizontal radiation

K_{tc} - Clearness condition for global horizontal radiation under clear skies

ΔK_n – Departure of K_n from clear sky value K_{nc}

ΔK_t - Departure of K_t from clear sky value K_{tc}

m_R – Mean error in ordinary kriging framework

P_{mp} – Maximum power point

R_b – Geometric factor

$\hat{u}$ – prediction locations for ordinary kriging framework

u_i – sample point value in ordinary kriging framework

V_{mp} – Voltage at maximum power point

w – weights of kriging system

α_m – Module tilt angle

δ - Declination angle

ε - Equation of time correction

γ - Solar azimuth angle

γ_m – Module azimuth angle (south = 0°)

$\gamma(h)$ – value of semivariogram at distance h

η - station elevation in meters

λ - Latitude

θ_a – Angle of incidence

θ_z – Solar zenith angle

ψ - local solar noon

σ_R - Error variance in ordinary kriging framework

τ - GMT in decimal form

ω - hour angle

Section 2.5.1

T_c = Cell temperature inside module (°C)

T_o = Reference cell temperature, typically 25°C

E_o = Reference solar irradiance, typically 1000 W/m^2

E_e – Effective Radiation input to SPM

$\delta(T_c)$ = 'Thermal voltage' per cell at temperature T_c

N_s = Number of cells in series in a module's cell-string

$\beta_{Vmp}(E_e) = \beta_{Vmpo} + m_{\beta Vmp} \cdot (1-E_e)$, (V/°C) which is the temperature

coefficient for module maximum- power-voltage as a function of effective

irradiance, E_e.

I_{mpo} = Measured current at maximum power point at standard reporting conditions, T_o, E_o

V_{mpo} = Measured voltage at maximum power point at standard reporting conditions, T_o, E_o

C_0, C_1 = Empirically determined coefficients relating I_{mp} to effective irradiance, E_e. $C_0 + C_1 = 1$, (dimensionless)

C_2, C_3 = Empirically determined coefficients relating V_{mp} to effective irradiance (C_2 is dimensionless, and C_3 has units of 1/V)

Section 2.5.1.2

T_m = Back-surface module temperature, (°C).

T_a = Ambient air temperature, (°C)

E = Solar irradiance incident on module surface, (W/m$_2$)

WS = Wind speed measured at standard 10-m height, (m/s)

Section 2.6.2

P_{ac} = AC-power output from inverter based on input power and voltage, (W)

P_{dc} = DC-power input to inverter (W)

V_d = DC-voltage input (V)

P_{aco} = maximum AC-power rating for inverter at reference condition (W)

P_{dco} = DC-power level where AC-power rating reached at the reference condition, (W)

V_{dco} = DC-voltage level where AC-power rating reached at the reference condition (V)

P_{so} = DC-power required to start inversion process, large influence on inverter efficiency at low power levels, (W)

P_{nt} = AC-power consumed by inverter at night, must power required circuitry to sense PV array voltage, (W)

C_o = definines the curvature of AC-DC-power relationship at the reference conditions, the default value of zero gives a linear relationship, (1/W)

C_1 = empirical coefficient that allows P_{dco} to vary linearly with DC-voltage input, defaults to zero, (1/V)

C_2 = empirical coefficient allowing P_{so} to vary linearly with DC-voltage input, defaults to zero, (1/V)

C_3 = empirical coefficient allowing C_o to vary linearly with DC-voltage input, defaults to zero, (1/V)

a = Empirically-determined coefficient establishing the upper limit for module temperature at low wind speeds and high solar irradiance

b = Empirically-determined coefficient establishing the rate at which

module temperature drops as wind speed increases